Deliverable 4.4: Report describing the benchmarks to be carried out during the WP DONUT

Work Package DONUT

The project leading to this application has received funding from the European Union's Horizon 2020 research and innovation programme under grant agreement No 847593.

Document information

Project Acronym	**EURAD**
Project Title	**European Joint Programme on Radioactive Waste Management**
Project Type	**European Joint Programme (EJP)**
EC grant agreement No.	**847593**
Project starting / end date	**1st June 2019 – 30 May 2024**
Work Package No.	**4**
Work Package Title	**D**evelopment and Improvement **O**f **NU**merical methods and **T**ools for modelling coupled processes
Work Package Acronym	**DONUT**
Deliverable No.	**4.4**
Deliverable Title	**Report describing the benchmarks to be carried out during the WP DONUT**
Lead Beneficiary	**ANDRA**
Contractual Delivery Date	
Actual Delivery Date	**12 06 2023**
Type	
Dissemination level	
Authors	**Nikolaos Prasianakis (PSI), David Mašín (CU), Javier Samper (UDC), Kateřina Černochová (CTU) Antonio Gens (UPC), Diederick Jacques (SCK-CEN), Dimitri Kulik (PSI), Alba Mon (UDC), Luis Montenegro (UDC), Jiří Svoboda (CTU) Christophe Tournassat (ISTO, Université d'Orléans), Maria Victoria Villar (CIEMAT), Francis Claret (BRGM)**

To be cited as:

Prasianakis, N., Mašín D., Samper J., Černochová K., Gens A., Jacques D., Kulik D., Mon A., Montenegro L., Svoboda J., Tournassat C., Villar M.V., Claret F. (2023). Report describing the benchmarks to be carried out during the WP DONUT. Final version as of 12.06.2023 of deliverable D4.4 of the HORIZON 2020 project EURAD. EC Grant agreement no: 847593.

Disclaimer

Acknowledgement

This document is a deliverable of the European Joint Programme on Radioactive Waste Management (EURAD). EURAD has received funding from the European Union's Horizon 2020 research and innovation programme under grant agreement No 847593.

Status of deliverable		
	By	Date
Delivered (Lead Beneficiary)	Andra[BRGM]	12/06/2023
Verified (WP Leader)	Francis CLARET	10/05/2023
Reviewed (Reviewers)	Bernd Grambow	15/05/2023
Approved (PMO)	Bernd Grambow	12/06/2023
Submitted to EC (Coordinator)	Andra	13/06/2023

Executive Summary

A specific outcome of DONUT work package is the definition of benchmarks that will be use both inside DONUT and outside to foster interactions. While international benchmarks initiative are existing (Bildstein et al., 2021; Birkholzer et al., 2019; Steefel et al., 2015), the goal here is to define benchmarks of methods and tools to quantify efficiency and added-value in terms of :

- increase of knowledge (e.g. better physical representation, integration of couple processes, exchange between viewpoints of different disciplines)
- accuracy, robustness, computational cost,
- robustness of scale-transition approaches
- ability to manage uncertainty and sensitivity analyses

To tackled this issue, three benchmark exercise are running within DONUT. The first one is relevant to machine learning and geochemistry, the second one aims at modelling the Thermo Hydro Mechanical behaviour of bentonite and the third one deals the reactive transport modelling of two-phase flow coupled Thermo Hydro Chemical processes. Last but not least the first one provides a clear link with the EURAD WP ACED and FUTURE, the second one with HITEC while the last one is linked to ACED and GAS.

Table of content

List of figures

List of Tables

1. INTRODUCTION

In addition to the specific work that will be conducted by each partner, a specific outcome of DONUT is the definition of benchmarks that will be use both inside DONUT and outside to foster interactions. While international benchmarks initiative are existing (Bildstein et al., 2021; Birkholzer et al., 2019; Steefel et al., 2015), the goal here is to define benchmarks of methods and tools to quantify efficiency and added-value in terms of :

- increase of knowledge (e.g. better physical representation, integration of couple processes, exchange between viewpoints of different disciplines))
- accuracy, robustness, computational cost,
- robustness of scale-transition approaches
- ability to manage uncertainty and sensitivity analyses

Recently, Bildstein et al. (2021) in a guest editorial to the subsurface environmental simulation benchmarks special issue mentioned emerging benchmarking opportunities. Amongst others, machine learning was identified. Indeed it is considered as a recent disruptive technology in the field of reactive transport and will possibly unlock the next generation of simulation that require high demanding CPU time (Leal et al., 2017). The high computing cost associated with chemical equilibrium calculations is considering as the most demanding one in comparison to fluid flow or heat transfer. To circumvent this issue the use of surrogate model provides promising perspectives (Laloy and Jacques, 2019; Prasianakis et al., 2020). Therefore, having a benchmark that tackle this issue will be very useful. In that context DONUT is defining one benchmark relating to ***machine learning and geochemistry***. This latter aims at providing a point of reference for testing and addressing the challenges relevant to: (i) producing high quality training datasets, which can be used by all available ML techniques, (ii) using Deep neural network learning, Polynomial Chaos Expansion and Gaussian processes to learn from the generated data, (iii) testing the accuracy of predictions for geochemical calculations, reactive transport and uncertainty analysis. The philosophy of the benchmark is described in the paragraph 2. It is worth noticing that two geochemical system will be investigated: one related to cement based material degradation and one related to uranium sorption on clay materials. **It therefore provides a clear link to the ACED and FUTURE WPs.** In addition, within the WP **HITEC** two experiments have been selected as benchmarks for validation of constitutive and numerical models. These experiments represent a column section of barrier system, heated at one-end to mimick canister heat, with water supply at the other end to mimick natural water supply. One test (CIEMAT/UPC) adopts MX-80 bentonite in pellet state heated up to 140°C. The other test (SURAO/CTU) adopts BCV bentonite in a powder state heated up to 150°C. The tests, being performed in the laboratory at a smaller scale allow for more detailed control of boundary and initial conditions than full-scale or in-situ Mock-Up tests, **thus providing valuable data for THM model evaluation.**

At last but not least Bildstein et al. (2021) stress the need for benchmarking in the context of multiphase multicomponent reactive transport. Outside EURAD a benchmark entitled “Reactive Multiphase Flow in Porous Media at the Darcy Scale” has been initiated and recently discussed at the conference on Mathematical & Computational Issues in the Geosciences https://meetings.siam.org/sess/dsp_talk.cfm?p=111450. The extension of this benchmark to the radwaste context has been discussed. A preliminary draft presentation of the benchmark and its philosophy is given in paragraphs 4,5 and 6, providing . **a clear link to the WP GAS and ACED**

2. BENCHMARK RELEVANT TO MACHINE LEARNING AND GEOCHEMISTRY

2.1 Executive summary

Due to recent technological developments, the fields of artificial intelligence and machine learning methods (ML) are growing at a very fast pace. The DONUT scientific community has recently started using ML for a) accelerating numerical simulations, b) multiscale and multiphysics couplings, c) uncertainty quantification and sensitivity analysis. There are first evidences, which suggest an overall acceleration of calculations between one to four orders of magnitude (Laloy and Jacques, 2019; Prasianakis et al., 2020). Within DONUT a benchmark is designed to coordinate activities and test a variety of ML techniques relevant to geochemistry and reactive transport. It aims at benchmarking the major geochemical codes, at generating high quality data for training/validation of existing/new methodologies and at providing basic guidelines about the benefits and drawbacks of using ML techniques.

2.2 Benchmark philosophy

Machine learning (ML) is a subset of artificial intelligence with special focus on learning from experimental/numerical data and subsequently representing the correlations of the data in multidimensional variable spaces. This is achieved by using a variety of mathematical models, which result in methodologies like deep neural network learning, polynomial chaos expansion and Gaussian processes. In the context of radioactive waste management, ML may be used to create surrogate models, which are computationally more efficient than the full physical models. For example, it can be used to accelerate the geochemical calculations used in reactive transport calculation(Laloy and Jacques, 2019; Prasianakis et al., 2020). An illustrative example is shown in figure 1. Typically in reactive transport simulations the transport solver is much faster to compute compared to the thermodynamic and chemistry solver, with the latter being responsible for 90-99% of the overall computational time. The reason for that is that the thermodynamic solver typically involves the iterative solution of several equations until convergence for a single computational grid point, while transport equations are less demanding. With chemistry being the bottleneck, effort has to be spent to accelerate that part of the code. Using machine learning a surrogate model for the chemistry may be created. Once trained and coupled with the transport solver, significant speed-ups are obtained. These models require a training dataset, which is always produced by the full physical-chemical numerical code. The number of training points depends on the number of variables, which defines the input multidimensional space. Once the training dataset is available, the training phase takes place where the ML algorithm learns from the data and is able to represent complex data correlations. After the training is finished, the ML algorithm is ready to be used for predictions for a combination of parameters, which does not belong to the training dataset, which however lies within the range set from the minimum and maximum values of the input parameters existing in the training dataset. The accuracy of the predictions highly depends a) on the size and quality of the training dataset (typically the larger the better), b) on the ML algorithm that was used, and c) on the tuning of the hyper-parameters of the each ML algorithm. Hyper parameter is a parameter whose value is used to control the learning process.

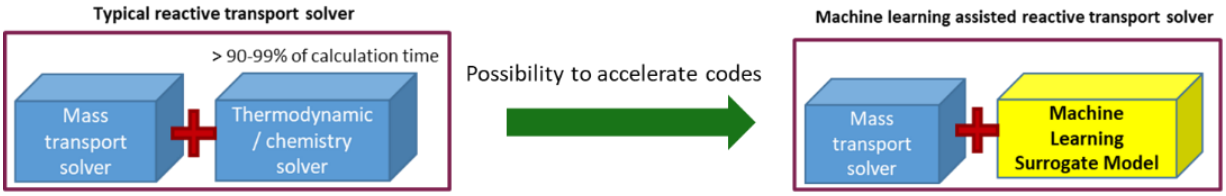

Figure 1*: In typical reactive transport simulations, thermodynamics and chemistry consume most of the computational time. Coupling of carefully trained surrogate models provides an overall acceleration of*

the simulation between one to four orders of magnitude (Laloy and Jacques, 2019; Prasianakis et al., 2020)

This benchmark aims in providing a point of reference for testing and addressing the challenges relevant to:

- Streamline the production of high quality consistent training datasets, using the major geochemical solvers. Setting the specifications such that the datasets may directly use all available and future ML techniques.
- Using Deep neural network learning, Polynomial Chaos Expansion and Gaussian processes and other techniques to learn from the generated data
- Testing the accuracy of predictions for geochemical calculations, reactive transport and uncertainty analysis.

2.3 Benchmark Roadmap and main milestones

This benchmark exercise is already at an advanced stage in terms of setting the problem as well as relevant to the obtained results. The history and future timeline of the benchmark is described below and illustrated in figure 2:

- **June to December 2021**: System of interest specification and definition of the different benchmark levels of complexity. This action is done.
- **January 2022 to December 2022**: Production of the training sets. This action is done
- **May 2022 to June 2023**: Resolution of the benchmarks by the different teams
- **November 2022**: 1st Workshop to discuss geochemical systems and preliminary ML results (took place 29.11.2022)
- **November 2022 to May 2023**: Base on the November workshop some ew calculations have been performed to enriche the training set. Accuracy metrics were defined to compare the results.
- **April 2023**: 2nd Workshop to exchange information and compare ML results for different levels of complexity. Following the workshop the teams started working in improving the accuracy of their methodologies
- **March 2023 to August 2023**: Wrap up of common publications

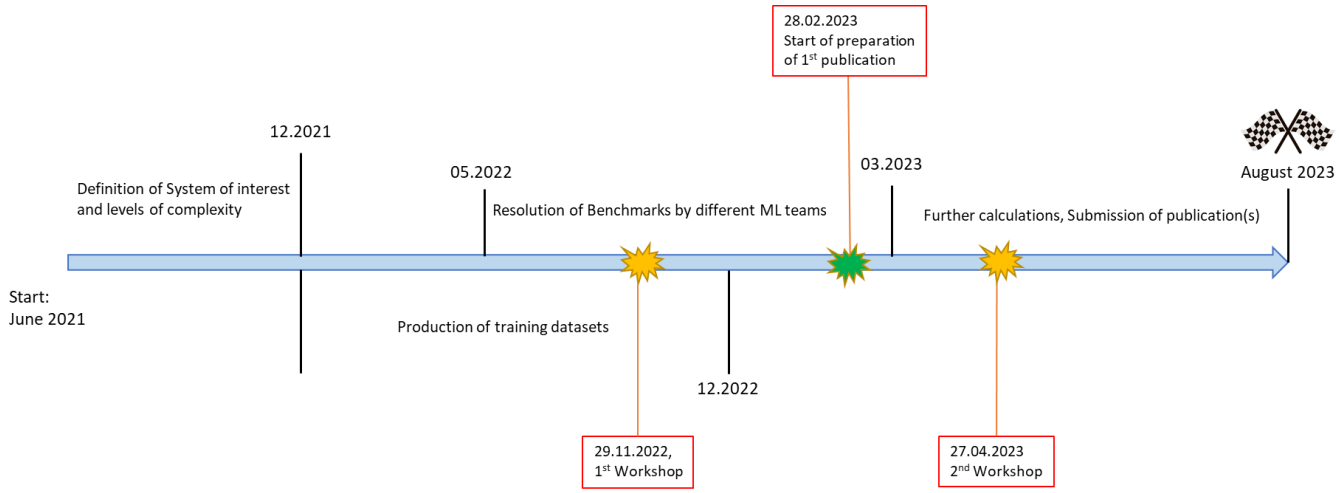

Figure 2*: Benchmark timeline*

2.4 Involved teams

At the moment more than 10 research teams across Europe (within and outside EURAD) have joined this benchmark, both at the level of chemical system definition and production of training data, and for the part relevant to machine learning techniques. The main participating teams and contact persons are listed below in FIGURE 3:

Geochemical Systems / training datasets: **SCK-CEN**	D. Jacques	(*PHREEQC*)
Geochemical Systems/ training datasets: **NRG**	H. Meeussen	(*ORCHESTRA*)
Geochemical Systems/ training datasets: **PSI**	D. Kulik	(*GEMS*)
ML: **SCK-CEN** (Neural Networks)	E. Laloy / D. Jacques	
ML: **Amphos21** (Neural Networks)	A. Idiart et al.	
ML: **PSI** (Neural Networks)	N. Prasianakis	
ML: **ANDRA/ Uni Paris Saclay** (Polynomial Chaos PCE)	M. Savino, M. Leconte, B. Cochepin	
ML: **UDC/ Env. Data Tech Inc.** (Gaussian Processes and Random forests)	J. Samper, J. Samper (Jr.), C. Yang	
ML: **GFZ-Potsdam** (Geometric Method and Trees)	M. De Lucia	
ML: **BRGM/Uni Orleans/CEA**	F. Claret et al	

Figure 3: *Research teams and contact persons involved in the geochemistry and machine learning benchmark*

2.5 High quality training datasets and problem set

Two systems of interest have been identified. The first system is relevant to cement dissolution/precipitation. The chemical system includes Ca-Si and simple C-S-H models and the CEMDATA-18 thermodynamic database is used (Lothenbach et al., 2019). The used approach is based on C-S-H solid solution thermodynamic models developed by Kulik et al. With increasing complexity, a more complete system is addressed, including Al-Mg-S-C-(Na-K) using a structurally-consistent CASH+ sublattice solid solution model for fully hydrated C-S-H phases (Kulik et al., 2022) and its extension for the uptake of alkali metals and alkaline earth metals in C-S-H (Miron et al., 2022).

The second system is relevant to the sorption of U on claystone formation (e.g. Callovo-Oxfordian), Opalinus or BOOM clay). Some preliminary work on the used of surrogate model to decipher Cs sorption uncertainty on Callovo-Oxfordian formation has been made and has been used as starting point to define the benchmark storyboard. Uranium is a more complex system because of its complex speciation and requires to build a benchmark with an increasing complexity. The model used for U(VI) sorption on montmorillonite in the absence and presence of carbonate is described in Marques et al. (2012) For the two systems of interest the major geochemical solvers PHREEQC, ORCHESTRA, GEMS (Figure 4) have been used by experts to produce data relevant to the geochemical systems of interest. The results already show extremely consistent results between the geochemical solvers. The systems of interest, the thermodynamic databases and the exact models have been already defined.

Figure 4: *The major geochemical solvers are operated by experts in the field, benchmarked and used to produce consistent training datasets for the machine learning techniques.*

2.1 Data Management and open research

Throughout the benchmark, all relevant input files, models and results are stored in an online secure cloud service (SWITCH), offered by PSI and Swiss Universities. The status and progress may be followed online at any time at the following link: https://drive.switch.ch/index.php/s/PcxgaiYIRVS2k52 (the folder is password protected; credentials may be provided at any time to interested parties and EURAD participants). It is intended that after the end of the benchmark all files will be accessible online as well as supplemental material to the journal publications. Snapshot of the folder structure may be seen in Figure 5

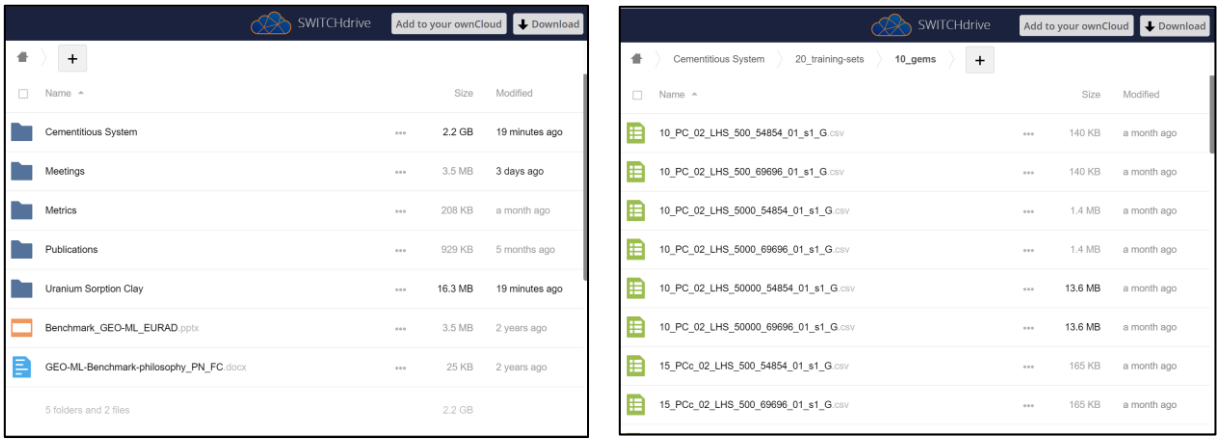

Figure 5: *Online Benchmark Data management and SWITCH drive. The benchmark workflows, documentation, models, input files, output files and results are accessible in well structured folder system.*

The benchmark team has defined a specific workflow in order to standardize the process from system definition to machine learning output. In figure 6, the workflow from system definition to creation of training files is illustrated.

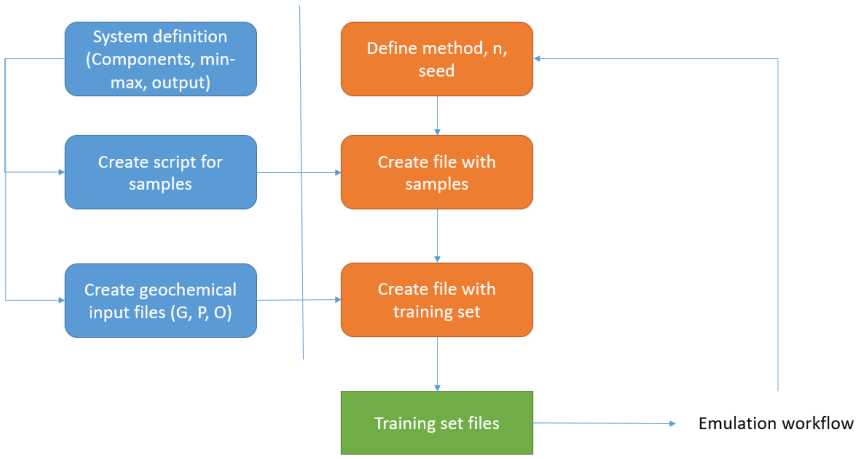

Figure 6: *The workflow from system definition to creation of training files is illustrated.*

2.2 Application and accuracy of predictions of ML algorithms

Several ML methods (e.g. deep neural networks technique, polynomial chaos expansion, Gaussian processes) are used to create the surrogate models. The trained surrogate models are then used in a series of problems to evaluate their accuracy. At the first stage, the ML models are used to make pure geochemical calculations and well defined accuracy thresholds are provided. Several teams as shown in figure 3 have already trained their algorithms and produced the first results. For the low complexity cementitious system, very good agreement in terms of accuracy can already be demonstrated. The accuracy of the surrogate models i can be measured by using an independent set of input samples and testing against the ground truth (result of geochemical solver). The metrics of accuracy which are used at the moment are shown in figure 7. Several measures of accuracy are used to scrutinize the efficiency of the produced surrogate models. When a model passes all criteria e.g. mean square error (MSE), mean average error (MAE), root mean square error (RMSE) being lower than specific desired accuracy values, then it can be considered suitable for use in reactive transport simulations in the range of input data and the according learning set. The level of accuracy can be set depending on the scope of the respective application.

$$MAE = \frac{1}{N}\sum_{i=1}^{N}|y_i - \hat{y}|$$

$$MSE = \frac{1}{N}\sum_{i=1}^{N}(y_i - \hat{y})^2$$

$$RMSE = \sqrt{MSE} = \sqrt{\frac{1}{N}\sum_{i=1}^{N}(y_i - \hat{y})^2}$$

$$R^2 = 1 - \frac{\sum(y_i - \hat{y})^2}{\sum(y_i - \bar{y})^2}$$

Where,

$\hat{y}$ – *predicted value of y*

$\bar{y}$ – *mean value of y*

$$\mathrm{MAE}_{log} = \frac{1}{N}\sum|\log y_i - \log \hat{y}_i| = \frac{1}{N}\sum\left|\log \frac{y_i}{\hat{y}_i}\right|$$

$$\mathrm{RMSE}_{log} = \sqrt{\frac{1}{N}\sum(\log y_i - \log \hat{y}_i)^2} = \sqrt{\frac{1}{N}\sum\left(\log \frac{y_i}{\hat{y}_i}\right)^2}$$

$$\mathrm{RMSLE} = \sqrt{\frac{1}{N}\sum[\log(y_i + 1) - \log(\hat{y}_i + 1)]^2} = \sqrt{\frac{1}{N}\sum\left(\log \frac{y_i + 1}{\hat{y}_i + 1}\right)^2}$$

$$\mathrm{MAPE} = \frac{100\%}{N}\sum|\alpha_i|$$

$$\mathrm{RRMSE} = \sqrt{\frac{1}{N}\sum(\alpha_i)^2}$$

Figure 7*: Surrogate models created by machine learning are tested against independent samples with the metrics of accuracy as shown in this figure.*

While the robustness of the results and associated workflow have still to be consolidated , preliminary results on the simplest cases indicate that all teams can achieve very high accuracy with their modelling techniques.. Moreover, a significant speedup of the order of two to four orders of magnitude is already demonstrated depending on the complexity of the system. Some indicative results are presented below in figure 8. These are results from the PSI team. Similar results from all teams are deposited online in the Benchmark cloud directory. In figure 8, (left) a cementitious system with its input parameters and operational range is illustrated. The machine learning model, in this case neural networks, accepts as input three variables which define the composition of the system. The output are the 17 variables as mentioned on the table. For a specific output dimension, namely the amount of Ca in the solid phase after equilibration, the model predictions (red boxes) is tested against the ground truth, which in this case is the geochemical solver GEMS (blue crosses). Both the visual interpretation and the aforementioned metrics (for all output parameters) indicate close agreement between the ML-model and the geochemical solver.

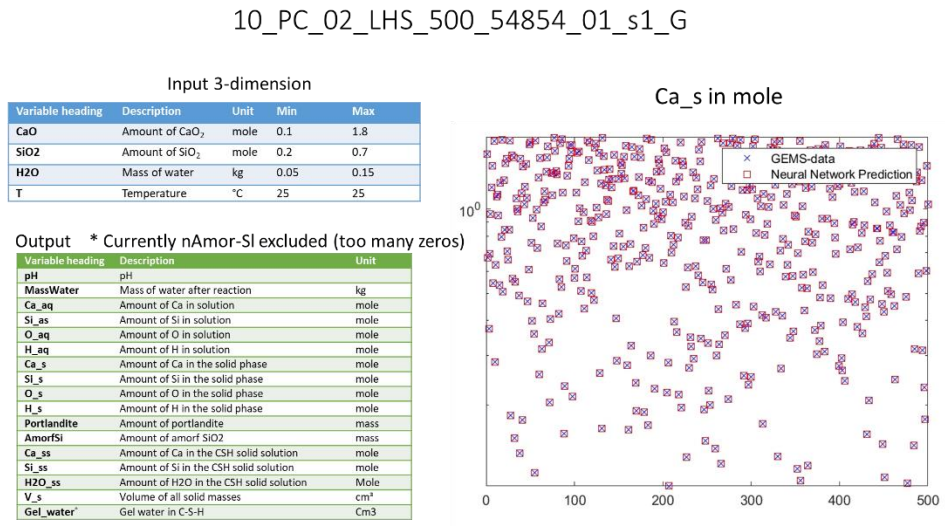

Figure 8: *Example of a cementitious system with input and output parameters (left). Surrogate model prediction (example of PSI-team using neural networks) for the amount of Ca in the solid phase after equilibration, and visual comparison with the geochemical solver GEMS output is shown; The y-axis is the molar concentration of Ca in the solid phase, while the x-axis signifies the test case under consideration. A total of 500 random 3-dimensional input test is shown. In this graph 500 random samples are compared (right)*. Accuracy and speed up of calculations is maintained at very high levels.

3. BENCHMARK CASES FOR BENTONITE THM ANALYSIS

These modelling benchmarks have been defined in Milestone MS130: HITEC Task 3.3 - Modelling benchmarks – description (Description of calibration case, verification cases and benchmarks selected for T3.3 in cooperation with DONUT).

3.1 Bentonite modelling benchmark of CIEMAT/UPC

3.1.1 Introduction

This section contains the description of a modelling benchmark involving bentonite material corresponding to the planned activities of Subtask 3.3: “Small scale experiments, model development and verification”.

The benchmark is based on a laboratory experiment being performed by CIEMAT in which a column of MX-80 bentonite pellets is subjected to high temperature (140ºC) and hydration. The benchmarks therefore is well placed to check model performance in the simulation of THM phenomena at elevated temperatures. The test has been running for over 9 years and it will be finished and dismantled during 2021.

The experimental set-up, the instrumentation, the testing protocol, the main characteristics of the material employed and some results are presented in the following sections. The final section indicates the results that are expected in this benchmark. Additional information on the test is provided in Villar et al. (2012) and Iglesias et al. (2019).

3.1.2 Experimental layout and instrumentation

The test is performed on a 50 cm long column of bentonite pellets that is hydrated through the top surface whereas heat is applied to the bottom surface, at constant temperature. The body of the cell consists of four cylindrical elements made out of Teflon PTFE (thermal conductivity 0.25 W/m·K) to prevent as much as possible lateral heat loss. In order to reinforce mechanically the wall of the cell, that has to support the swelling pressure of the clay, it was externally surrounded by half-cylindrical pairs of stainless steel shells, joined by steel braces. The cell was wrapped with a 5-mm thick dense foam insulation to reduce heat loss (thermal conductivity 0.04 W/m·K). The insulation of the bottom 5 cm of the column was enhanced after 1518 hours of heating by the addition of a 30-mm thick insulation wool (Superwool 607 HT) blanket (thermal conductivity 0.04 W/m·K) and a 25-mm thick ISOVER BT-LV blanket (thermal conductivity 0.034 W/m·K). The nominal internal diameter of the cell is 7 cm and the inner length 50 cm. Those are, therefore, the dimensions of the specimen column.

The bottom part of the cell has a plane stainless steel heater and the power is supplied by an electric resistance. The power supplied is measured during the test. Inside the top steel plug of the cell, there is a reservoir where water circulates at room temperature. In this way, a constant temperature gradient between top and bottom of the sample is applied. Hydration takes place through the perforated top lid of the cell. Pearson water (Pearson et al., 2011)that mimic the pore water of the Mont Terri Underground Research Laboratory (Na 7.1, K 0.11, Ca 0.11, Mg 0.03, Cl 0.56, S (6) C 5.79 mmol/l, pH 8.4) is supplied from a tank hanging from an electronic load cell, and the water intake is measured by changes in the weight of the tank. A load cell was located at the top of the cell with the aim of measuring the axial pressure developed by the clay. The layout of the experiment is shown in figure 9.

After the cell was filled with the bentonite sealing material, its walls were perforated for the installation of capacitive-type sensors placed in the axis of the column at three different vertical levels (10, 22 and 40 cm from the heater) to measure relative humidity (RH) and temperature (*T*) inside the bentonite. The transducers used were VAISALA HMT334 protected by cylindrical stainless steel filters. The accuracy of the humidity sensor was ±1% in the 0-90 percent RH range and ±2% in the 90-100 percent RH range. The holes in the cell walls were sealed by plugs with O-rings placed in contact with the sensors.

The water intake (in weight), the heater power, the axial pressure and the relative humidity (RH) and temperature (*T*) at three different levels inside the bentonite are continuously being measured during the test. A schematic diagram of the whole setup is shown in figure 10

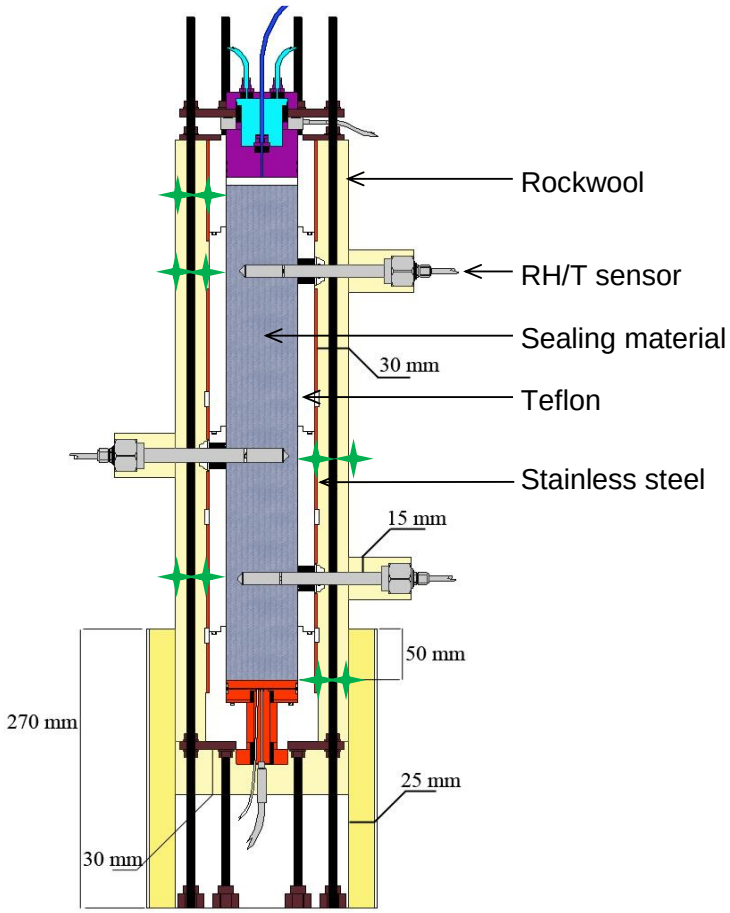

Figure 9. *Layout of the column experiment*

Temperatures on the external surface of the cell have been measured periodically with thermocouples placed on the surface of the cell, i.e. on the steel reinforcement, at the same levels as the sensors inserted in the column. The temperatures at the same level on the surface of the insulating rockwool material are also being measured. From September 2015 the external temperatures are also measured at the heater level and at 1 cm below the hydration surface. These measuring points are indicated by green crosses in figure 9.

3.1.3 Material tested

The material used in the experiment is made up of MX-80 bentonite pellets (Figure 11). It is the same material used in a section of the HE-E experiment carried out in the Mont Terri laboratory. The as-received water content of the material was 6.4%. The grading curve obtained by dry sieving in the CIEMAT laboratory is shown in figure 12.

The dry density of the solid grains determined with pycnometers using water as dispersing agent was 2.75 g/cm^3; the external specific surface area determined by the 9-point BET method was 33 m^2/g; and the superficial thermal conductivity in the as-received state (which probably corresponds to a dry density of around 1.1 g/cm^3) determined at room temperature using the transient hot wire method (KEMTHERM QTM-D3) was 0.12 W/m·K. The specific heat capacity of the material ground and dried at 110°C was determined in a TG-DSC Setsys Evolution 16 equipment. The determination was performed in the range of temperatures from 22 to 298°C. The values obtained ranged between 0.64 J/g·K (at 22°C) and 0.97 J/g·K (at 115°C) (Fernández, 2011). The pore size distribution of the uncompacted material was

obtained by mercury intrusion porosimetry. The bentonite granulate has predominantly mesopores with a size mode of about 0.014 µm (Villar, 2013).

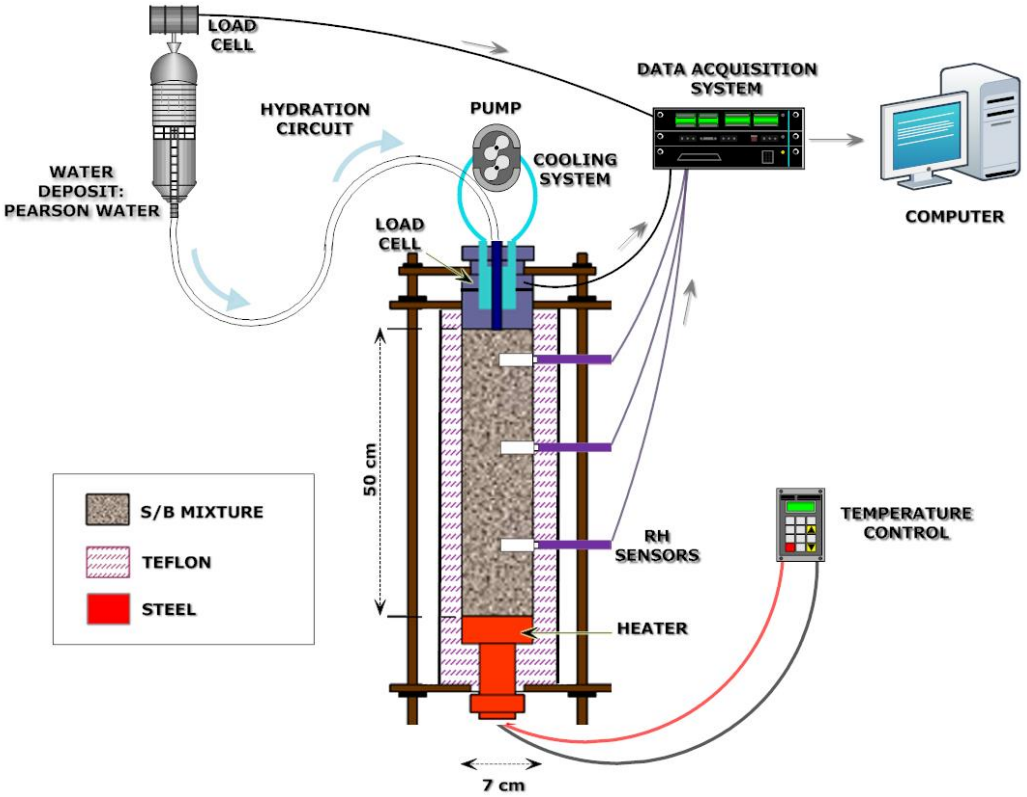

Figure 10. *Experimental setup. S/B indicate sand bentonite mixture. It is generic on the illustration here MX80 pellets have been used.*

Figure 11: *MX-80 bentonite pellets used in the experiment*

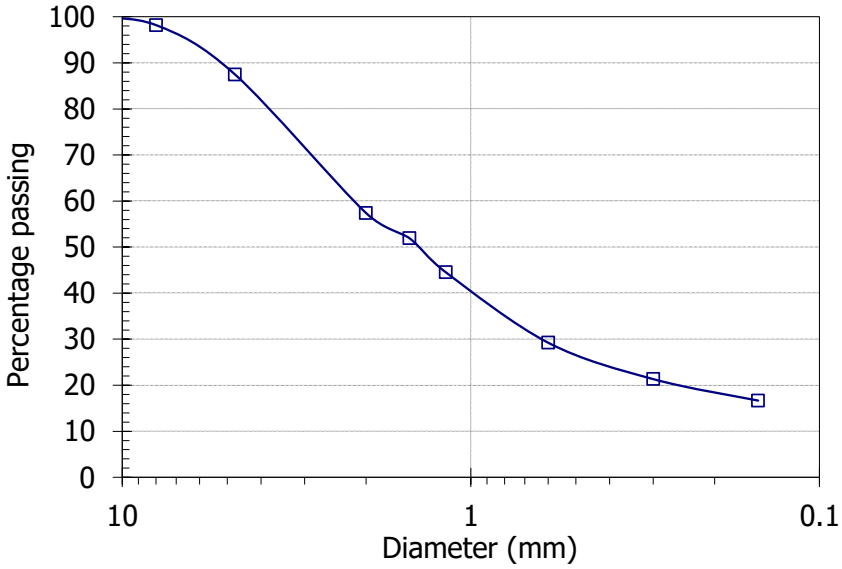

Figure 12: *Grading curve of the MX-80 pellets obtained by dry sieving*

The swelling pressure of small samples (3.8 or 5.0 cm in diameter, 1.2 cm in height) of MX-80 bentonite powder compacted at its hygroscopic water content was determined at CIEMAT at room temperature using deionised water as saturation fluid. The swelling pressure (P_s, MPa) can be related to final dry density (ρ_d, g/cm^3) through the following equation:

$$\ln P_s = 5.44\ \rho_d - 6.94 \quad (1)$$

The hydraulic conductivity (k_w, m/s) of samples of powdered MX-80 bentonite (grain size <1 mm), compacted at different dry densities (ρ_d, g/cm^3) and kept in stainless steel cells at constant volume was measured under saturated conditions in a constant head permeameter (Villar, 2020). Deionised water and water of 0.5% salinity were used as permeants. Exponential relations between dry density (ρ_d, g/cm^3) and hydraulic conductivity (k, m/s) were found:

For deionised water: $$\log k_w = -2.94\ \rho_d - 8.17 \quad (2)$$

For saline water: $$\log k_w = -2.39\ \rho_d - 8.78 \quad (3)$$

Although these tests were performed using powder material with a grain size <1 mm (from batches different from those used to manufacture the pellets), it has been proved that the saturated hydro-mechanical properties of pellets mixtures are similar to those of fine granulates (Imbert and Villar, 2006). However, it is known that the salinity of the pore water reduces the swelling capacity of clays while it increases the hydraulic conductivity. Therefore, the swelling pressure and the hydraulic conductivity in the test may differ from the values derived from equations (1) to (3).

3.1.4 Preparation of the specimen and test protocol

The column was manufactured by filling the cell in seven equal layers. The pre-determined amount of the material was poured inside the cell. The quantity of material was computed taking into account the initial water content, the inner volume of the cell and the target dry density, which was 1.47 g/cm^3. To fill the cell, a funnel was used to avoid the loss of the finer particles (Figure 13) and no compaction was applied.

Between the bentonite and the upper lid, a 70-mm diameter and 8-mm high porous stone was placed. The top plug with the O-rings was then pushed to its location and tightened. This assembly was weighed and afterwards the holes for the insertion of the sensors were drilled into the granulate material through the Teflon walls. The assembly was weighed again in order to record how much material had been lost

as a consequence of drilling. In this way, the initial characteristics of the column could be obtained (Table 1). The difference with respect to the target density was due to the compression of the column caused by the tightening of the upper plug. Figure 13 shows a view of the cell in its final configuration before and after being wrapped with the insulating material.

a) b) c)

Figure 13: *a) Pouring the pellets inside the cell, b) View of the assembled column, c) View of the column after installing the thermal insulation*

Table 1 *Main features of the specimen after installation*

Initial water content (%)	6.4	Height (mm)	483.9
Sample mass (g)	3094	Dry density (g/cm^3)	1.53
Sample mass after drilling (g)	3076	Porosity	0.444
Volume of sensors (cm^3)	20	Void ratio	0.797
Theoretical dry mass (g)	2891	Degree of saturation (%)	22
Diameter (mm)	70.0		

The first stage of the test involved heating but no hydration. The heating started on 22/11/2011, a date that is considered time *t=0* of the experiment. After 33 minutes the first target temperature of 100ºC was reached. On 17/4/2012, after the observations of relative humidity throughout the column had stabilised, the temperature was increased in 17 minutes to 140ºC.

Heater power was measured from *t*=1250 h. The improvement of the insulation during the heating phase induced a reduction of the average heater power from 12 to 8 W to keep the target temperature of 100°C at the heater surface. When the heater temperature increased to 140°C, the average heater power increased to about 12 W.

On 18/6/2012 hydration started while maintaining the heater temperature to 140°C. Hydration was performed by applying a constant water height of 60 cm on the top surface of the specimen. The thermal and hydraulic conditions have been kept constant since. At the end of the experiment, the test will be dismantled and the distributions of dry density and water content along the column determined.

Figure 14 shows the laboratory temperature, heater power and temperature at 10 cm from the heater during the hydration stage of the test. It can be observed that there are fluctuations (mainly seasonal) in the laboratory temperature that affect somewhat the temperatures in the column. The power required to maintain a constant temperature in the heater is affected as well.

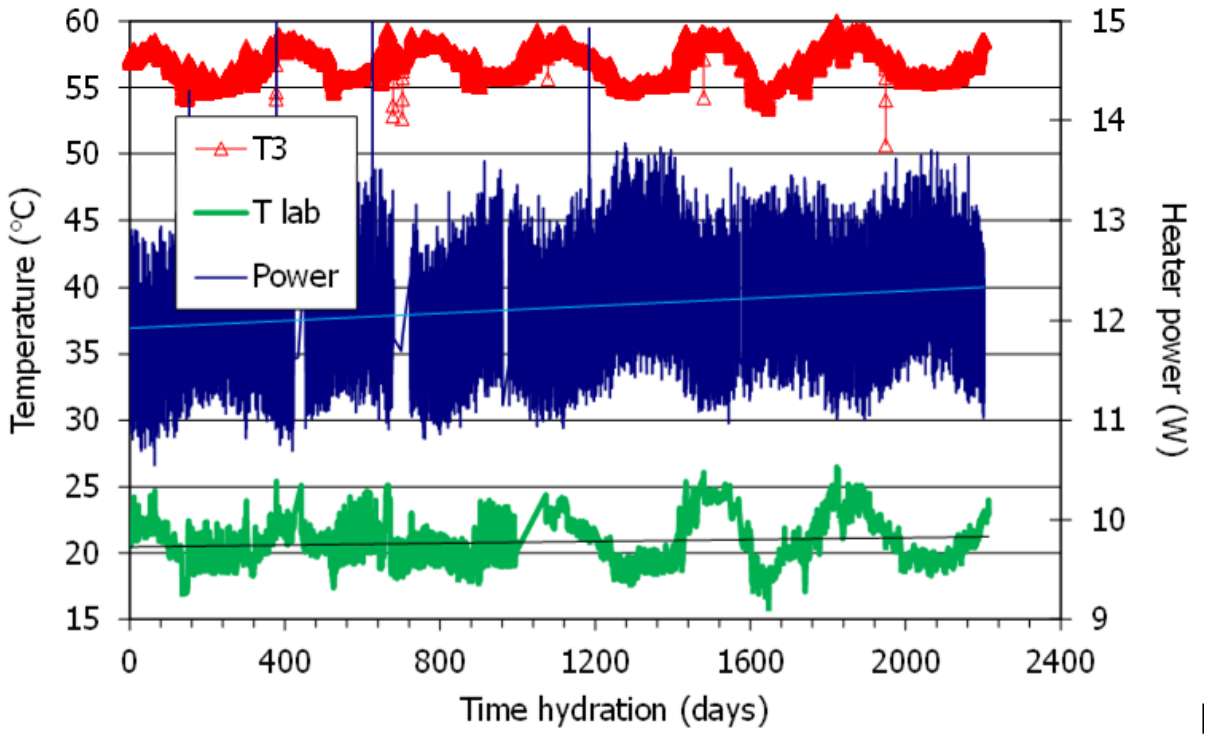

Figure 14: *Laboratory temperature, heater power and temperature at 10 cm from the heater (T3) during the hydration stage of the test*

3.1.5 Observations

A sample of the observations made during the test is presented in this section. Figure 15 shows the evolution of the temperatures at the three distances from the heater where the sensors are located (T1 at 40 cm, T2 at 22 cm and T3 at 10 cm from the heater). It can be observed that, apart from the ambient fluctuations, temperatures are largely constant during the test. Figure 16*a* shows the evolution of water intake and relative humidity. All the sensors record a progressive hydration but the evolution is much affected by temperature. Figure 16*b* shows the variation of axial pressure, measured at the top of the column, with time. It can be noted that much of the pressure increase occurs during the early hydration times.

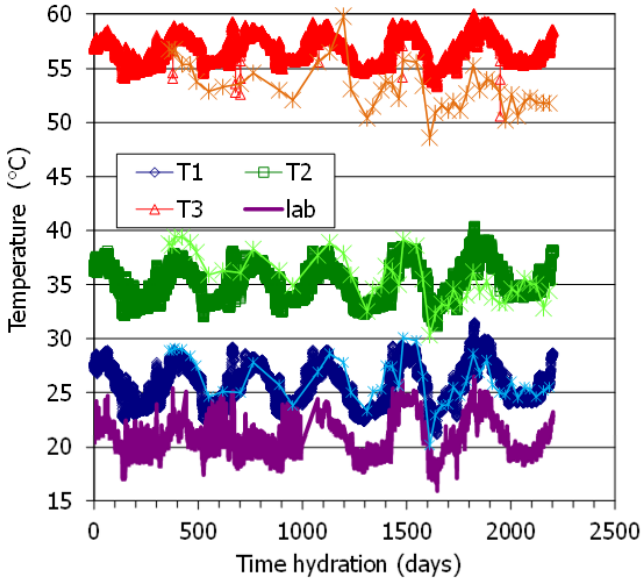

Figure 15: *Evolution of temperature after the start of hydration in the bentonite and on the steel surface (denoted by crosses) (T1 at 40 cm, T2 at 22 cm and T3 at 10 cm from the heater). The laboratory temperature is also shown.*

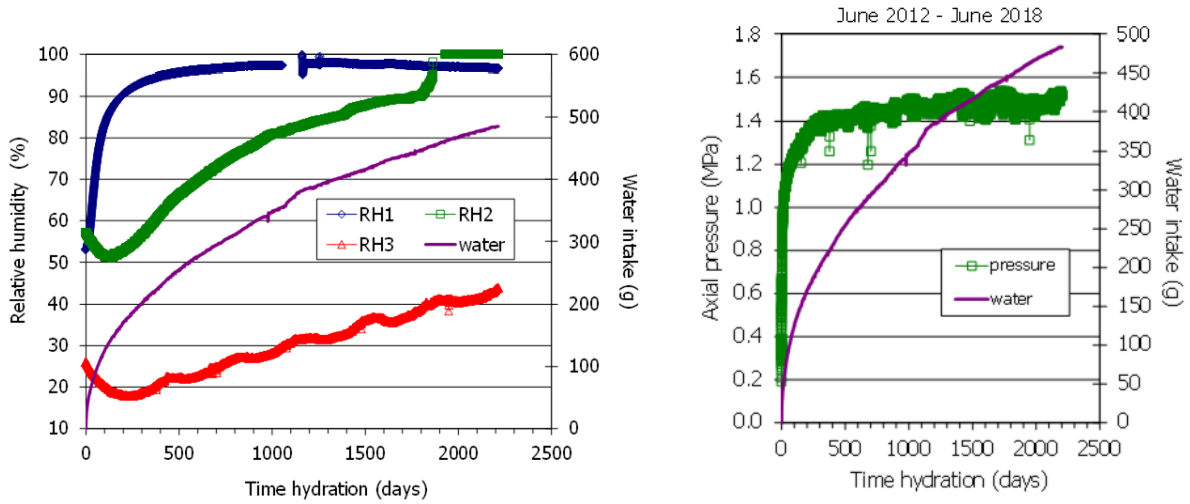

a) b)

Figure 16: *a) Evolution of water intake and relative humidity after the start of hydration (RH1 at 40 cm, RH2 at 22 cm and RH3 at 10 cm from the heater). b) Evolution of axial pressure and water intake after the start of hydration*

3.1.6 Requested results

The following results of the model are requested:

- Evolution of temperatures in sensors T1, T2 and T3 from time *t=0* to the end of the test (the laboratory temperature fluctuations can be disregarded).
- Evolution of relative humidity in sensors RH1, RH2 and RH3 from time *t=0* to the end of the test.
- Evolution of water intake from time *t=0* to the end of the test.
- Evolution of axial pressure from time *t=0* to the end of the test.
- Distributions of dry density, water content and degree of saturation along the column at the end of the test (from dismantling data)

3.2 Small scale experiment by CTU-SURAO

3.2.1 Overview – short description of the benchmark experiment

Material used: BCV bentonite (Ca-Mg type) - powder
Material treatment (sample preparation for test): Manually gentle compacted powder Initial water content equal as in delivered material (12.8 %) Final dry density before start of the experiment: 949 $kg.m^{-3}$
Temperature and pressure (at which measurement/test is carried out) 150 °C at the bottom of vessel, room temperature at the top To avoid the boiling, the pressure of 6 bar is applied on the top (saturation side)
Tests carried out (name, description, sample preparation, procedure, results): Small scale experiment is based on laboratory testing of bentonite subjected to high temperature while hydrating. The experiment consists of the vessel and measurement system. Bentonite is placed into constant volume cylindrical steel vessel with heater in the bottom and forced saturation on the top. Temperature gradient is applied. The final temperature will be 150°C at the bottom, while the rest of the apparatus is subject to laboratory temperature. On 05/21 the material has been loaded by 120 °C the next step is the final temperature 150°C. Two runs of approximately one-year duration are expected. After each run, the experiment will be dismantled and samples analysed as part of T3.1
Schedule and past and future date(s) of results delivery: Equipment preparation and tests 05/19 - 11/20 Results for first run (samples for T3.1): 05/22 Results for second run (samples for T3.1): 07/23

3.2.2 Introduction

The purpose of the experiment is to obtain characteristics of bentonite after subjecting it to high temperature (150 °C) while forced saturation is applied (6 bar). The data obtained in the benchmark experiment are supposed to be used in the mathematical modelling part of Subtask 3.3. The aim of the benchmark is to get information necessary for simulation of THM processes occurring in the bentonite at the overall constant volume conditions, while both thermal load and forced saturation pressure is active. The other purpose is to verify the measurements from subtask T3.1 at a larger scale.

The benchmark experiment is performed by CTU since December 2020 and it has been be in operation until 2022 when it will be dismantled and the material will be analysed. The laboratory analysis will be carried out as a part of subtask 3.1. Once the experiment is dismantled the second run will be prepared and initiated.

3.2.3 Material

To keep the consistency throughout the work package tasks, the same material as in the Tasks 2 and 3 has been employed. It is Czech bentonite from Cerny Vrch deposit in a powder state, denoted as BCV. The properties of the material are described in detail in Hausmannová (2018).

The values of hydraulic conductivity and swelling pressures plotted against dry density are shown in figure 17 and figure 18. The data were obtained from various projects, including Task 3.1 of this project.

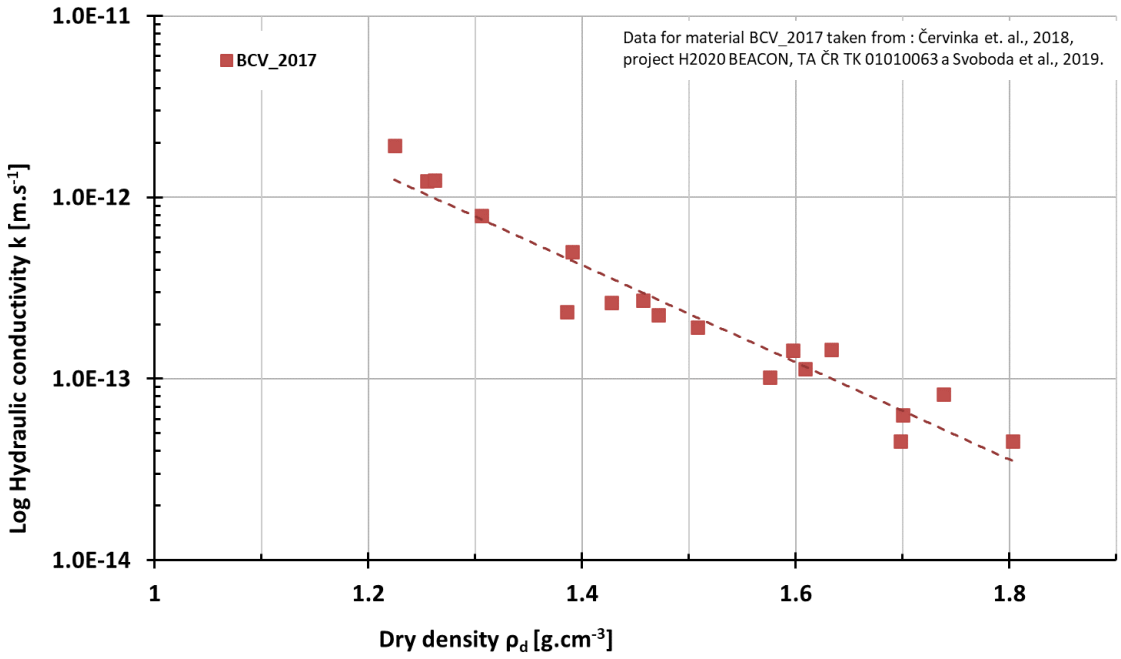

Figure 17: *The hydraulic conductivity of BCV material*

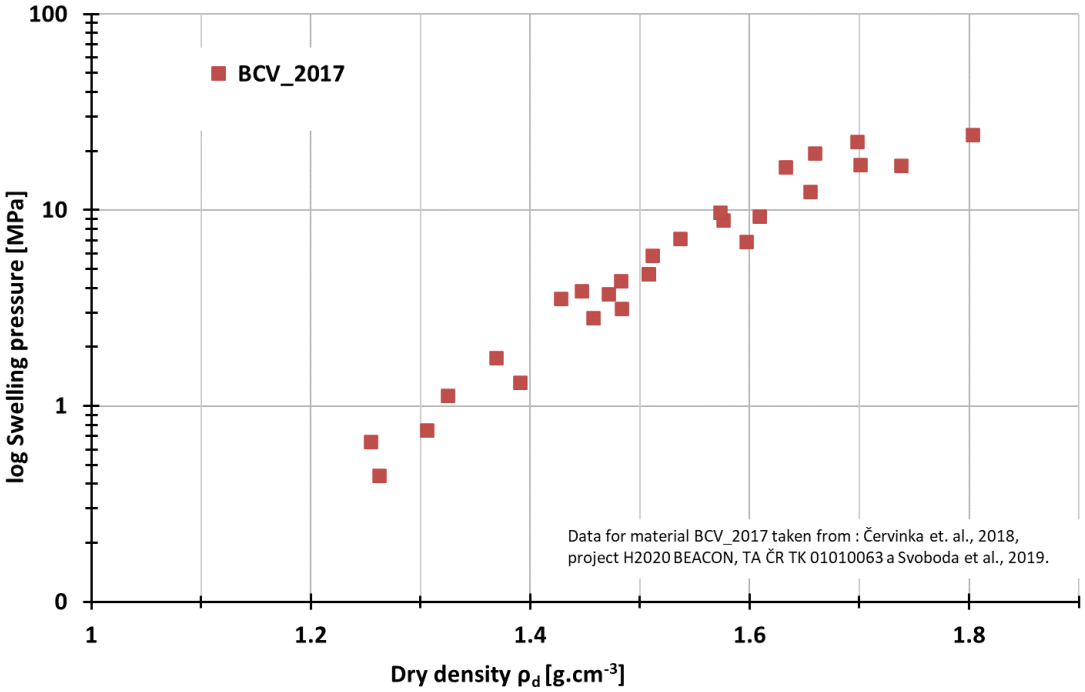

Figure 18: *The swelling pressures of BCV material*

3.2.4 Description of experimental set-up

The testing is carried out in specially designed cylindrical vessel of constant volume, which allows thermal loading of the sample and at the same time forced saturation. The saturation is applied at the top (with the rest of the sample closed to water and vapour) and thermal loading of 150°C is carried out at the bottom, therefore the sample is subject to thermal gradient.

The body of the vessel consists of stainless steel tube of 300 mm in diameter and 300 mm in length. There are welded thin flanges on both sides of the tube - at the top and at the bottom. The lid and the bottom are composed of blind (solid) flanges. The vessel is closed by tightening the lid to the tube flange by threaded rods with nuts, while six of the rods are tightened to the bottom flange (Figure 19).

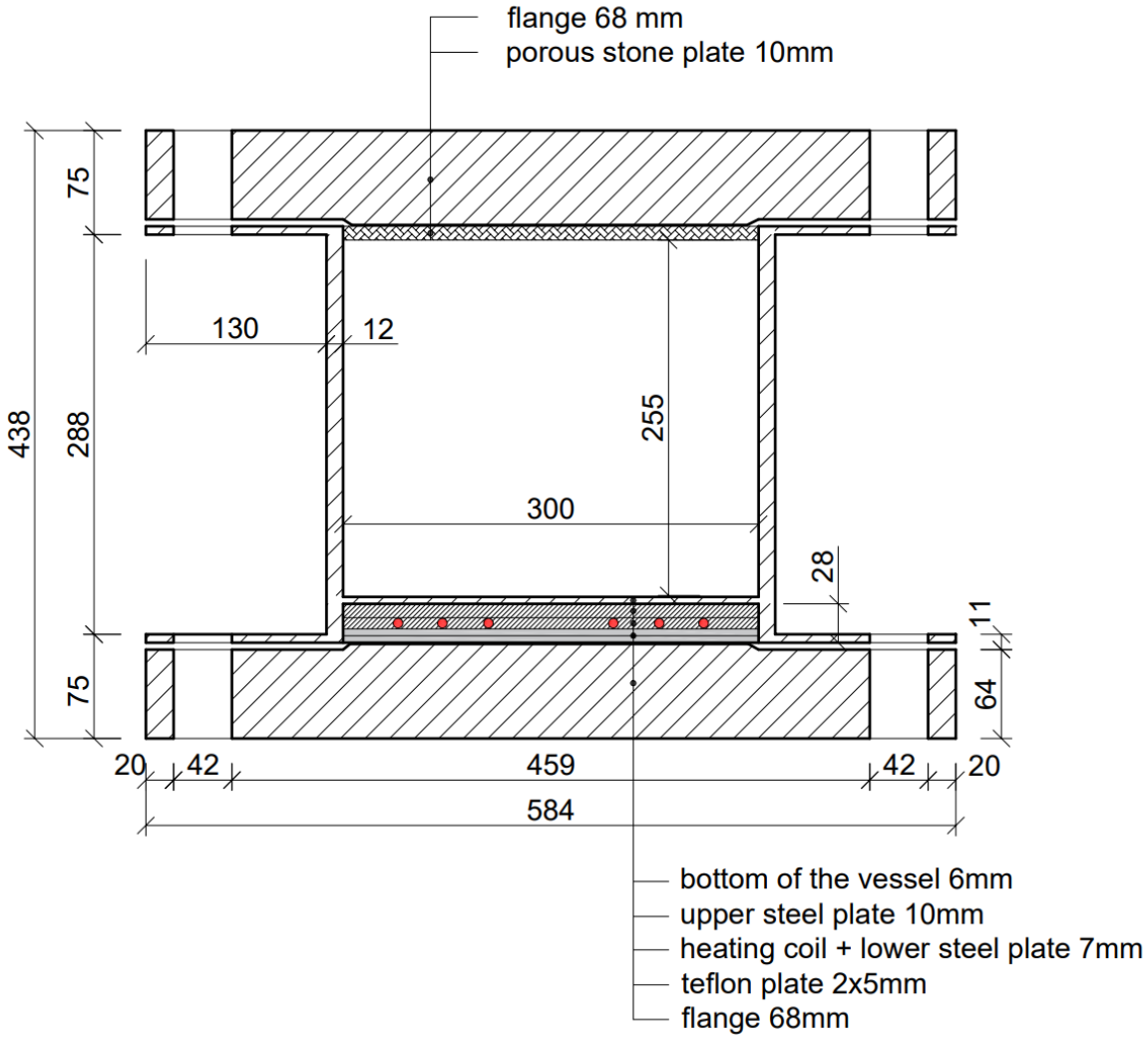

Figure 19: *Schema of little mock up experiment*

The thermal loading is provided by heater placed in the bottom of the vessel. The heater consists of electric resistance coil accommodated in groove milled in steel plate and covered by top steel plate. Two Teflon PTFE plates are placed at the bottom of the heating composition as thermal insulation. The heating set is screwed on the lower blind flange. The content of the vessel is separated from the heater by stainless steel plate welded inside the tube directly above the heater.

The space for the specimen is constrained by the tube on the sides, steel plate welded on the tube above the heater and porous stone of 10 mm of thickness placed under the lid. The effective inner diameter is 300 mm and effective height is 255 mm. The volume of the vessel is 0.018 m^3.

Forced saturation of the bentonite is provided by system consisting of two pressure bottles. One bottle with air serves as a pressure source, other with distilled water serving as gas – water exchanger. Required pressure is set and maintained by regulation valve on the output of air bottle. The water is fed from gas/water exchanger into vessel via steel pipe of 8 mm of diameter through the lid (Figure 20 and Figure 21). Saturation takes place through the aperture in the centre of the lid of the vessel and the uniform distribution of the water is arranged by porous stone under the lid.

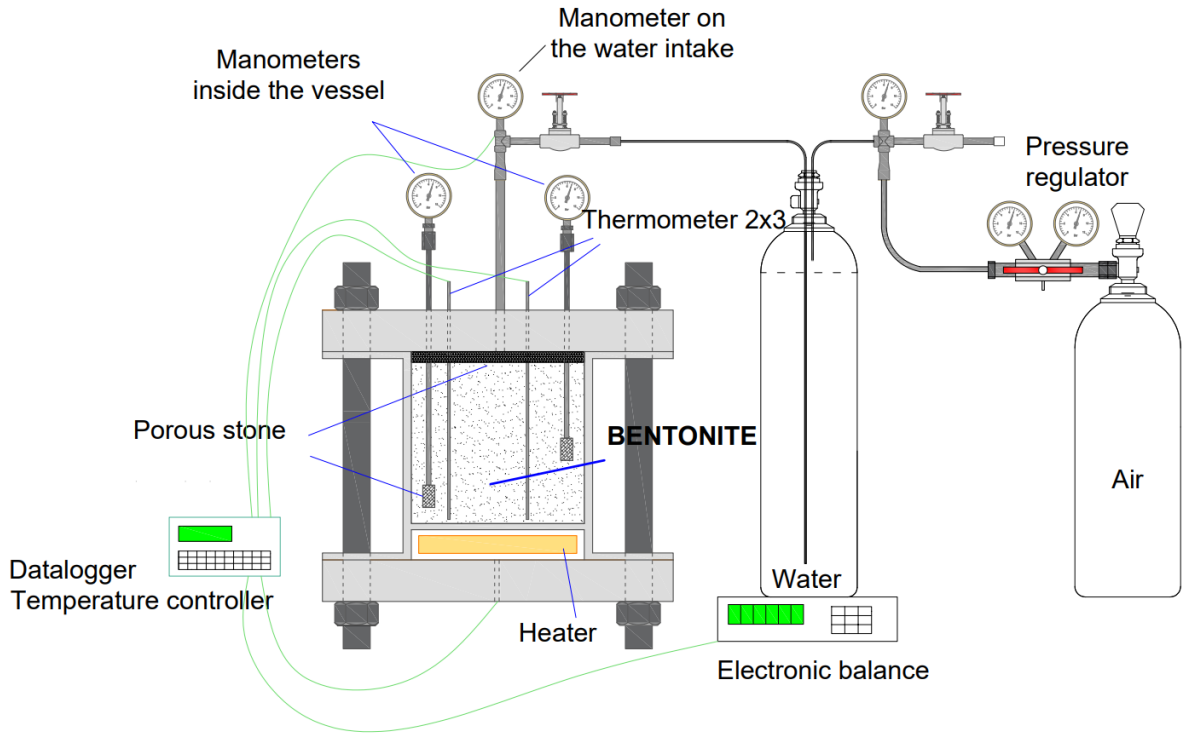

Figure 20: *Schematic illustration of the little mock-up experiment*

Figure 21: *Left side: The experiment set up. Right side: The vessel*

There are 9 apertures of 8 mm of diameter drilled through the lid, 8 are designated for instrumentation, one, in the centre serves for saturation. Only 4 instrumentation ports and one port for saturation are in operation, the others are hermetically sealed.

The instrumentation consists of 6 thermometers and 2 manometers with input filters placed inside the vessel (Figure 22). The thermometers are using two ports. Each is equipped with probe measuring temperature 3 different vertical levels. The measurement of vapor pressure takes place in two different points and two different vertical levels. There are 9 thermometers on the surface of the vessel and 1 manometer on the system of hydration. The temperature of the heater is controlled by the PID controller depending on temperature measured inside the heater. The water intake is calculated from

measurement of gas – water exchanger weight by electronic balance. Vapour pressure inside the bentonite, the power supplied and relative humidity of the room are measured periodically. The temperature inside the bentonite and on the surface of the vessel, saturation pressure and water intake (in form of weight) are measured continuously. The complete list of the sensors is shown in table 2

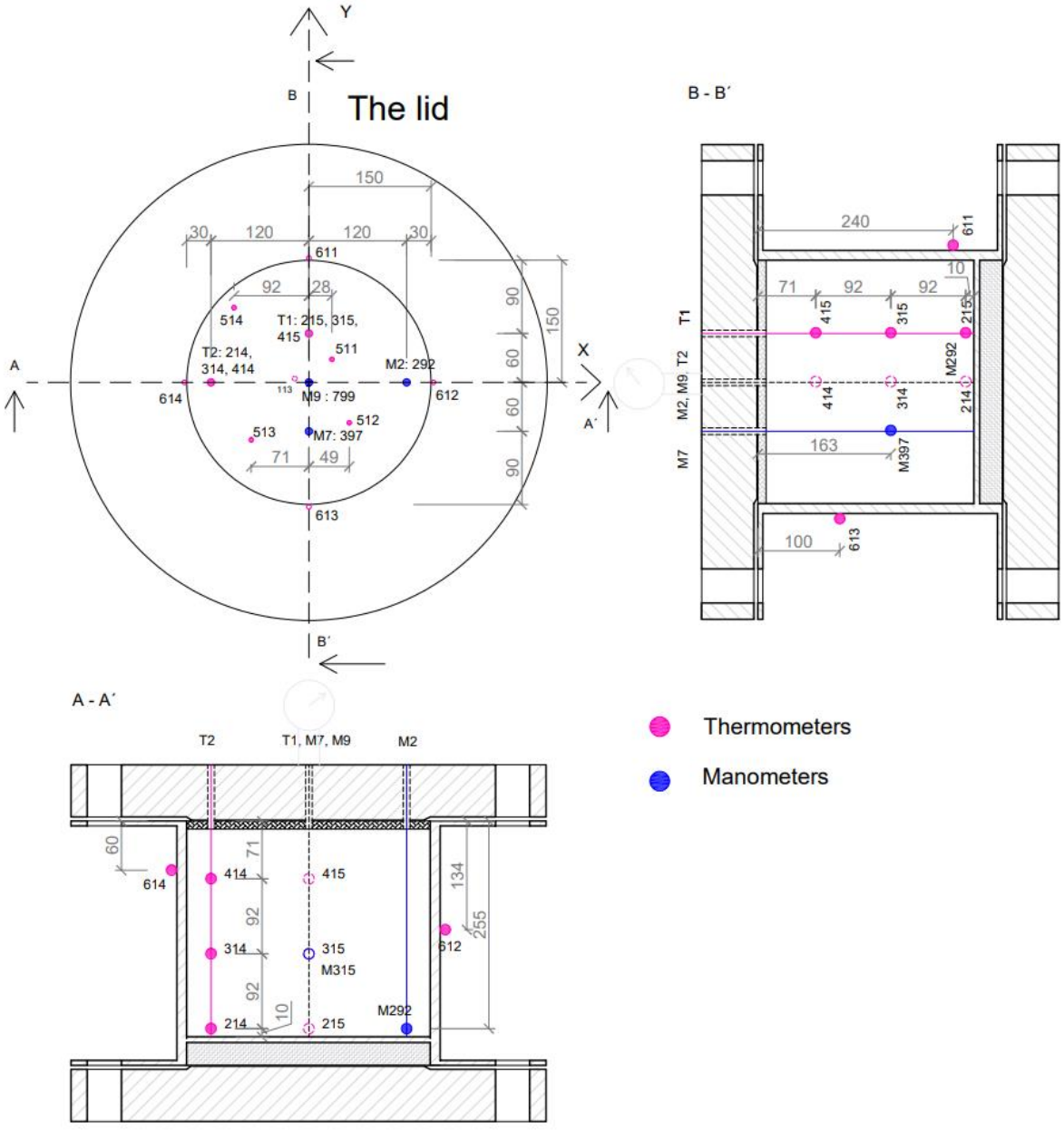

Figure 22: *Schema of the instrumentation*

Table 2: *List of employed sensors*

Number	Type of sensor	Description	Coordinates			Position
			z [mm]	r [mm]	alfa [°]	
113	Thermometer	controller - analog temperature sensor	270	18	345	on the heater
214	Thermometer	analog temperature sensor	255	120	270	inside the vessel
215	Thermometer	analog temperature sensor	255	60	0	
292	Manometer	manometer - vapor pressure	255	120	90	
314	Thermometer	analog temperature sensor	163	120	270	
315	Thermometer	analog temperature sensor	163	60	0	
397	Manometer	manometer - vapor pressure	163	60	180	
414	Thermometer	analog temperature sensor	71	120	270	
415	Thermometer	analog temperature sensor	71	60	0	
511	Thermometer	analog temperature sensor	-70	40	45	on the lid - 1. quadrant
512	Thermometer	analog temperature sensor	-70	70	135	on the lid - 2. quadrant
512	Thermometer	analog temperature sensor	-70	100	225	on the lid - 3. quadrant
514	Thermometer	analog temperature sensor	-70	130	315	on the lid - 4. quadrant
611	Thermometer	analog temperature sensor	240	150	0	on the shell of the vessel
612	Thermometer	analog temperature sensor	134	150	90	
613	Thermometer	analog temperature sensor	100	150	180	
614	Thermometer	analog temperature sensor	60	150	270	
799	Saturation pressure	digital manometer	-70	0	0	on the water intake
790	Electronic balance	measurement of the weight of water intake				under the saturation water bottle
800	Power supply analyser	power supply measurement				cabel line of the heater

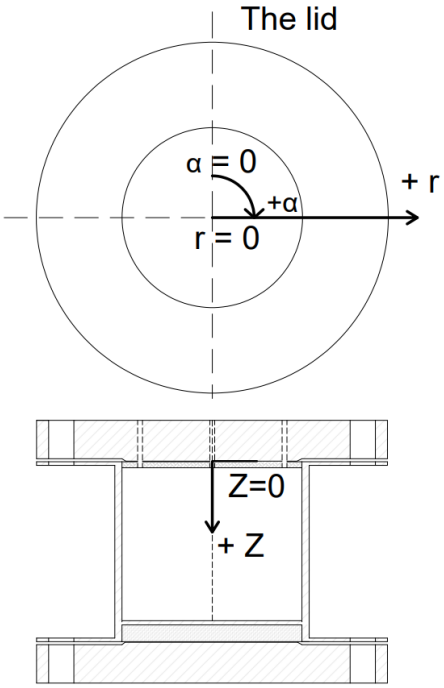

Figure 23: *Coordinate system of the instrumentation*

3.2.5 Preparation of the material

Powdered Czech BCV is tested in the experiment. The aim of the first run of the tests was to test bentonite in bulk loose state. The material was placed into the vessel in the manufactured powdered state. The initial water content of bentonite corresponding to hygroscopic humidity at laboratory

conditions was 12.8 %. The material was placed into the cell in portions of approximately 1.5 kg. Each of the portions was weighted exactly by an electronic balance. The total weight of the bentonite was 19.297 kg. Gentle manual compaction was applied. The dry density, computed taking in account the initial water content, was 949.07 kg.m^{-3}. The main features of the specimen after installation are summarized in table 3. The vessel had been filled-up by bentonite and then the top porous stone plate with drilled apertures for instrumentation was placed on. The instrumentation probes had been placed to their positions in the lid and then the vessel was closed using the frame crane. Because of low final dry density of the specimen it was not necessary to make boreholes in the bentonite for the instrumentation in advance. The assembly was weighted before applying the material and after. Because of very high total weight of the assembly (402.9 kg), the weighting was provided by frame crane and serves for excluding the gross errors in weighting of the tested material (higher accuracies cannot be reached at such a high total weight).

Table 3: *Main features of the specimen after installation*

material	powdered BCV	weight [kg]	19.297
height [mm]	255	dry density [kg.m^{-3}]	949.07
diameter [mm]	300	void ratio [%]	64.80
volume [m^3]	0.018	initial water content [%]	12.80

3.2.6 Experimental procedure

The first phase of the experiment consisted of saturation at laboratory temperature. The aim was to reach the pressure of 6 bar inside the vessel at first, which was necessary for no- boiling state of the liquid inside the vessel during subsequent thermal loading of 150 °C. Once the required pressure had been reached, the thermal loading started.

The hydration started on 03/12/2021. The saturation pressure had gradually been increased up to 6 bar, which was reached on 28/01/2021. The thermal loading started after the observed features stabilized on 02/02/2021 while maintaining the saturation pressure to 6 bar. The whole procedure of temperature increase and reaction of the monitored variables is shown in figure *24*. The heater had been set to 90°C first. After stabilization of the monitored variables the temperature was increased to 120°C which is the current state. At this moment (05/2021), the monitored variables have stabilized and the experiment is ready for temperature increase to its final value of 150°C, which will take place on 06/2021.

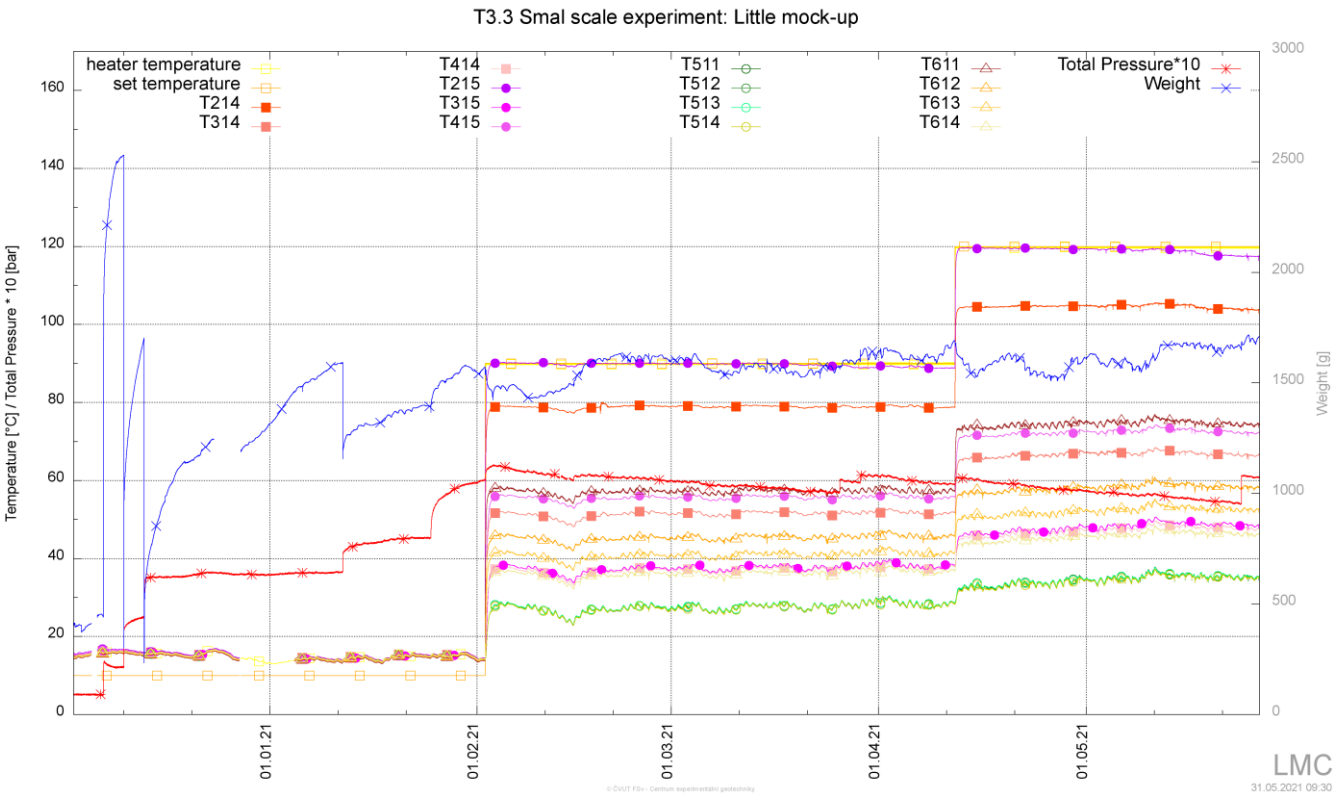

Figure *24*: *The progress of saturation and thermal loading*

3.2.7 Progress and observations

When the experiment was running (05/2021), the thermal loading while maintaining forced saturation is taking place. From the available observation, it is possible to conclude that the system reacts immediately to increase in the temperature and the temperature field stabilizes within few hours. It can be noted that much of the weight increase occurs instantly as reaction on increase in saturation pressure, mostly during the first phase of the experiment. Current overall degree of saturation computed using the water consumption data is 72.7 %.

The experiment will be in operation for one year with stable hydraulic and thermal conditions of forced saturation and thermal loading of 150 °C.

Once the experiment is finished, it will be dismantled and the material will be analyzed. The specimen itself will be analyzed as a part of subtask T3.1. The parameters to be tested are the following:

- Analysis of the water content field
- Saturated hydraulic conductivity on set of samples
- Swelling pressures on set of sampless

4. Benchmark cases for non-isothermal multiphase flow and reactive transport for radioactive waste disposal

4.1 Main features of the benchmark cases

The main features of the selected benchmark cases for non-isothermal multiphase flow and reactive transport for radioactive waste disposal include:

1) Multiphase flow and solute transport with liquid, gas and solid phases.
2) Non-isothermal conditions: heat source at around 100ºC.
3) Water evaporation near a heating source: phase change.
4) List of gases: air, water vapour, and reactive gases such as O_2, CO_2 and H_2.
5) Chemical reactions: aqueous complexation, acid-base, redox, mineral dissolution/precipitation, cation exchange and gas dissolution/exsolution.
6) Materials: metallic canister, bentonite, concrete and the host rock (granite or clay).
7) Geometry: 1D parallel or 1D axi-symmetric.

Figure 25 shows a schematic diagram of the thermal and hydrodynamic conditions in the initial heating and hydration stage of a radioactive waste repository.

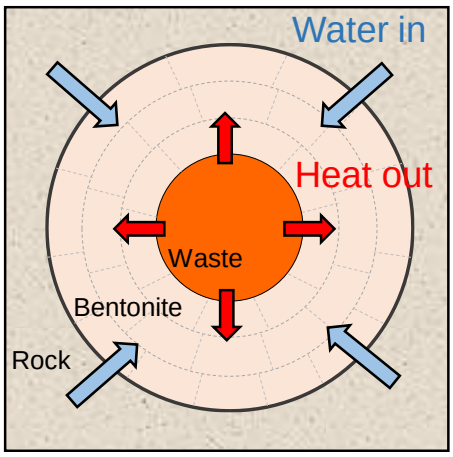

Figure 25: Schematic diagram of the thermal and hydrodynamic conditions in the initial heating and hydration stage of a radioactive waste repository.

4.2 Selected benchmark cases

Two simulation benchmark cases have been selected for the non-isothermal multiphase flow and reactive transport benchmark for radioactive waste disposal. These cases are the following

1) The FEBEX in situ test: 1D model. Unsaturated bentonite. Strong thermal gradients. Water evaporation in the heater and vapour condensation. Other gases: dry air, CO_2 and H_2. Materials: Bentonite and granite. Geochemical processes: aqueous reactions, mineral dissolution & precipitation, cation exchange and gas dissolution & ex-solution.

2) Long-term canister corrosion. 1D flow and multicomponent reactive solute transport model to simulate canister corrosion, the interactions of corrosion products with bentonite and the long-term hydrochemical evolution of porewater composition in the near field of a repository in fractured granite. Thermal gradient, water evaporation and vapour condensation could be less relevant. Other gases: H_2.

4.3 Preliminary list of partners and computer codes

Several teams have shown interest in participating in such benchmark. *Table 4* lists the teams and computer codes to be used for the non-isothermal multiphase flow and reactive transport for radioactive waste disposal. The participation of the teams at the benchmark could be as participant or observer.

Table 4 – List of teams and computer codes to be used for the non-isothermal multiphase flow and reactive transport for radioactive waste disposal.

Participant	Modeling tool	DONUT partner	Type of participation	Contact person
UDC	INVERSE-FADES-CORE	Yes	Producer	J. Samper A. Mon
University of Pau	Reactive-DuMuX	Yes	Producer	Brahim Etienne
Jilin University	TOUGHREACT	No	Producer	Tianfu Xu
TUL (Tech Univ Liberec)	FEFLOW & PHREEQC	Yes	Testing	
LEI	COMSOL-PHREEQC	Yes	Testing	
SCK-CEN	OpenGeoSys (OGS) (to be confirmed)	Yes	Testing	
PSI		No	Observer	
Paris Mines Tech		No	Observer	

4.4 Planning and schedule of the benchmark

Table 5 shows the planning and schedule of the non-isothermal multiphase flow and reactive transport for radioactive waste disposal from March 2022 to December 2023.

Table 5 - Planning and schedule of the non-isothermal multiphase flow and reactive transport for radioactive waste disposal

Date	**Milestone**
March to June 2022	Selection of the benchmark case and definition of the different benchmark levels of complexity.
June 2022 to February 2023	Preliminary benchmark simulation by benchmark leaders (preliminary results are shown later in the document)
February 2023 to June 2023	Resolution of the benchmark by the different teams and exchange of information.
June 2023	Workshop to discuss the results.

June to October 2023	New calculations, if necessary, based on the workshop outcome.
October to December 2023	Wrap up of common publications

5. Benchmark case 1: Febex in situ test

5.1 Multiphase mathematical formulation

This section presents the mathematical formulation of the coupled THC model. This formulation has been extracted from Zheng et al. (2011).

It is assuming no deformation. Water mass balance is given by Navarro and Alonso (2000):

$$\frac{\partial m^w}{\partial t} + \nabla \cdot \left(\rho^l X_l^w \boldsymbol{q}^l + \rho^g X_g^v \boldsymbol{q}^g + \boldsymbol{j}_v\right) + r^w = 0 \quad (1)$$

where$\nabla \cdot ( )$ is the divergence operator, ρ^l and ρ^g are the bulk densities of the liquid and gaseous phases (kg/m^3), respectively, X_l^w is the mass fraction of water in the liquid phase, X_g^v is the mass fraction of the vapor in the gas phase, r^w is the sink/source term of liquid water, $\boldsymbol{q^l}$ is the vector of volumetric liquid flux (m/s) which is given by Eq. 15, $\boldsymbol{q^g}$ is the vector of volumetric gas flux (m/s), which is given by Eq. 16, $\boldsymbol{j_v}$ is the dispersive mass flux of vapor with respect to the mean gas velocity (kg/m^2/s), which is given by Eq. 17, and m^w is the mass of water per unit volume of porous medium (kg/m^3), which is given by:

$$m^w = \emptyset\left[\rho^l X_l^w S_l + \rho^g X_g^v (1 - S_l)\right] \quad (2)$$

where $\emptyset$ is the porosity and S_l is the liquid saturation degree. The dispersive mass flux of air and water with respect to the liquid phase are neglected.

The gas mass balance equation is given by:

$$\frac{\partial m^g}{\partial t} + \nabla \cdot (\rho^g \boldsymbol{q^g}) + r^g = 0 \quad (3)$$

where and m^g is the mass of gas per unit volume of porous medium (kg/m^3) and r^g is the sink/source term of gas. The dispersive mass flux of air and the gas with respect to the gaseous phase are neglected.

The air mass balance equation is given by:

$$\frac{\partial m^a}{\partial t} + \nabla \cdot \left(\rho^g X_g^a \boldsymbol{q^g} + \rho^l X_l^a \boldsymbol{q^l}\right) = 0 \quad (4)$$

where X_g^a is the mass fraction of air in the gaseous phase, X_l^a is the mass fraction of air in the liquid phase, and m^a is the mass of air per unit volume of porous medium (kg/m^3) which is given by:

$$m^a = \emptyset\left[\rho^g X_g^a (1 - S_l) + \rho^l X_l^a S_l\right] \quad (5)$$

If the coefficient of the thermal expansion of the solid particles (1/ºC), C_T^s, is considered and the mechanical compressibility of the particles C_p^s is disregarded (C_T^s >> C_p^s), then the solid mass balance becomes:

$$\frac{\partial \emptyset}{\partial t} = (1 - \emptyset)\left[-C_T^s \frac{\partial T}{\partial t}\right] \quad (6)$$

where T is the temperature (ºC).

Our formulation assumes that all phases are at local thermal equilibrium and therefore they are all at the same temperature. Hence, the energy balance is described in terms of an equation of internal energy, which is defined by the following balance of enthalpy:

$$\frac{\partial h}{\partial t} + \nabla \cdot (-\Lambda \cdot \nabla T + \boldsymbol{I^e}) = 0 \tag{7}$$

where h is the average specific enthalpy of the soil (J/m^3), which in turn is given by:

$$h = \rho^l X_l^w \emptyset S_l h^w + \rho^g X_g^v \emptyset (1 - S_l) h^v + \rho^g X_g^a \emptyset (1 - S_l) h^a + \rho^l X_l^a \emptyset S_l h^a + \rho^s (1 - \emptyset) h^s \tag{8}$$

where h^w, h^v, h^a and h^s are the specific enthalpies of free water, vapor, air and solid particles respectively, which are assumed to depend linearly on temperature and specific heat (Navarro and Alonso, 2000):

$$h^w = c_w (T - T_o) \tag{9}$$

$$h^v = c_v (T - T_o) + h_o^v \tag{10}$$

$$h^a = c_a (T - T_o) \tag{11}$$

$$h^s = c_s (T - T_o) \tag{12}$$

where c_w, c_v, c_a and c_s are the specific heat at the temperature T_o of the liquid, vapor, air and solid, respectively; and h_o^v is the specific enthalpy of water vapor at temperature T_o.

$\boldsymbol{I^e}$ is the vector of convective energy flux, which is given by:

$$\boldsymbol{I^e} = \rho^l X_l^w h^w \boldsymbol{q^l} + \rho^g X_g^v h^v \boldsymbol{q^v} + \rho^g X_g^a h^a \boldsymbol{q^g} \tag{13}$$

where $\boldsymbol{q^v}$ is the vector of volumetric vapor flux (m/s), which is given by the last terms of Eq. 1, that is, $\rho^v \boldsymbol{q^v} = \rho^g X_g^v \boldsymbol{q^g} + \boldsymbol{j^v}$ and $\boldsymbol{\Lambda}$ is the bulk thermal conductivity tensor (W/m^{o}C), which for unsaturated bentonite is computed as a volume-weighted average of the conductivities of the components according to:

$$\boldsymbol{\Lambda} = \emptyset S_l \boldsymbol{\Lambda^w} + X_l^a \emptyset S_l \boldsymbol{\Lambda^a} + \emptyset (1 - S_l)(\boldsymbol{\Lambda^v} + \boldsymbol{\Lambda^a}) + (1 - \emptyset)\boldsymbol{\Lambda^s} \tag{14}$$

where $\boldsymbol{\Lambda^w}$, $\boldsymbol{\Lambda^v}$, $\boldsymbol{\Lambda^a}$ and $\boldsymbol{\Lambda^s}$ are the thermal conductivities of water, vapor, air and solid, respectively. This equation is inspired in the formulation of De Vries's (1963), which according to Tang et al. (2008) provides the best fit to measured thermal conductivity data for several bentonites such as FEBEX bentonite. The formulation in Eq. 14, however, may not be the appropriate for courser porous materials. According to Soler (2001), the Dufour effect is negligible compared to thermal conduction and, therefore, can be disregarded.

The volumetric liquid flux, $\boldsymbol{q^l}$, is given by:

$$\boldsymbol{q^l} = -\frac{\boldsymbol{K^{il}} k^{rl}}{\mu^l} (\nabla p^l + \rho^l g \nabla z) \tag{15}$$

where p^l is the liquid pressure (Pa), $\boldsymbol{K^{il}}$ is the intrinsic permeability tensor of the liquid (m^2), k^{rl} is the relative permeability of the liquid, μ^l is the viscosity of the liquid (kg/m/s), z is the elevation. The volumetric gas flux, $\boldsymbol{q^g}$, is given by:

$$\boldsymbol{q^g} = -\frac{\boldsymbol{K^{ig}} k^{rg}}{\mu^g} (\nabla p^g + \rho^g g \nabla z) \tag{16}$$

where $\boldsymbol{K^{ig}}$ is the intrinsic permeability tensor of the gas (m^2), k^{rg} is the relative permeability of gas, μ^g and is the viscosity of the gas phase (kg/m/s).

The dispersive mass flux of vapor, $\boldsymbol{j^v}$, is calculated by the Fick's law:

$$\boldsymbol{j^v} = -\rho^g \boldsymbol{D^v} \nabla X_g^v \tag{17}$$

where $\boldsymbol{D^v}$ is the hydrodynamic dispersion tensor for vapor (m^2/s) which includes the effects of mechanical dispersion (D_{disp}) and molecular diffusion (D_e^v). The effective molecular diffusion coefficient for the vapor was calculated from Pollock (1986):

$$D_e^v = \frac{5.9 \cdot 10^{-6} \tau^v (T + 273.15)^{2.3}}{p^g} \tag{18}$$

where τ^v is the vapor tortuosity factor (dimensionless), T in Celsius.

It should be noticed that in the model the gases dissolved in water (air and other gases) are transported by advection and dispersion in the fluid phase together with liquid water.

Solute transport processes include advection, molecular diffusion, and mechanical dispersion. Each of them produces a solute flux per unit surface and unit time. There are as many transport equations as primary chemical species or aqueous components in the system. The primary species are the building blocks of chemical systems of interest, upon which concentrations of secondary species are written through laws of mass action for reactions at thermodynamic equilibrium. Advection refers to solute migration associated to the volumetric liquid flux, $\boldsymbol{q^l}$. The advective solute flux, $\boldsymbol{F_A}$, is given by:

$$\boldsymbol{F_A} = \rho^l X_l^w \boldsymbol{q^l} C_j. \tag{19}$$

where C_j is the total dissolved concentration of the of j-th species (mol/L).

Molecular diffusion in pure water $\boldsymbol{F_D}$, produces a mixing effect which obeys Fick's law:

$$\boldsymbol{F_D} = -\rho^l X_l^w D_0^j \nabla C_j. \tag{20}$$

Where D_0^j is the molecular diffusion coefficient in pure water of the j-th specie. In a porous medium the porewater molecular diffusion, D_m, is related with the molecular diffusion in pure water, D_o, through:

$$D_m = S_l \emptyset D_o \tau \tag{21}$$

where τ is the medium tortuosity. For partially saturated porous media, tortuosity is related to water content through relationships such as (Millington and Quirk ,1961):

$$\tau = \frac{\theta_l^{7/3}}{\emptyset^2} \tag{22}$$

Therefore, the diffusive flux in a porous media is given by:

$$\boldsymbol{F_D} = -\rho^l X_l^w D_m^j \nabla C_j = .-\rho^l X_l^w \theta_l \tau D_o^j \nabla C_j \tag{23}$$

The hydrodispersive flux, $\boldsymbol{F_H}$, can be described as:

$$\boldsymbol{F_H} = .-\rho^l X_l^w \theta_l \boldsymbol{D_h} \nabla C_j \tag{24}$$

The hydrodynamic dispersion, $\boldsymbol{D_h}$, is a symmetric tensor which components in two dimensions D_{xx}, D_{yy} and D_{xy} are the following:

$$D_{xx} = \frac{\alpha_L v_x^2 + \alpha_T v_y^2}{|v|} \tag{25}$$

$$D_{yy} = \frac{\alpha_L v_y^2 + \alpha_T v_y^2}{|v|} \tag{26}$$

$$D_{xy} = D_{xy} = (\alpha_L - \alpha_T)\frac{v_x v_y}{|v|} \tag{27}$$

where α_L and α_T are the longitudinal and transversal dispersivities, v_x and v_y are the velocity components in two dimensions, and $|v|$ is the velocity magnitude.

The dispersion coefficient $\boldsymbol{D^j}$ (m²/s) includes the hydrodynamic or mechanical dispersion, $\boldsymbol{D_h}$, and the porewater molecular diffusion, D_m.Then, the dispersion coefficient $\boldsymbol{D^j}$, can be expressed as the following relation:

$$\theta \boldsymbol{D^j} = \boldsymbol{I} D_m + \theta \boldsymbol{D_h} \tag{28}$$

where **I** is the identity tensor.

The mass balance equation for the j-th primary species is given by:

$$\frac{\partial\left(\rho^l X_l^w \theta_l C_j\right)}{\partial t} = -\nabla \cdot (\boldsymbol{F_A} + \boldsymbol{F_D} + \boldsymbol{F_H}) + r_j' \tag{29}$$

where r_j' is the gas sink/source term, which includes the chemical reactions term, R_j (mol/m³/s), the water mass flux (kg/m³/s) source entering (r_j) or sink leaving (r_0) the system, according to:

$$r_j' = r_j C_j^0 + r_0 C_j + R_j \tag{30}$$

where C_j^o is the external concentration of the j-th solute species in the entering water flux.

Substitution of mass fluxes $\boldsymbol{F_A}$, $\boldsymbol{F_D}$ and $\boldsymbol{F_H}$ into equation (29) and taking into account equation (28) leads to:

$$\frac{\partial\left(\rho^l X_l^w \theta_l C_j\right)}{\partial t} = -\nabla \cdot \left(\rho^l X_l^w \boldsymbol{q^l} C_j - \rho^l X_l^w \theta_l \boldsymbol{D^j} \nabla C_j\right) + r_j' \tag{31}$$

Expanding the mass term and the advective transport term and reordering the Eq. (31), the following equation can be rewritten as:

$$\frac{\partial(\rho^l X_l^w \theta_l)}{\partial t} C_j + \rho^l X_l^w \theta_l \frac{\partial(C_j)}{\partial t} = -\rho^l X_l^w \boldsymbol{q^l} \nabla C_j - C_j \nabla \cdot \left(\rho^l X_l^w \boldsymbol{q^l}\right) + \nabla \cdot \left(\rho^l X_l^w \theta_l \boldsymbol{D^j} \nabla C_j\right) + r_j' \tag{32}$$

The following identity derived from the water mass balance in the liquid phase (Eq. 1) and multiplying by C_j, was taken into account.

$$\left(\frac{\partial m^w}{\partial t} + \nabla \cdot (\rho^l X_l^w \boldsymbol{q^l}) + (r_j - r_0) + (r_c - r_e)\right) C_j = 0 \tag{33}$$

where and r_c and r_e are the condensation and evaporation rates (kg/m³/s), respectively. The net effect of the evaporation/condensation rate (kg/m³/s), $(r_e - r_c)$, can be evaluated as:

$$(r_e - r_c) = \frac{\partial\left(\rho^g X_g^v \emptyset S_g\right)}{\partial t} + \nabla \cdot \left(\rho^g X_g^v \boldsymbol{q^g} + \boldsymbol{j^v}\right) \tag{34}$$

Therefore, substituting the Eq. (30) and Eq. (33) into Eq. (32), one has the mass balance equation for the j-th primary species:

$$\rho^l X_l^w \theta_l \frac{\partial(C_j)}{\partial t} = -\rho^l X_l^w \boldsymbol{q^l} \nabla C_j + \nabla \cdot (\rho^l X_l^w \theta_l \boldsymbol{D^j} \nabla C_j) + r_j(C_j^0 - C_j) + C_j(r_e - r_c) + R_j \quad (35)$$

Defining the transport operator $L^*(\,)$, as the following:

$$L^*(\,) = \nabla \cdot [m_l^w \boldsymbol{D^j} \cdot \nabla(\,)] - m_l^w \boldsymbol{q^l} \cdot \nabla(\,) + (r_e - r_c)(\,) \quad (36)$$

Finally, the mass balance equation for the j-th primary species is given by (Zheng and Samper, 2008):

$$m_l^w \frac{\partial C_j}{\partial t} + \frac{\partial(m_l^w P_j)}{\partial t} + \frac{\partial(m_l^w W_j)}{\partial t} + \frac{\partial(m_l^w G_j)}{\partial t} = L^*(C_j) + r_i(C_j^0 - C_j) \quad (37)$$

where C_j is the total dissolved concentration of the of j-th primary species (mol/L), m_l^w is the mass of liquid water per unit volume of medium (kg/m^3), which is equal to $\rho^l X_l^w \theta$, where $\theta = S_l \emptyset$ is the volumetric water content (m^3/m^3), P_j, W_j and G_j are the total precipitated minerals, the total exchanged and total dissolved gas concentrations (mol/L), respectively, of the j-th primary species, r_i is the sink term (kg/m^3/s), C_j^0 is the dissolved concentration of j-th species (mol/L) in the sink term r_i, N_c is the number of primary species.

The reactive transport of the f-th gas species was implemented as an additional mass balance equation of the f-th gas species in the gaseous phase. The gas mass balance accounts for: a) advection; b) molecular diffusion and c) mechanical dispersion.

The advection considers the movement of the gas species with the volumetric gas flux, $\boldsymbol{q_g}$ (m^3/s). The advective flux, $\boldsymbol{F_A^f}$, of the f-th gas species is given by:

$$\boldsymbol{F_A^f} = \rho^g \boldsymbol{q_g} C_f \quad (38)$$

where ρ^g is the gas density and C_f is the concentration of the of f-th gas species (mol/kg) in the gaseous phase.

The diffusive flux of the f-th gas species, $\boldsymbol{F_D^f}$, is given by Fick's Law according to:

$$\boldsymbol{F_D^f} = -\rho^g D_g^f \nabla C_f \quad (39)$$

where D_g^f is the diffusion coefficient of the f-th gas species in an ideal gaseous phase which according to Lasaga (1998) is given by:

$$D_g^f = \frac{RT}{3\sqrt{2}\pi P N_{avog} d^2} \sqrt{\frac{8RT}{\pi M}} \quad (40)$$

where P is the gaseous phase pressure, N_{avog} is Avogadro's number, and d and M are the molecular diameter and the molecular weight of the f-th gas species, respectively. In a partly saturated gaseous phase containing several gases, the molecular diffusion, D_m^f, is affected by the gaseous phase tortuosity, τ_g, and the volumetric gas content, θ^g ($\theta^g = S_g \emptyset$) according to:

$$D_m^f = \theta^g \tau_g D_g^f \quad (41)$$

The tortuosity in the gaseous phase, τ_g, is computed from (Millington and Quirk ,1961):

$$\tau_g = \frac{\theta_g^{7/3}}{\emptyset^2} \tag{42}$$

Combining Eq. (39) and Eq. (417), the diffusive flux in the gaseous phase is given by:

$$\boldsymbol{F_D^f} = -\rho^g \theta^g \tau_g D_g^f \nabla C_f \tag{43}$$

The dispersive transport by the mechanical dispersion, $\boldsymbol{F_H^f}$, is assumed to follow Fick's Law according to:

$$\boldsymbol{F_H^f} = -\rho^g \theta^g \boldsymbol{D_H^f} \nabla C_f \tag{44}$$

where $\boldsymbol{D_H^f}$ is the mechanical dispersion tensor similar to that of the liquid phase presented in Eq. (25), Eq. (26) and Eq. (27). The molecular diffusion, D_m^f, and the mechanical dispersion, $\boldsymbol{D_H^f}$, are commonly lumped into a single dispersion tensor, $\boldsymbol{D^f}$, according to:

$$\theta^g \boldsymbol{D^f} = \boldsymbol{I} D_m^f + \theta^g \boldsymbol{D_H^f} \tag{45}$$

where the $\boldsymbol{I}$, is the identity tensor.

The mass balance equation of the f-th gas species in the gaseous phase is given by:

$$\frac{\partial(\rho^g \theta^g C_f)}{\partial t} = -\nabla\left(\boldsymbol{F_A^f} + \boldsymbol{F_D^f} + \boldsymbol{F_H^f}\right) + r_f' \tag{46}$$

where r_f' is the gas sink/source term, which includes: the gas chemical reactions term, R_f (mol/m³/s), the gas mass flux (kg/m³/s) source entering (r_f^i) or sink leaving (r_f^o) the system, according to:

$$r_f' = r_f^i C_f^o - r_f^o C_f + R_f \tag{47}$$

where C_f^o is the external concentration of the f-th gas species in the entering gas flux. Substituting the Eq. (38), Eq (43) and Eq. (44) into Eq. (46) and taken into account Eq. (51), one has:

$$\frac{\partial(\rho^g \theta^g C_f)}{\partial t} = -\nabla\left(\rho^g \boldsymbol{q_g} C_f - \rho^g \theta^g \boldsymbol{D^f} \nabla C_f\right) + r_f' \tag{48}$$

Expanding the mass term and the advective transport term and substituting Eq (47), one has:

$$\rho^g \theta^g \frac{\partial C_f}{\partial t} + \frac{\partial(\rho^g \theta^g)}{\partial t} C_f = -\rho^g \boldsymbol{q_g} \nabla C_f - C_f \nabla\left(\rho^g \boldsymbol{q_g}\right) + \nabla\left(\rho^g \theta^g \boldsymbol{D^f} \nabla C_f\right) + r_f^i C_f^o - r_f^o C_f + R_f \tag{49}$$

The gas mass balance in the gaseous phase Eq. (3) reordered and multiplied by the concentration C_f is given by:

$$\left(\frac{\partial(\rho^g \theta^g)}{\partial t} + \nabla\left(\rho^g \boldsymbol{q_g}\right) + r_f^0 - r_f^i\right) C_f = 0 \tag{50}$$

Combining Eq (49) and Eq (50), the transport equation is given by:

$$\rho^g \theta^g \frac{\partial C_f}{\partial t} = -\rho^g \boldsymbol{q_g} \nabla C_f + \nabla\left(\rho^g \theta^g \boldsymbol{D^f} \nabla C_f\right) + r_f^i\left(C_f^o - C_f\right) + R_f \quad (51)$$

The gas transport equation can be rewritten in compact form as:

$$m_g \frac{\partial C_f}{\partial t} = L_f^*\left(C_f\right) + r_f^i\left(C_f^0 - C_f\right) + R_f \quad (52)$$

where m_g is the mass of gas per unit volume of medium (kg/m^3) which is equal to $\rho^g \theta^g$ and $L_f^*(\,)$ is the following transport operator:

$$L_f^*(\,) = \nabla \cdot \left[m_g \boldsymbol{D^f} \cdot \nabla(\,)\right] - \rho^g \boldsymbol{q^g} \cdot \nabla(\,) \quad (53)$$

The chemical conceptual model for compacted bentonite accounts for the following reactions: aqueous complexation, acid/base, redox, cation exchange, mineral dissolution/precipitation (at equilibrium or under kinetic control), gas dissolution/exsolution. The chemical system is defined in terms of the concentrations of the primary species. The concentrations of the secondary species are computed from the concentrations of the primary species through appropriate mass action laws. The concentrations of the precipitated, exchanged and adsorbed species are computed using similar equations. A detailed description of the calculations of the chemical reactions can be found in Samper et al. (2009) and Zheng et al. (2011). The Gaines-Thomas convention is used for cation exchange.

The total dissolved concentration, C_j, can be written in an explicit form as a function of the N_c primary species by applying the Mass-Action Law:

$$C_j = c_j + \sum_{k=1}^{N_x} \upsilon_{kj} x_j = c_j + \sum_{k=1}^{N_x} \upsilon_{kj} \left(K_k^{-1} \gamma_k^{-1} \prod_{i=1}^{N_c} c_{ki}^{\upsilon_{ki}} \gamma^{\upsilon_{ki}}\right) \quad (54)$$

where N_x is the number of the $x_j$secondary species; K_k is the equilibrium constant of the k-th secondary specie reaction; γ is the thermodynamic activity coefficient and υ_{kj} is the stoichiometric coefficient of the j-th primary specie on the k-th species.

The total concentration of the precipitated minerals of the j-th primary species, P_j, can be written as:

$$P_j = \sum_{m=1}^{N_p} \upsilon_{mj}^p p_m \quad (55)$$

where p_m is the concentration of the m-th mineral phase and υ_{mj}^p is the stoichiometric coefficient of the j-th primary specie on the m-th mineral. Under equilibrium conditions, dissolution-precipitation reactions can be described by the Law of Mass Action which states that:

$$X_m \lambda_m K_m = \prod_{i=1}^{N_c} c_i^{\upsilon_{mi}} \gamma_i^{\upsilon_{mi}} \quad (56)$$

where X_m is the molar fraction of the m-th solid phase; λ_m is the thermodynamic activity coefficient (X_m and λ_m are taken equal to 1 for pure phases); c_i and γ_i are the concentration and activity coefficient of the i-th specie; υ_{mi} is the stoichiometric coefficient in the dissolution reaction of the m-th solid phase; and K_m is the corresponding equilibrium constant.

The concentration of the i-th exchanged cation w_i (mol/L) can be obtained from the i-th equivalent fraction β_i, according to:

$$w_i = \beta_i \, CEC \, \rho_s \frac{(1-\phi)}{z_i 100 \phi} = \left(K_{ij}^*\right)^{-\nu_i} c_i \gamma_i \left(\frac{\beta_j}{c_j \gamma_j}\right)^{\upsilon_i / \upsilon_j} CEC \, \rho_s \frac{(1-\phi)}{z_i 100 \phi} \quad (57)$$

where CEC is the total cation exchange capacity (meq/100g); z_i is the cation charge and; K_{ij}^* is the exchange coefficient or selectivity.

The total concentration of the dissolved gases concentrations of the j-th primary species, G_j, can be written as:

$$G_j = \sum_{f=1}^{N_g} \upsilon_{fj}^g g_f \tag{58}$$

where g_f is the concentration of the f-th gas and υ_{fj}^g is the stoichiometric coefficient of the j-th primary specie on the f-th gas. For reactions involving aqueous and gas phase, the Law of Mass-Action states that:

$$p_f \Gamma_f K_f = \prod_{i=1}^{N_c} c_i^{\upsilon_{fi}} \gamma_i^{\upsilon_{fi}} \tag{59}$$

where p_f is the partial pressure of the f-th species in the gas phase; Γ_f is the activity coefficient and K_f is the equilibrium constant of the reaction, c_i and γ_i are the concentration and activity coefficient of the i-th dissolved primary specie, υ_{fi} is the stoichiometric coefficient of the f-th gas on the i-th specie. The gaseous phase is assumed as an ideal mixture and the fugacity constant, Γ_f is equal to 1.

The equilibrium constants for aqueous complexes and minerals depend on temperature under non-isothermal conditions. They are calculated with the following expression, which is valid for temperatures between 0 and 300 ºC:

$$logK(T) = \frac{b_1}{T^2} + \frac{b_2}{T} + b_3 lnT + b_4 + b_5 T \tag{60}$$

where b_1 to b_5 are coefficients, which are derived by fitting Equation 43 to measured $logK$ values at 0, 25, 60, 100 and 300ºC.The thermodynamic database of ThermoChimie v11.a (Giffaut et al., 2014).is used for aqueous complexes and minerals.

For the activity coefficients of the aqueous species the extended Debye-Hückel formula can be used:

$$log\gamma_i = -\frac{Az_i^2 (I)^{1/2}}{1 + Ba_i (I)^{1/2}} + bI \tag{61}$$

where I is the ionic strength of the solution; z_i and a_i are the electric charge and the ionic radius in solution of the i-th species, respectively; A and B are constants which depends on the temperature and dielectric constant of water, and b is a constant determined from experimental data (A, B and b were taken from tabulated values from Helgeson and Kirkham (1974). The value of the ionic strength is calculated as:

$$I = \frac{1}{2} \sum_{i=1}^{N_T} c_i z_i^2 \tag{62}$$

The activity of the water can be calculated according to the approximation of Garrels and Christ (1965):

$$a_{H_2O} = 1 - 0.018 \sum_{i=2}^{N_T} c_i \tag{63}$$

5.2 Description of the Febex in situ test reference case

The FEBEX in situ test was performed in a gallery excavated in granite in the underground research laboratory of Grimsel operated by NAGRA in Switzerland. The test included the heating system, the clay barrier and the instrumentation, monitoring and control system (*Figure 26*). The drift was 70.4 m long and 2.27 m in diameter. The test zone was located in the last 17.4 m of the drift where heaters, bentonite and instrumentation were installed. The main elements of the heating system were two heaters, separated horizontally by 1 m, which simulated full-sized canisters. The heaters were placed inside a cylindrical steel liner having a diameter of 0.93 m, which had been installed concentrically with the drift. Each heater was made of carbon steel, measured 4.54 m in length and 0.90 m in diameter, had a wall thickness of 0.10 m and weighed 11 tons. The heaters were designed to maintain a maximum temperature of 100ºC at the liner/bentonite interface. The bentonite barrier was made of blocks of highly compacted bentonite. The test began in February 1997. The 1st operation period lasted from 1997 to 2002 when heater 1 was switched off and the surrounding area was dismantled. The 2nd operation period started after the emplacement of a shotcrete plug and ended in June 2015 when the entire bentonite barrier was fully dismantled.

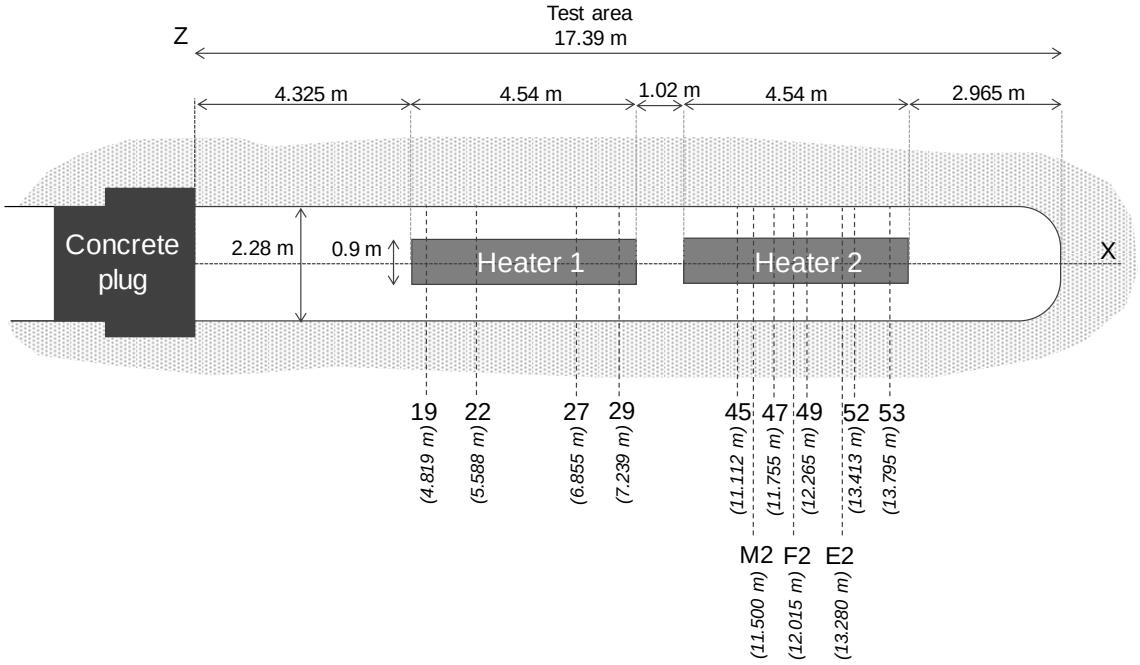

Figure 26.- General layout of the FEBEX in situ test indicating the instrumented and sampling sections used in this work. The x coordinates of the sections are referred to the concrete plug on the left.

The bentonite barrier is hydrated from the external cylindrical surface and water flows towards the internal heater/bentonite interface. The bentonite barrier is initially unsaturated, and it progressively hydrates from the surrounding rock towards the canister. The water content of the bentonite increases near the hydration boundary. Bentonite hydration leads to bentonite swelling. Therefore, the porosity of the bentonite increases during bentonite hydration. Mechanical and swelling processes play an important role in the hydrodynamic and geochemical evolution of the EBS during the early heating and hydration stage of the EBS, when bentonite buffer is subjected simultaneous to heating and hydration.

The temperature is fixed at 100ºC on the heater/bentonite interface. Water evaporates near the heater. Vapor diffuses away from the heater and condenses in cooler places. Vapor condensation retards the hydration of the bentonite buffer and affects the concentration of the dissolved species (Villar et al., 2012; Zheng et al., 2011).

The conditions of the FEBEX in situ test call for a coupled non-isothermal multiphase flow conceptual model with: 1) Advection of water in the liquid phase; 2) Advection and diffusion of vapor and other gases in the gaseous phase; 3) Advection and diffusion of air in the liquid and gaseous phases; 4) Convection of heat in the liquid and gaseous phase and; 5) Heat conduction.

5.3 Simplifications and benchmark test cases

The conceptual model for the multiphase simulations needs to be simplified due to the complexity of the real system. It has been agreed to consider a simplified system in the reference case and to increase the complexity of the modelled processes.

The proposed test cases (TC) are the following (*Table 6*):

1. Hydration and conservative tracer.
   - Bentonite hydration by fixing the liquid pressure at r = 1.14 m equal to 100 kPa
   - Constant temperature equal to 25ºC
   - Granite Cl^- concentration fix at r = 1.14 m

2. No hydration, conservative tracer and air and CO_2(g) diffusion.
   - Constant liquid saturation equal to 60% and constant gas saturation equal to 40%
   - Constant temperature equal to 25ºC
   - Granite Cl^- concentration fix at r = 1.14 m
   - CO_2(g) partial pressure equal to 0.1 bar fix at r = 1.14 m

3. No hydration, conservative tracer, CO_2(g) diffusion and calcite at equilibrium
   - Constant liquid saturation equal to 60% and constant gas saturation equal to 40%
   - Constant temperature equal to 25ºC
   - Granite Cl^- concentration fix at r = 1.14 m
   - CO_2(g) partial pressure equal to 0.1 bar fix at r = 1.14 m
   - Calcite precipitation at equilibrium

4. Hydration, conservative tracer, CO_2(g) diffusion and calcite at equilibrium.
   - Bentonite hydration by fixing the liquid pressure at r = 1.14 m equal to 100 kPa
   - Constant temperature equal to 25ºC
   - Granite Cl^- concentration fix at r = 1.14 m
   - CO_2(g) partial pressure equal to 0.1 bar fix at r = 1.14 m
   - Calcite precipitation at equilibrium

5. Hydration, conservative tracer, CO_2(g) diffusion and calcite and gypsum at equilibrium.
   - Bentonite hydration by fixing the liquid pressure at r = 1.14 m equal to 100 kPa
   - Constant temperature equal to 25ºC
   - Granite Cl^- concentration fix at r = 1.14 m
   - CO_2(g) partial pressure equal to 0.1 bar fix at r = 1.14 m
   - Calcite, gypsum and anhydrite precipitation/dissolution at equilibrium

6. Heating, hydration, evaporation and conservative tracer.
   - Bentonite hydration by fixing the liquid pressure at r = 1.14 m equal to 100 kPa
   - Temperature fix at r = 0.45 equal to 100ºC and equal to 25ºC at r = 1.14 m
   - Granite Cl^- concentration fix at r = 1.14 m
   - Vapour generation

7. Heating, hydration, evaporation, conservative tracer and CO_2(g) diffusion.
   - Bentonite hydration by fixing the liquid pressure at r = 1.14 m equal to 100 kPa
   - Temperature fix at r = 0.45 equal to 100ºC and equal to 25ºC at r = 1.14 m
   - Granite Cl^- concentration fix at r = 1.14 m
   - CO_2(g) partial pressure equal to 0.1 bar fix at r = 1.14 m
   - Vapour generation

8. Heating, hydration, evaporation, conservative tracer, CO_2(g) diffusion and minerals at equilibrium.
   - Bentonite hydration by fixing the liquid pressure at r = 1.14 m equal to 100 kPa
   - Temperature fix at r = 0.45 equal to 100ºC and equal to 25ºC at r = 1.14 m
   - Granite Cl^- concentration fix at r = 1.14 m
   - CO_2(g) partial pressure equal to 0.1 bar fix at r = 1.14 m
   - Calcite, gypsum and anhydrite precipitation/dissolution at equilibrium
   - Vapour generation

9. Heating, hydration, evaporation, conservative tracer, CO_2(g) diffusion, minerals at equilibrium and cation exchange.
   - Bentonite hydration by fixing the liquid pressure at r = 1.14 m equal to 100 kPa
   - Temperature fix at r = 0.45 equal to 100ºC and equal to 25ºC at r = 1.14 m
   - Granite Cl^- concentration fix at r = 1.14 m
   - CO_2(g) partial pressure equal to 0.1 bar fix at r = 1.14 m
   - Calcite, gypsum and anhydrite precipitation/dissolution at equilibrium
   - Vapour generation
   - Cation exchange reactions

10. Heating, hydration, evaporation, conservative tracer, CO_2(g) diffusion, minerals at equilibrium, cation exchange, corrosion, corrosion products and H_2(g) generation.
   - Bentonite hydration by fixing the liquid pressure at r = 1.14 m equal to 100 kPa
   - Temperature fix at r = 0.45 equal to 100ºC and equal to 25ºC at r = 1.14 m
   - Granite Cl^- concentration fix at r = 1.14 m
   - CO_2(g) partial pressure equal to 0.1 bar fix at r = 1.14 m
   - Calcite, gypsum and anhydrite precipitation/dissolution at equilibrium
   - Vapour generation
   - Cation exchange reactions
   - Corrosion, corrosion products and H_2(g) generation which is linked to corrosion rate and therefore is constrained by the steel corrosion rate

Table 6 - Proposed benchmark test cases for the Febex in situ test.

Test case	Heating	Hydration	Minerals	Gases	Cation exchange	Comment
TC1	No	Yes	-	Air	-	Tracer (Cl^-)
TC2	No	No	-	Air, $CO_2(g)$	-	Gas diffusion
TC3	No	No	Calcite*	Air, $CO_2(g)$	-	Gas diffusion & mineral diss/prec
TC4	No	Yes	Calcite*	Air, $CO_2(g)$	-	Hydration, gas diffusion & mineral diss/prec
TC5	No	Yes	Calcite*, gypsum*	Air, $CO_2(g)$	-	Hydration, gas diffusion & several minerals diss/prec
TC6	Yes	Yes	-	Air, vapour,	-	Nonisothermal water evaporation/condensation. Tracer (Cl^-)
TC7	Yes	Yes	-	Air, vapour, $CO_2(g)$	-	Nonisothermal water evaporation/condensation + $CO_2(g)$ + $CO_2(aq)$
TC8	Yes	Yes	calcite*, gypsum*, anhydrite*, quartz*	Air, vapour, $CO_2(g)$	-	Nonisothermal water evaporation/condensation + $CO_2(g)$ + $CO_2(aq)$ + minerals
TC9	Yes	Yes	calcite*, gypsum*, anhydrite*, quartz*	Air, vapour, $CO_2(g)$	Na^+, K^+, Ca^{2+}, Mg^{2+}	Nonisothermal water evaporation/condensation + $CO_2(g)$ + $CO_2(aq)$ + minerals+ cation exchange
TC10	Yes	Yes	calcite*, gypsum*, anhydrite*, quartz*, Fe(s)**, magnetite*, siderite*, goethite*,	Air, vapour, $CO_2(g)$, O2(g), $H_2(g)$	Na^+, K^+, Ca^{2+}, Mg^{2+}	Nonisothermal water evaporation/condensation + $CO_2(g)$ + $CO_2(aq)$ + minerals+ cation exchange + corrosion

**chemical equilibrium is considered. Temperature dependency of thermodynamic parameters is included. **under kinetic control*

Table 7 shows the resume of the boundary conditions at the inner and outer boundaries for test TC1 to TC6.

Table 7 – Resume of the boundary conditions of the test cases for the Febex in situ test.

Test cases	**Boundary r = 0.45 m**	**Boundary r = 1.14 m**
TC1	T = 25ºC	T = 25ºC P_{liq} = 100 kPa P_{gas} = 100 kPa Fix granite boundary water
TC2	T = 25ºC Fix S_{liq} = 60%	T = 25ºC P_{gas} = 100 kPa Fix S_{liq} = 60% Fix CO_2(g) pp = 0.1 bar
TC3	T = 25ºC Fix S_{liq} = 60%	T = 25ºC P_{gas} = 100 kPa Fix S_{liq} = 60% Fix granite boundary water Fix CO_2(g) pp = 0.1 bar
TC4	T = 25ºC	T = 25ºC P_{liq} = 100 kPa P_{gas} = 100 kPa Fix granite boundary water Fix CO_2(g) pp = 0.1 bar
TC5	T = 25ºC	T = 25ºC P_{liq} = 100 kPa P_{gas} = 100 kPa Fix granite boundary water Fix CO_2(g) pp = 0.1 bar
TC6	T = 100ºC	T = 25ºC P_{liq} = 100 kPa P_{gas} = 100 kPa Fix granite boundary water Fix CO_2(g) pp = 0.1 bar

5.4 Model description

5.4.1 Physical properties

Table 8 and *table 9* show the hydrodynamic and transport properties used in the numerical model of the Febex in situ test.

Table 8 - Thermal and hydrodynamic parameters of the bentonite (Samper et al., 2018; Zheng and Samper, 2008; Zheng et al., 2011)

Porosity, ∅	0.4
Intrinsic permeability for liquid flow, k_{il} (m²)	$k_{il} = k_o \frac{\phi^3}{(1-\phi)^2} \frac{(1-\phi_o)^2}{\phi_o^3}$ $k_o = 3.75\ 10^{-21}$ m²
Relative permeability to liquid, k_{rl}	$k_{rl} = S_l^3$
Van Genuchten retention curve, Ψ (kPa)	$S_l = S_r + \frac{S_s - S_r}{\left(1 + (\alpha(P_g - P_l)^{(\frac{1}{1-b})}\right)^b}$ $S_r = 0.05$ $S_s = 1$ $\alpha = 5 \cdot 10^{-5}$ kPa^{-1} $b = 0.21$
Liquid viscosity (kg/m s) (T in Celsius)	$661.2 \cdot 10^{-3}(T + 44)^{-1.562}$
Vapor tortuosity factor	0.10
Solid density (kg/m³) (T in Celsius)	$2780e^{(-2\cdot10^{-5}(T-12))}$
Liquid density (kg/m³) (T in Celsius)	$\rho^l = 998.2 \cdot \exp(5 \cdot 10^{-7}(P_l - 100) - 2.1 \cdot 10^{-4}(T - 12))$
Gas density (kg/m³) (T in Celsius)	$\rho_g = \rho_v + \rho_a$ $\rho_v = \frac{e^{(0.06374T - 0.1634\cdot10^{-3}T^2)}}{194.4} e^{-(2.16677\psi)/(\rho_l(T+273.15))}$ $\rho_a = \frac{3.499P_g}{T + 273.15} - 1.615\rho_v$
Specific heat of the solid (J/kg ºC)	835.5
Thermal conductivity of the solid (W/m ºC)	1.23
Intrinsic permeability for gas flow (m²)	$5 \cdot 10^{-10}$
Relative permeability to gas, k_{rg} (m²)	$k_{rg} = (1 - S_l)^3$

Gas viscosity (kg/m s)	$1.76 \cdot 10^{-5}$
Specific heat of the liquid (J/kg ºC)	4202
Specific heat of the air (J/kgº C)	1000
Specific heat of the vapor (J/kg ºC)	1620
Thermal conductivity of the liquid (W/m ºC)	1.5
Thermal conductivity of the air (W/m ºC)	$2.6 \cdot 10^{-2}$
Thermal conductivity of the vapor (W/m ºC)	$4.2 \cdot 10^{-2}$
Vaporization enthalpy (J/kg)	$2.45 \cdot 10^{6}$
Thermal compressibility of the water ($ºC^{-1}$)	$2.1 \cdot 10^{-4}$
Thermal compressibility of the solid ($ºC^{-1}$)	$2 \cdot 10^{-5}$

Table 9 - Hydrodynamic and transport parameters of the numerical models (Mon et al., 2017; Samper et al., 2018; Zheng and Samper, 2008; Zheng et al., 2011).

Molecular diffusion in water $D_0(T)$ in m²/s as a function of *T* and the molecular diffusion at the reference temperature T_{ref} (ºC), $D_0(T_{ref})$, with T_{ref} = 22ºC	$D_o(T) = D_o(T_{ref}) \frac{T}{T_0} \frac{\mu_0^l}{\mu^l}$ $D_o(T_{ref}) = 2 \cdot 10^{-11}$
Longitudinal dispersivity (m)	0.01
Molecular diameter of the gases species (m)	10^{-10}

5.4.2 Time and space discretization

A 1D row of rectangular elements was used (*Figure 27*). The model domain included the bentonite barrier, which extended from *r* = 0.45 m to *r* = 1.14 m. The spatial discretization is refined near the heater (0.45 m < *r* < 0.46 m) where the grid size is 1 mm. The length of the elements is 1 cm in the bentonite within the range 0.46 m < *r* < 1.14 m.

The simulation time horizon covered the entire duration of the in situ test from February 1997 to 2015 (18 years).

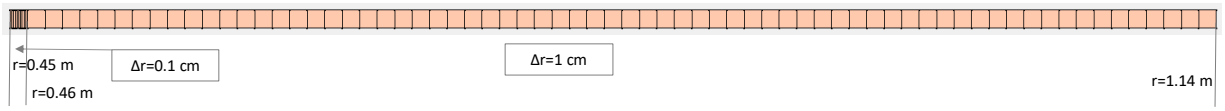

Figure 27.- Finite element mesh.

5.4.3 Thermodynamic database

The benchmark cases consider the thermodynamic database ThermoChimie version 11a (Giffaut et al., 2014), available in different formats at https://www.thermochimie-tdb.com/.

5.4.4 Geochemical properties

The primary species considered in the geochemical model of the benchmark case 1 are the following: H_2O, H^+, $O_2(aq)$, Na^+, Ka^+, Ca^{+2}, Mg^{+2}, Cl^-, SO_4^{-2}, CO_3^{2-} and $H_4SiO_4(aq)$. *Table 10* shows the chemical reactions and the equilibrium constants at 25ºC for the secondary aqueous species, minerals and gases used in the numerical model of the Febex in situ test benchmark case. The Fe aqueous species and minerals for the benchmark test case TC10 (with Fe^{+2} as primary species), in which the canister corrosion is considered, are the same than in the long-term corrosion benchmark case (see Table 14).

Table 10 - Chemical reactions and equilibrium constants for aqueous complexes, minerals and gases at 25ºC taken from the thermodynamic database ThermoChimie v11.a (Giffaut et al., 2014) to use in the model of the Febex in situ test benchmark case.

Aqueous complexes	**Log K**
$CaCO_3(aq) \Leftrightarrow Ca^{2+} + CO_3^{2-}$	-3.2200
$Ca(HCO_3)^+ \Leftrightarrow Ca^{2+} + H^+ + CO_3^{2-}$	-11.4300
$CaSO_4(aq) \Leftrightarrow Ca^{2+} + SO_4^{2-}$	-2.3100
$CaCl^+ \Leftrightarrow Ca^{2+} + Cl^-$	+0.2900
$CaCl_2(aq) \Leftrightarrow Ca^{2+} + 2Cl^-$	+0.6400
$Ca(H_3SiO_4)^+ + H^+ \Leftrightarrow Ca^{2+} + H_4SiO_4(aq)$	+8.8300
$CO_2(aq) + H_2O \Leftrightarrow 2H^+ + CO_3^{2-}$	-16.6800
$HCO_3^- \Leftrightarrow H^+ + CO_3^{2-}$	-10.3300
$H_2(aq) + 0.5O_2(aq) \Leftrightarrow H_2O$	+46.0700
$H_3(SiO_4)^- + H^+ \Leftrightarrow H_4SiO_4(aq)$	+9.8400
$KCl(aq) \Leftrightarrow K^+ + Cl^-$	+0.5000
$KSO_4^- \Leftrightarrow K^+ + SO_4^{2-}$	-0.8800
$MgCO_3(aq) \Leftrightarrow Mg^{2+} + CO_3^{2-}$	-2.9800
$Mg(HCO_3)^+ \Leftrightarrow Mg^{2+} + H^+ + CO_3^{2-}$	-11.3700
$MgSO_4(aq) \Leftrightarrow Mg^{2+} + SO_4^{2-}$	-2.2300
$MgCl^+ \Leftrightarrow Mg^{2+} + Cl^-$	-0.3500
$Mg(H_3SiO_4)^+ + H^+ \Leftrightarrow Mg^{2+} + H_4SiO_4(aq)$	+8.5800
$NaHCO_3(aq) \Leftrightarrow Na^+ + H^+ + CO_3^{2-}$	-10.0800
$NaSO_4^- \Leftrightarrow Na^+ + SO_4^{2-}$	-0.9400
$NaCl(aq) \Leftrightarrow Na^+ + Cl^-$	+0.5000
$Na(CO_3)^- \Leftrightarrow Na^+ + CO_3^{2-}$	-1.2700
$OH^- + H^+ \Leftrightarrow H_2O$	14.000
Minerals	**LogK**
Calcite $\Leftrightarrow Ca^{2+} + CO_3^{2-}$	-8.4800
Anhydrite $\Leftrightarrow Ca^{2+} + SO_4^{2-}$	-4.4400
Gypsum $\Leftrightarrow Ca^{2+} + SO_4^{2-} + 2H_2O$	-4.6100
Quartz $+ 2H_2O \Leftrightarrow H_4SiO_4(aq)$	-3.7400
Gases	**LogK**
$CO_2(g) + H_2O \Leftrightarrow 2H^+ + CO_3^{2-}$	-18.1500
$H_2(g) + 0.5O_2(aq) \Leftrightarrow H_2O$	+42.9900
$O_2(g) \Leftrightarrow O_2(aq)$	-2.9000

5.4.5 Initial conditions

Bentonite had an initial porosity of 0.40, a volumetric water content of 24%, which corresponds to a gravimetric water content of around 14.4%, a liquid saturation degree of 60% and a suction of $1.17 \cdot 10^5$ kPa. The gas pressure was set to 100 kPa. The initial temperature was uniform and equal to 25ºC. The initial compositions of the bentonite and the granite pore water, the initial mineral volume fractions and the initial concentrations of exchanged ions are listed in *Table 11*. *Table 12* shows the selectivity constants for the cation exchange reactions in the bentonite.

Table 11 - Initial pore water composition (Fernández et al., 2001; Samper et al., 2008a), initial mineral volume fractions (Samper et al., 2008a) and initial concentrations of exchanged ions (Fernández et al., 2004) in the bentonite and granite used in the model of the Febex in situ test benchmark case.

	Bentonite	**Granite**
pH	7.72	8.35
O_2(aq)	$3.06 \cdot 10^{-4}$	$1.63 \cdot 10^{-75}$
Na^+ (mol/L)	$1.3 \cdot 10^{-1}$	$3.8 \cdot 10^{-4}$
K^+ (mol/L)	$1.7 \cdot 10^{-3}$	$7.8 \cdot 10^{-6}$
Ca^{2+} (mol/L)	$2.2 \cdot 10^{-2}$	$1.8 \cdot 10^{-4}$
Mg^{2+} (mol/L)	$2.3 \cdot 10^{-2}$	$1.3 \cdot 10^{-6}$
CO_3^{2-} (mol/L)	$4.1 \cdot 10^{-4}$	$3.9 \cdot 10^{-4}$
SO_4^{2-} (mol/L)	$3.2 \cdot 10^{-2}$	$7.9 \cdot 10^{-5}$
Cl^- (mol/L)	$1.6 \cdot 10^{-1}$	$1.3 \cdot 10^{-5}$
H_4SiO_4(aq) (mol/L)	$1.1 \cdot 10^{-4}$	$1.4 \cdot 10^{-4}$
Calcite (fraction volume)	1	-
Quartz (fraction volume)	4.5	-
Anhydrite (fraction volume)	0	-
Gypsum (fraction volume)	0.016	-
Exchanged Na^+ (meq/100g)	21.10	-
Exchanged K^+ (meq/100g)	1.94	-
Exchanged Ca^{2+} (meq/100g)	31.31	-
Exchanged Mg^{2+} (meq/100g)	41.41	-
CEC (meq/100g)	95.76	-

Table 12 - Selectivity constants for cation exchange reactions in the FEBEX bentonite (ENRESA, 2006).

Cation exchange	**$K_{Na\text{-}cation}$**
$Na^+ + X\text{-}K \Leftrightarrow K^+ + X\text{-}Na$	0.138
$Na^+ + 0.5\ X_2\text{-}Ca \Leftrightarrow 0.5\ Ca^{2+} + X\text{-}Na$	0.294
$Na^+ + 0.5\ X_2\text{-}Mg \Leftrightarrow 0.5\ Mg^{2+} + X\text{-}Na$	0.288

5.4.6 Boundary conditions

The temperature and the liquid and gas pressure at the outer boundary (r = 1.135 m) were equal to 25ºC and 100 kPa, respectively. A constant temperature of 100ºC was prescribed at the internal boundary which coincides with the liner/bentonite interface (r = 0.45 m). There was no gas and liquid flow at r = 0.45 m.

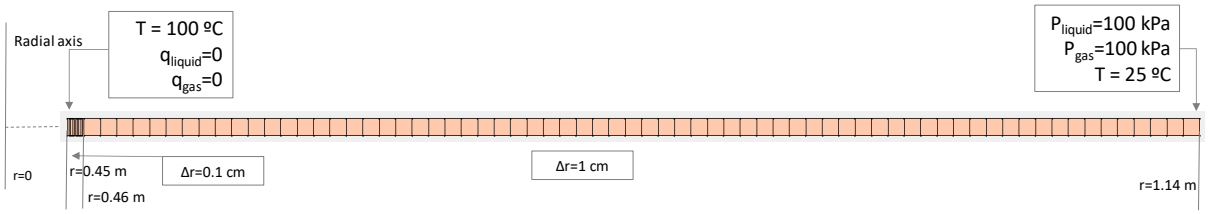

Figure 28.- Boundary conditions.

5.4.7 Canister corrosion

Anaerobic canister corrosion is considered in the benchmark test case TC5. The canister is treated as a porous material made of 100% metallic iron, Fe(s). Under anaerobic conditions, H_2O is the oxidizing agent of Fe(s) (Lu et al., 2011; Mon, 2017; Samper et al., 2016). The anaerobic Fe(s) corrosion reaction is given by:

$$Fe(s) + 2H_2O \rightleftarrows Fe^{2+} + 2OH^- + H_2(g) \quad (61)$$

By rewriting this reaction in terms of the primary species used in the numerical model, one obtains:

$$Fe(s) + 2H^+ + 0.5O_2(aq) \rightleftarrows Fe^{2+} + H_2O \quad (62)$$

The carbon-steel corrosion is kinetically controlled and assumed to corrode at a constant rate of 2 μm/year (it should be noticed that η = 0 for constant canister corrosion), which amounts to 0.281 mol/m^2/year.

5.5 Calculated model results

An excel file of each benchmark test case will be distributed to compare the computed results including the time evolution at selected locations and the spatial distribution at selected times of:

- The computed liquid and gas saturation
- The computed total dissolved chemical species concentration and pH
- The computed concentration of precipitated and dissolved minerals
- The computed gases concentration
- The computed cation exchange concentration

5.5.1 Case TC1. Hydration and conservative tracer.

Figure 29, *figure 30*, *figure 31* and *figure 32* show some preliminary benchmarking? results for water content and Cl- concentration for Case TC1.

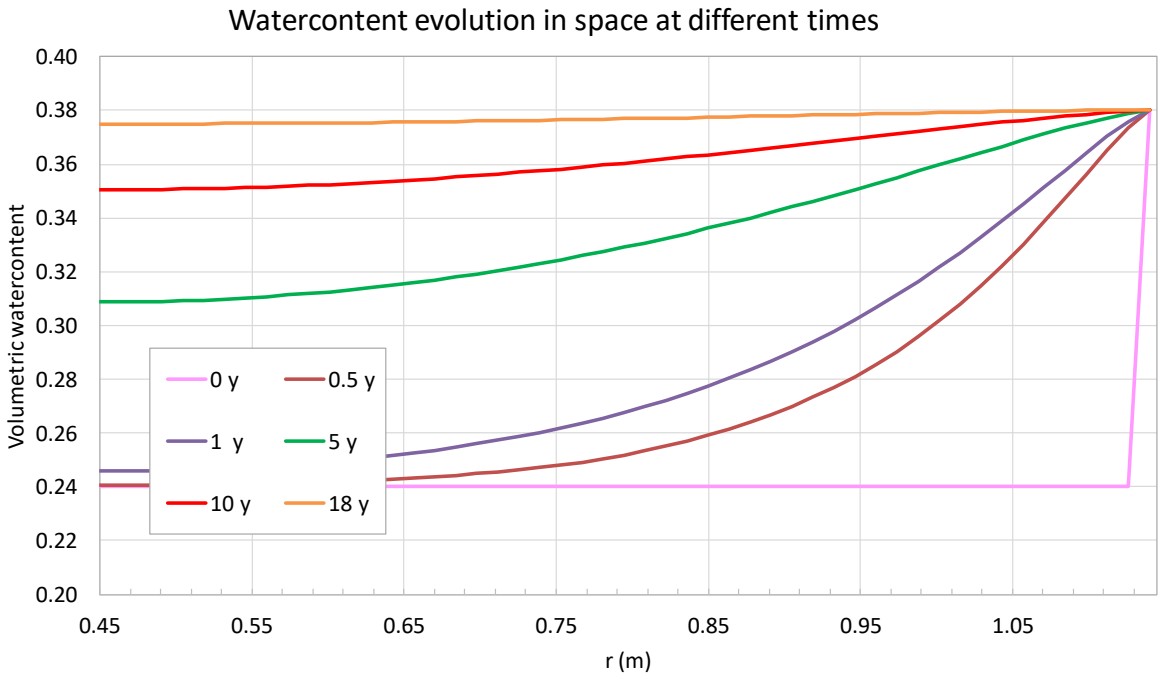

Figure 29.- Spatial distribution of the computed watercontent at 0, 0.5, 1, 5, 10 and 18 years for the Case TC1.

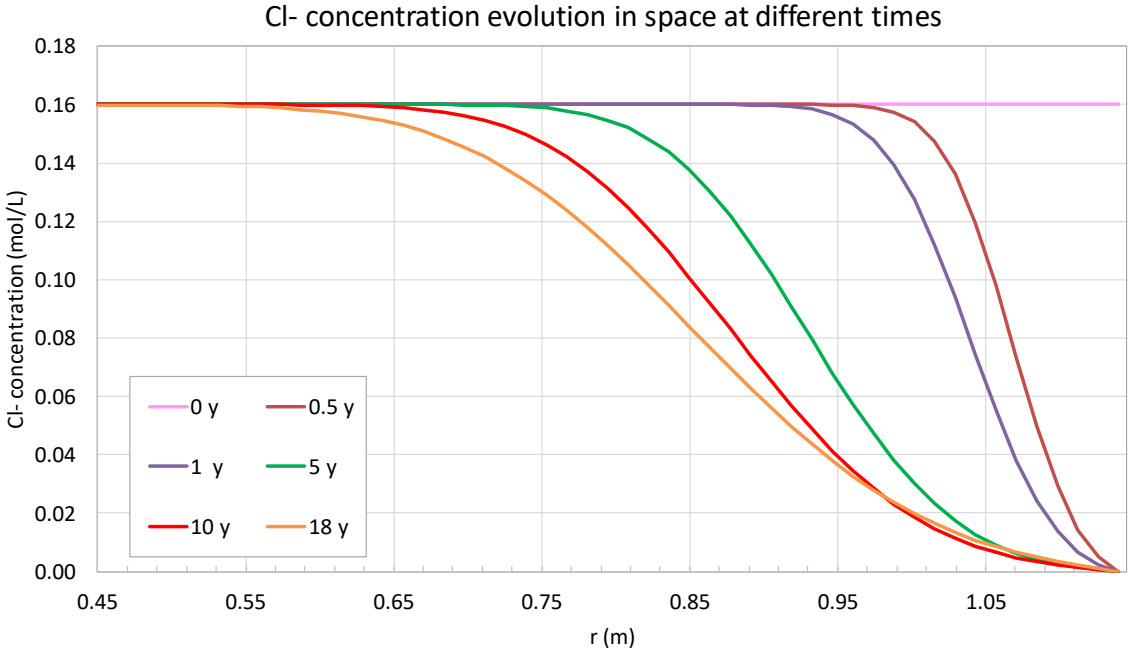

Figure 30.- Spatial distribution of the computed Cl^- concentration at 0, 0.5, 1, 5, 10 and 18 years for the Case TC1.

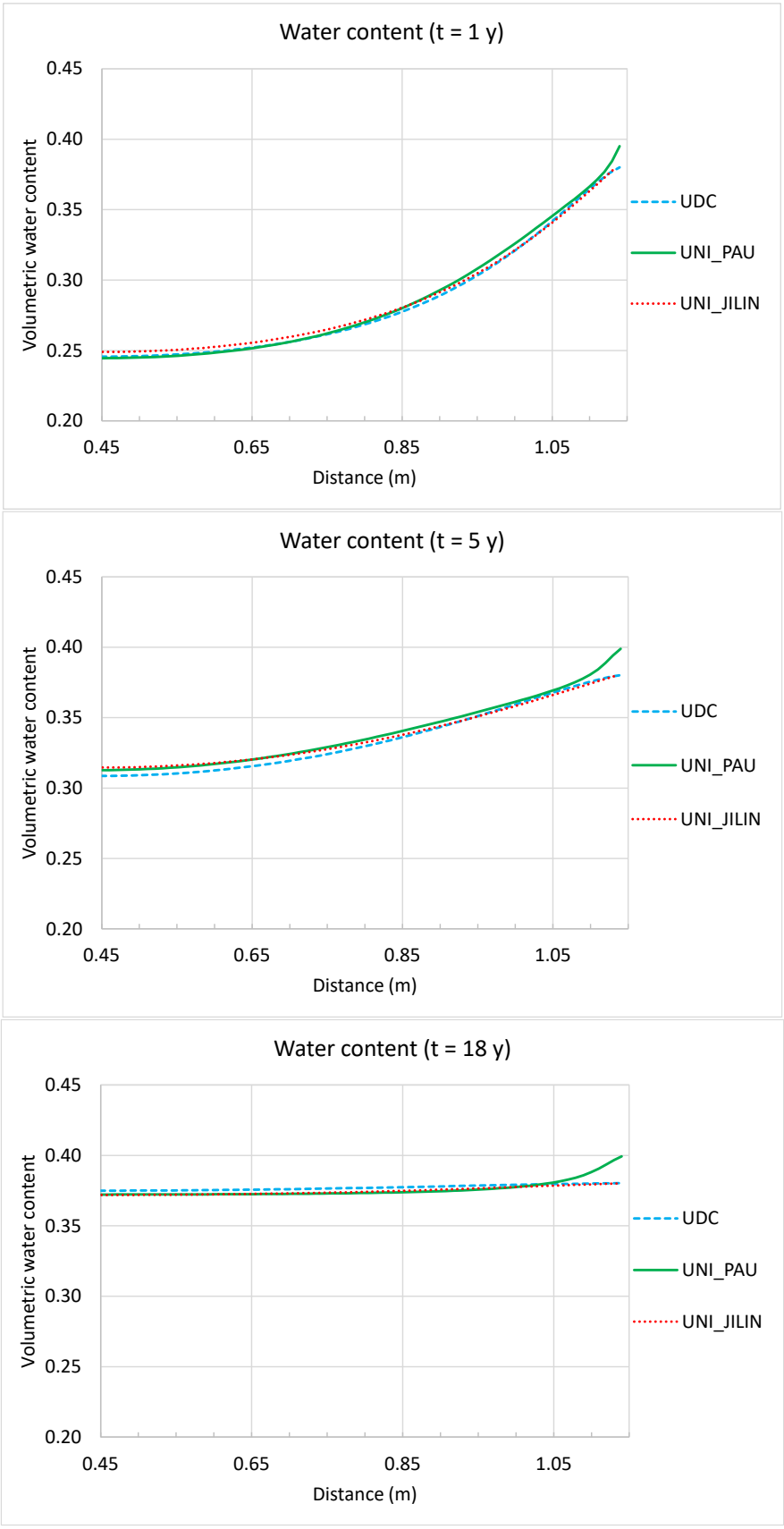

Figure 31.- Comparison of the spatial distribution of the computed water content at 1, 5 and 18 years for the Case TC1.

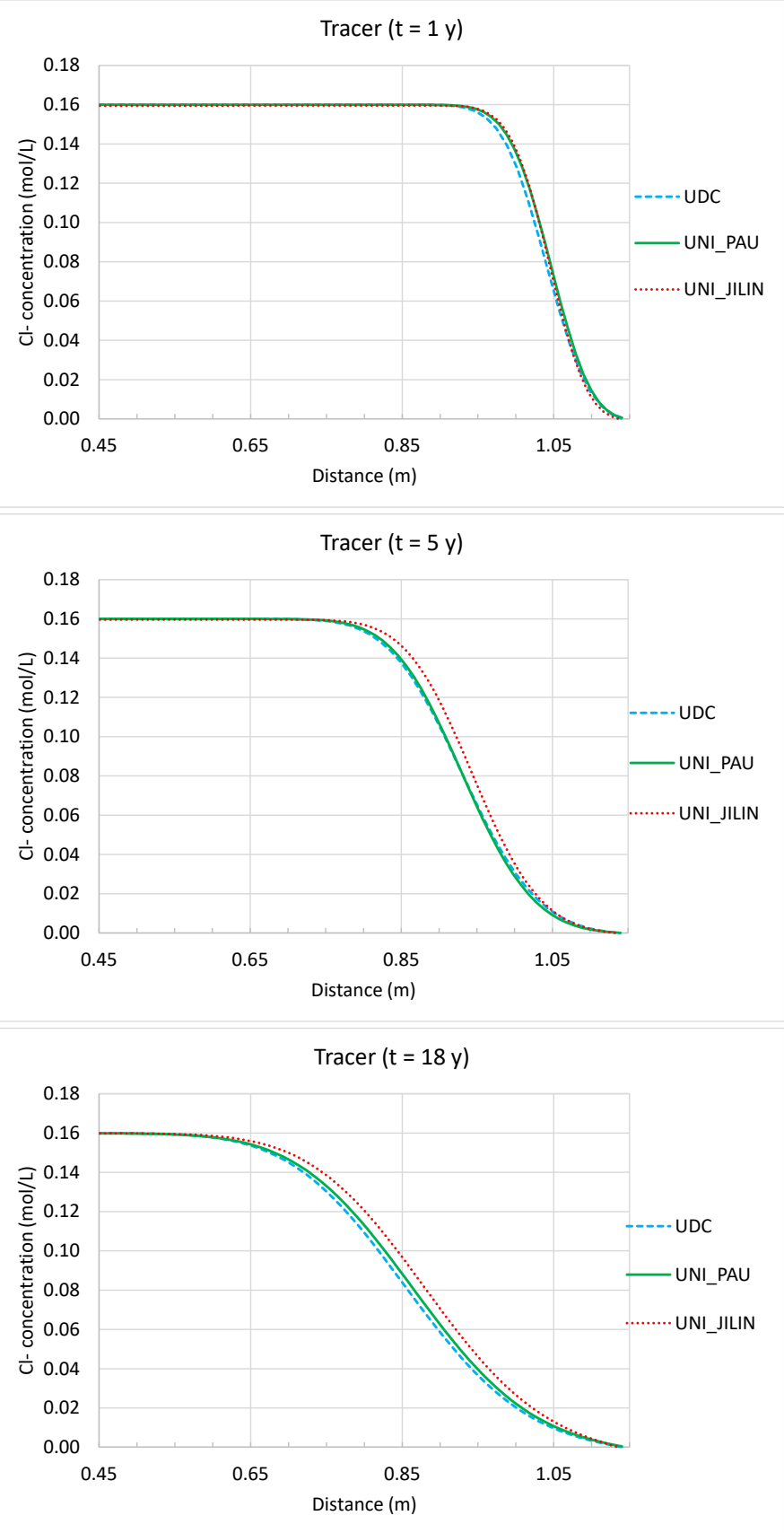

Figure 32.- Comparison of the spatial distribution of the computed Cl^- concentration at 1, 5 and 18 years for the Case TC1.

5.5.2 Case TC2. Gas diffusion

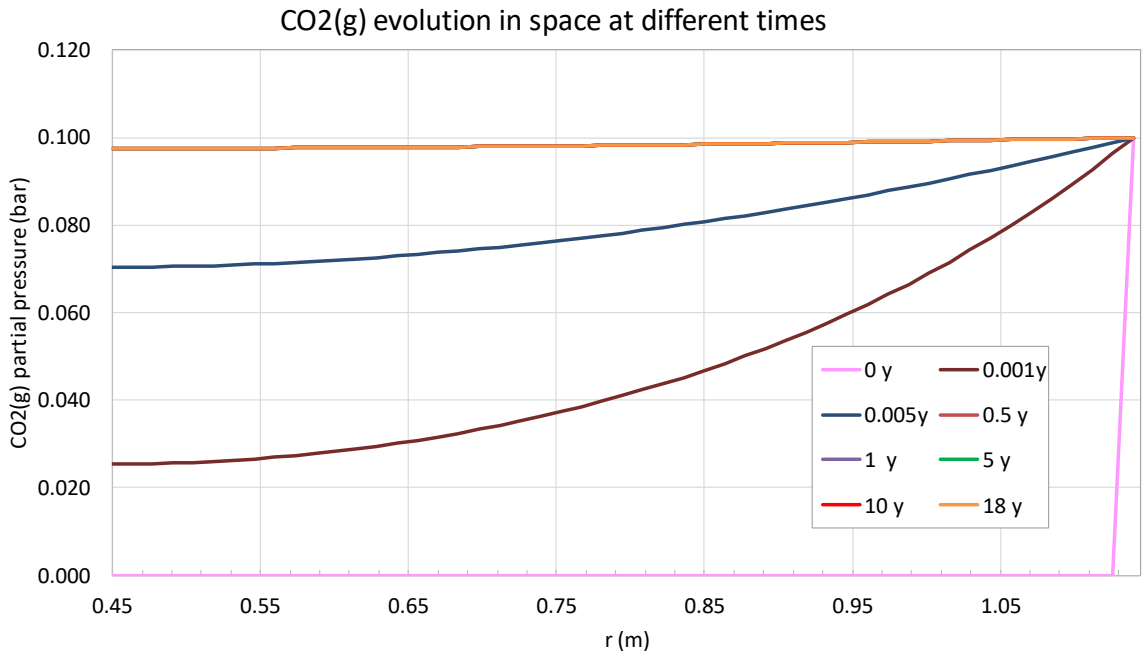

Figure 33.- Spatial distribution of the computed CO_2(g) partial pressure at 0, 0.5, 1, 5, 10 and 18 years for the Case TC2.

5.5.3 Case TC3. Gas diffusion & mineral diss/prec

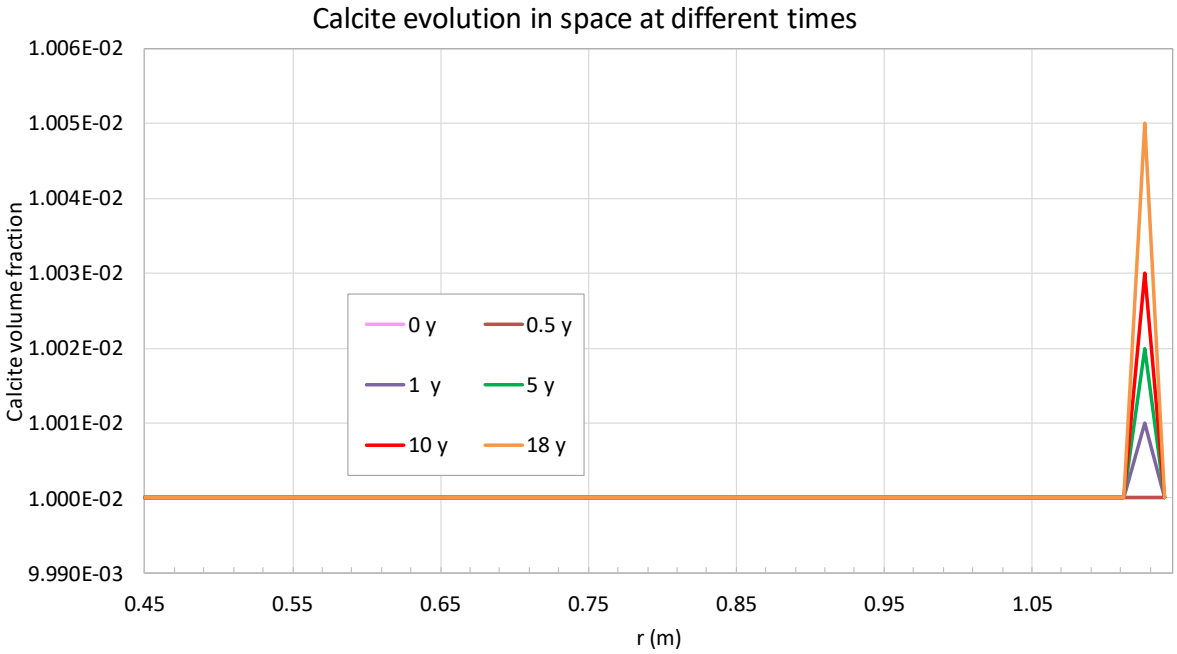

Figure 34.- Spatial distribution of the computed cumulative calcite precipitation at 0, 0.5, 1, 5, 10 and 18 years for the Case TC3.

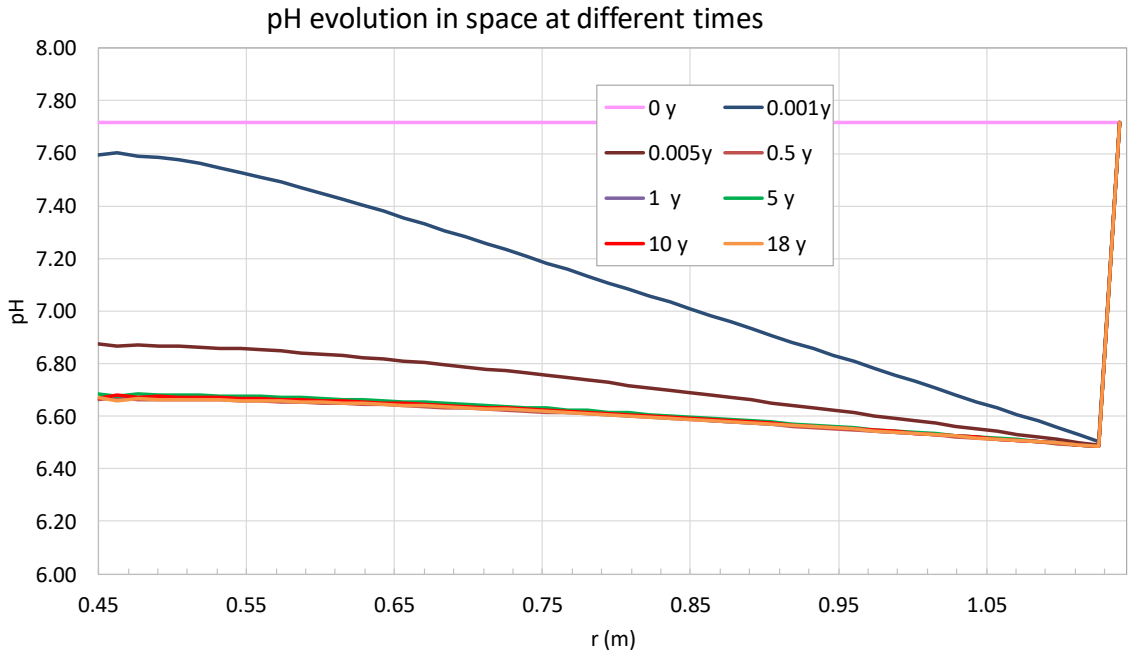

Figure 35.- Spatial distribution of the computed pH at 0, 0.001, 0.005, 0.5, 1, 5, 10 and 18 years for the Case TC3.

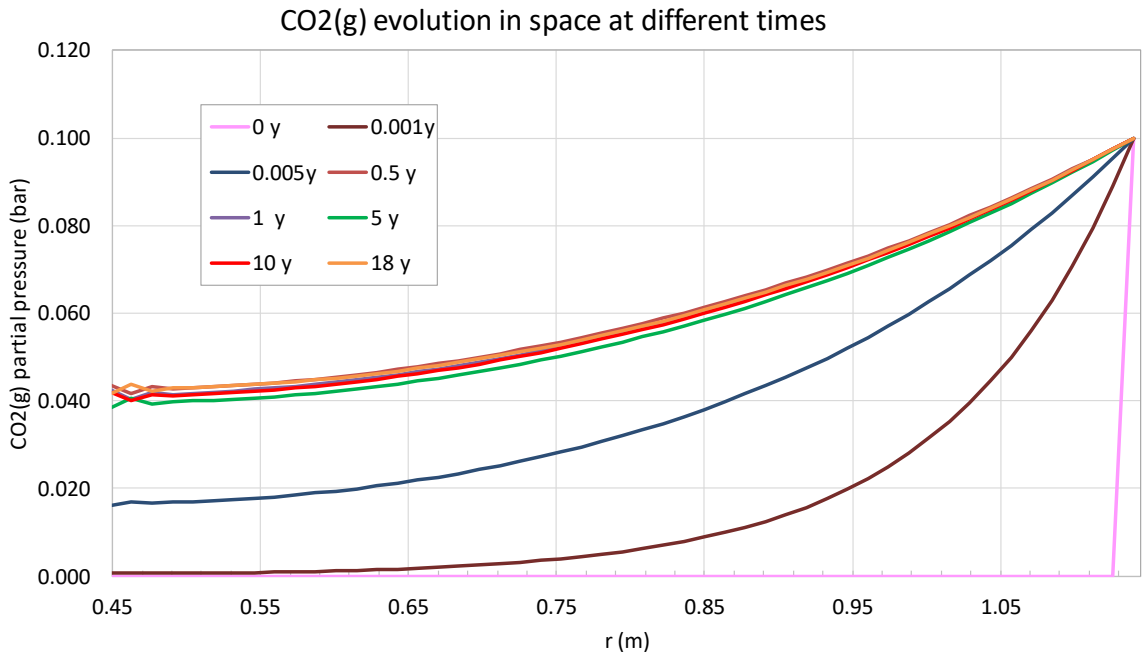

Figure 36.- Spatial distribution of the computed CO_2(g) partial pressure at 0, 0.001, 0.005, 0.5, 1, 5, 10 and 18 years for the Case TC3.

5.5.4 Case TC4. Hydration, conservative tracer, CO2(g) diffusion and calcite and gypsum at equilibrium.

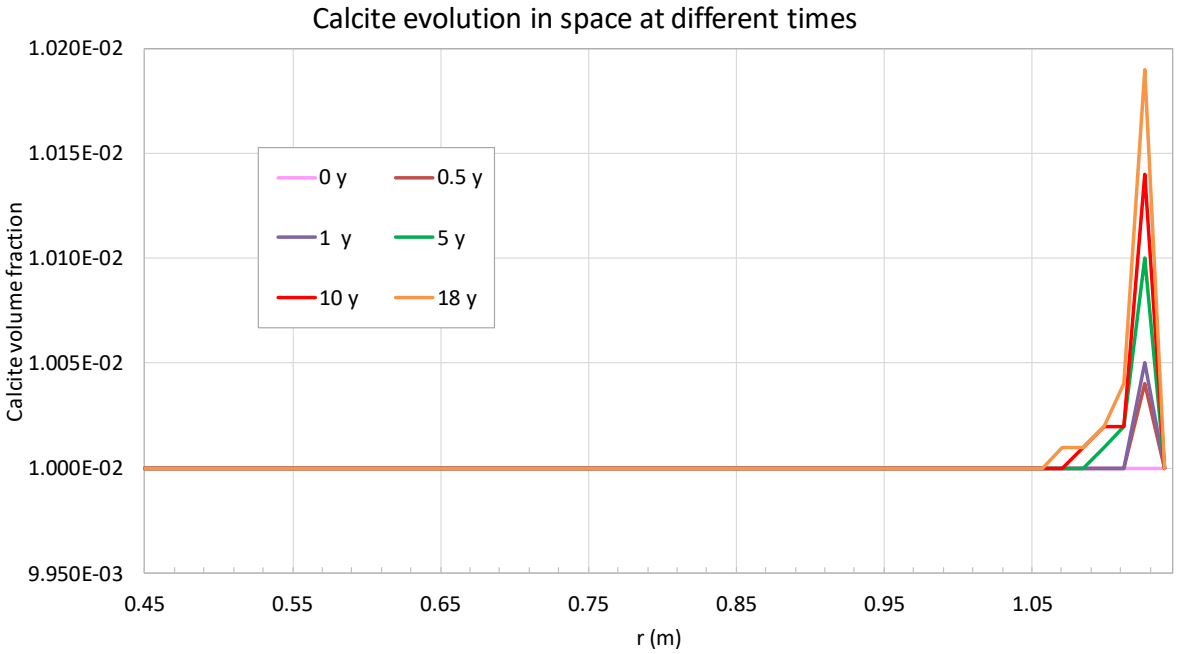

Figure 37.- Spatial distribution of the computed calcite volume fraction at 0, 0.5, 1, 5, 10 and 18 years for the Case TC4.

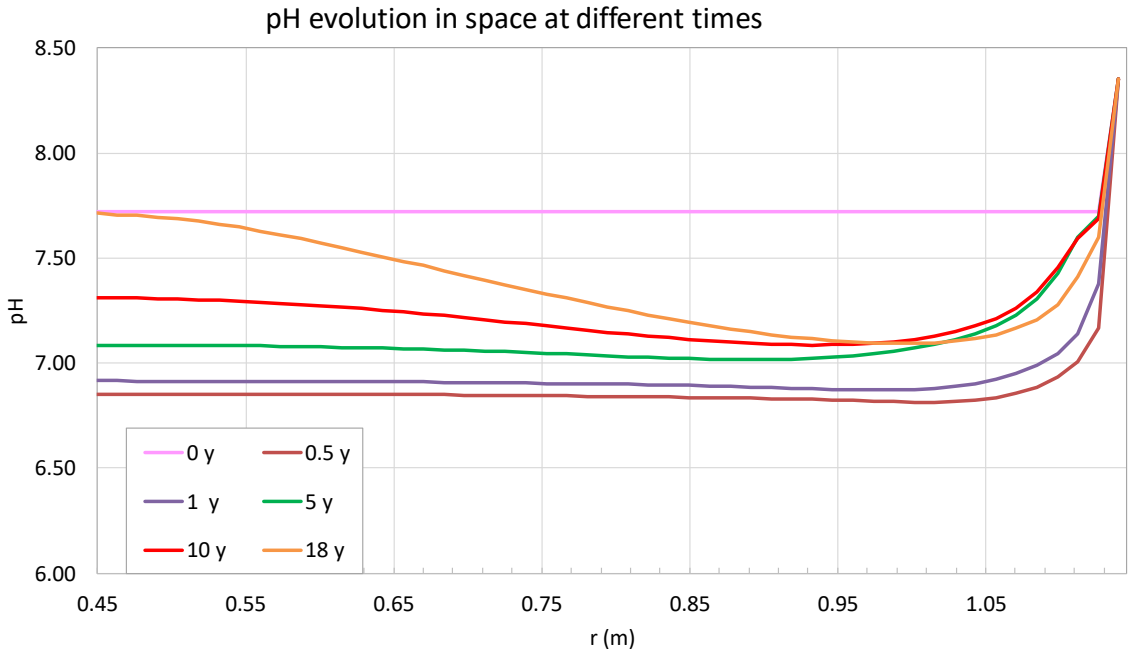

Figure 38.- Spatial distribution of the computed pH at 0, 0.5, 1, 5, 10 and 18 years for the Case TC4.

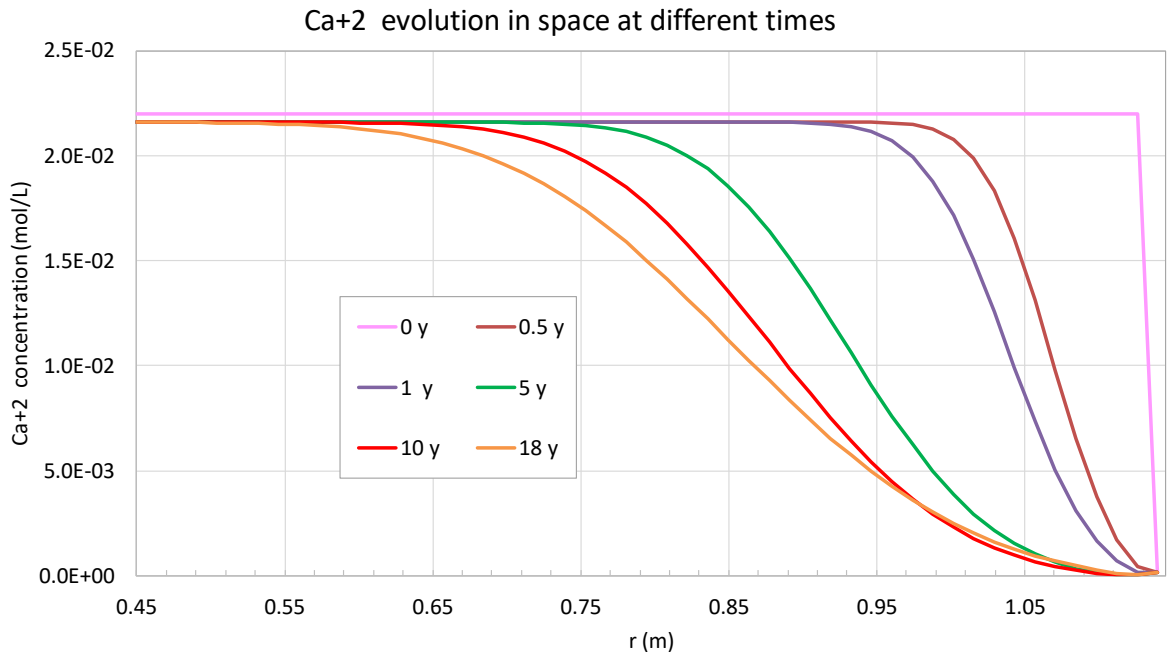

Figure 39.- Spatial distribution of the computed Ca^{2+} concentration at 0, 0.5, 1, 5, 10 and 18 years for the Case TC4.

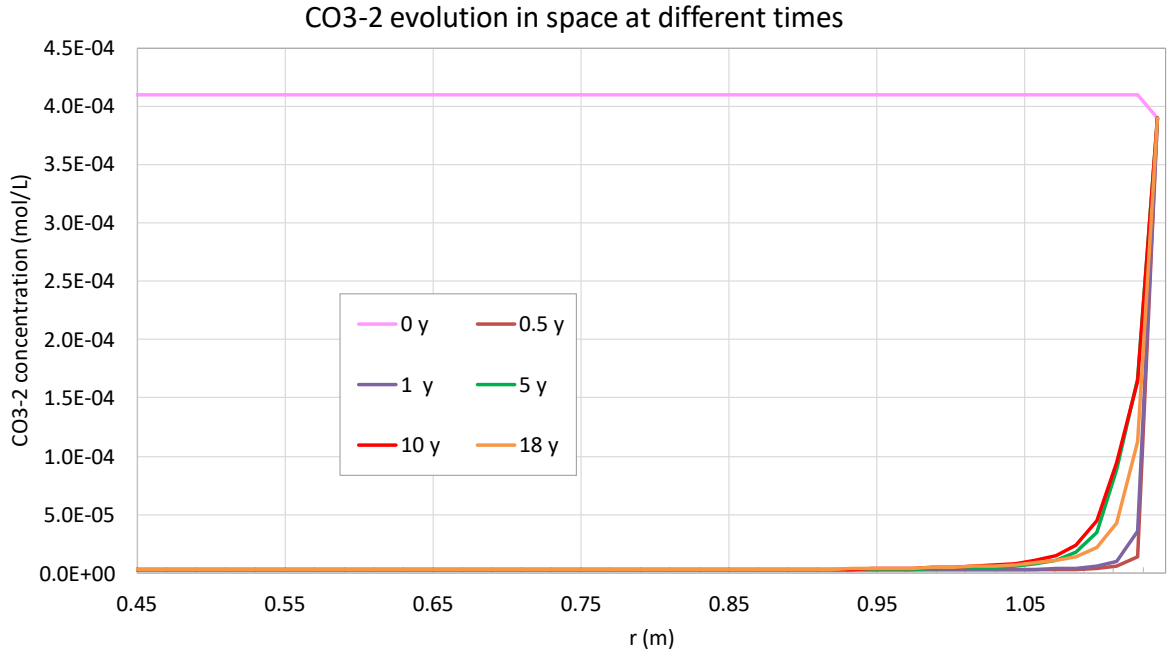

Figure 40.- Spatial distribution of the computed CO_3^{2-} concentration at 0, 0.5, 1, 5, 10 and 18 years for the Case TC4.

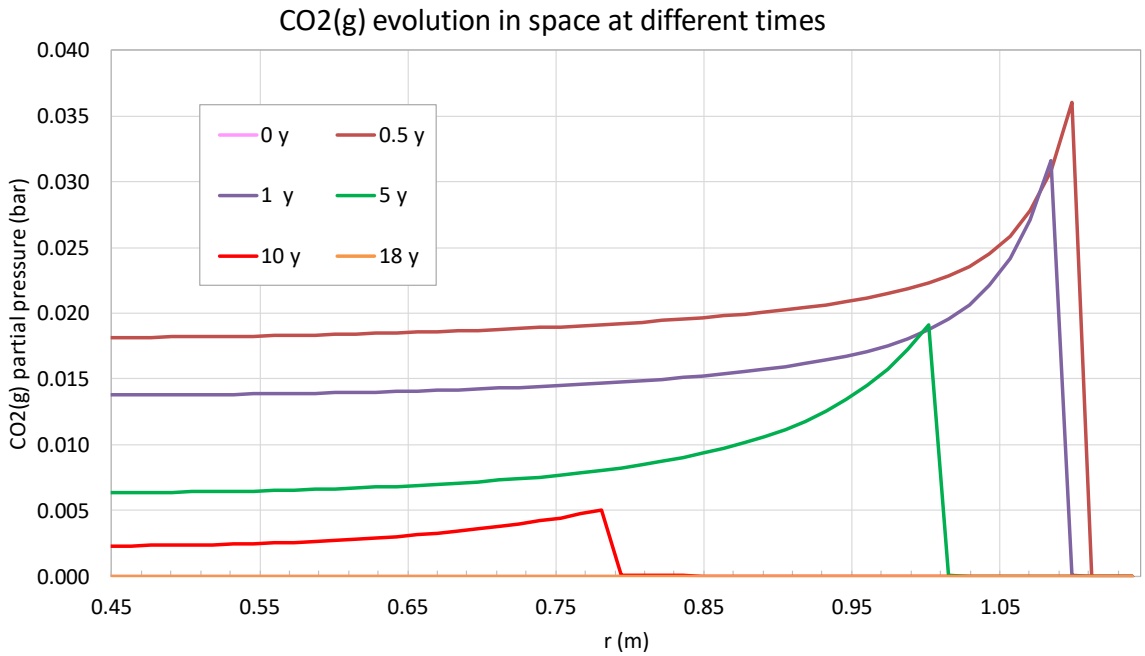

Figure 41.- Spatial distribution of the computed $CO_2(g)$ partial pressure at 0, 0.5, 1, 5, 10 and 18 years for the Case TC4.

5.5.5 Case TC5. Hydration, conservative tracer, CO2(g) diffusion and calcite and gypsum at equilibrium.

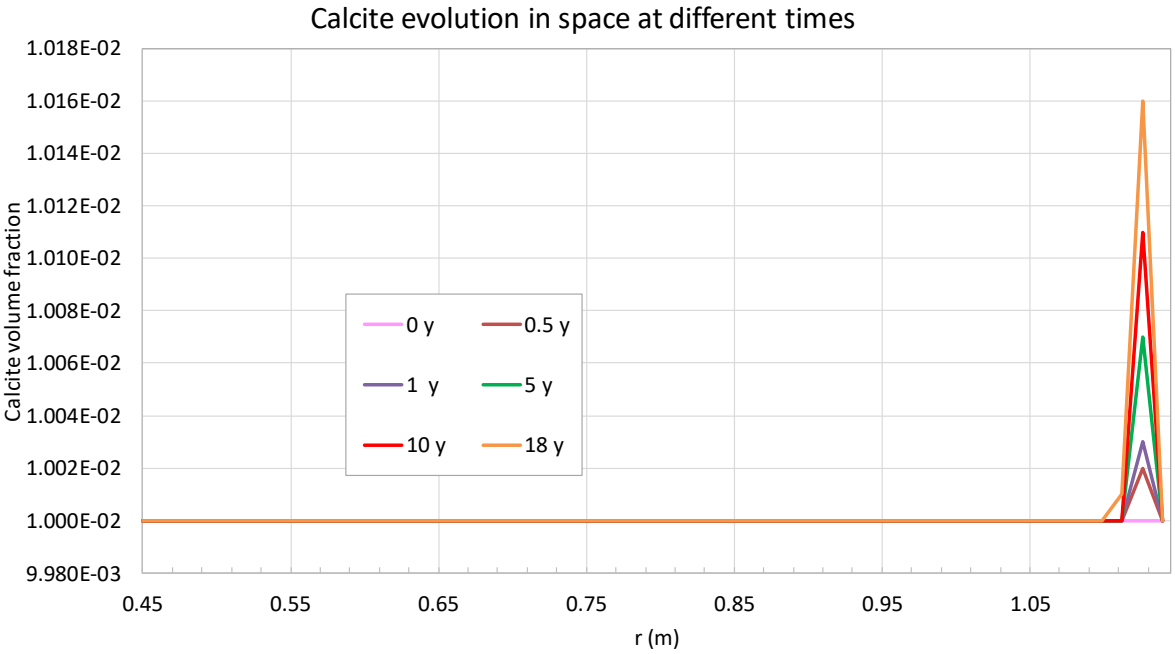

Figure 42.- Spatial distribution of the computed calcite volume fraction at 0, 0.5, 1, 5, 10 and 18 years for the Case TC5.

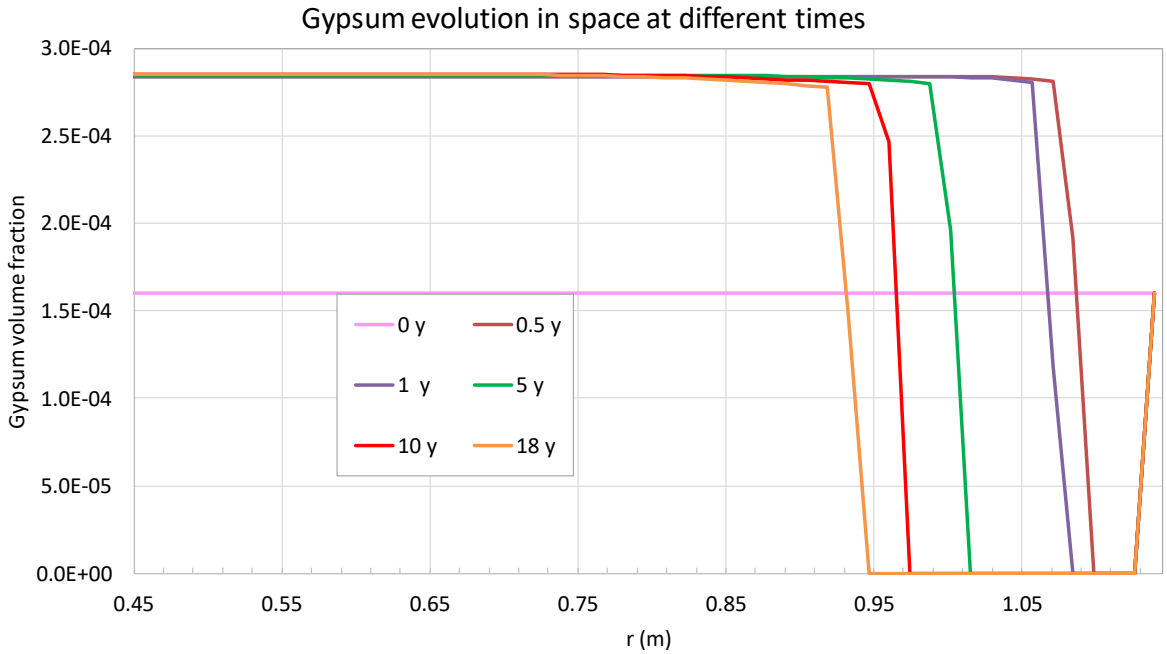

Figure 43.- Spatial distribution of the computed gypsum volume fraction at 0, 0.5, 1, 5, 10 and 18 years for the Case TC5.

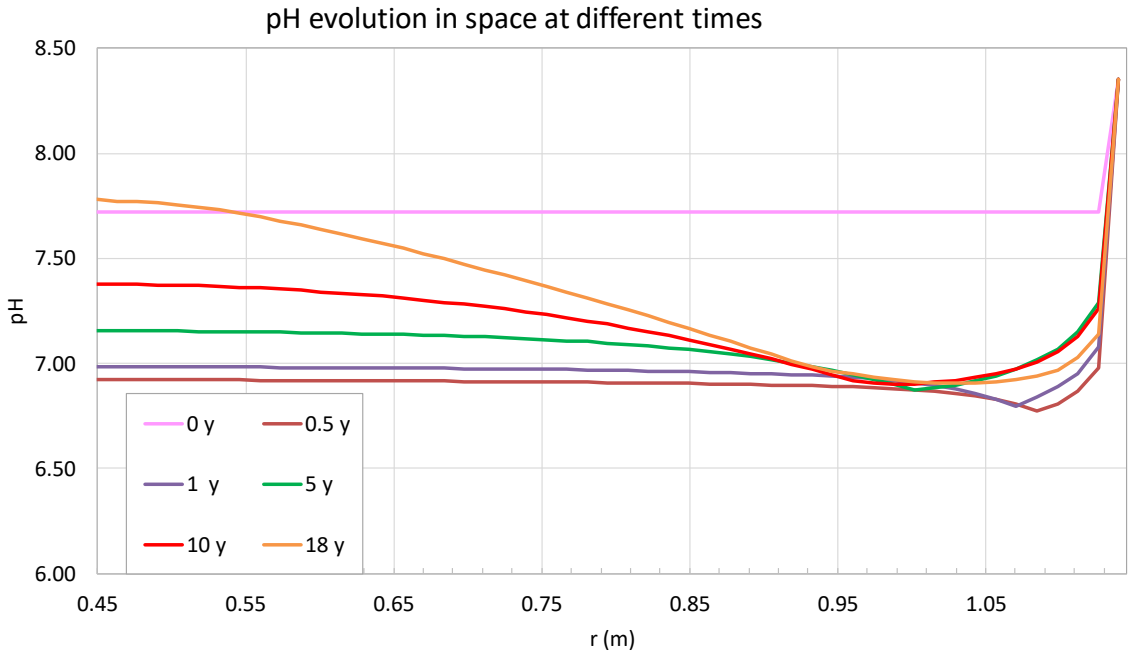

Figure 44.- Spatial distribution of the computed pH at 0, 0.5, 1, 5, 10 and 18 years for the Case TC5.

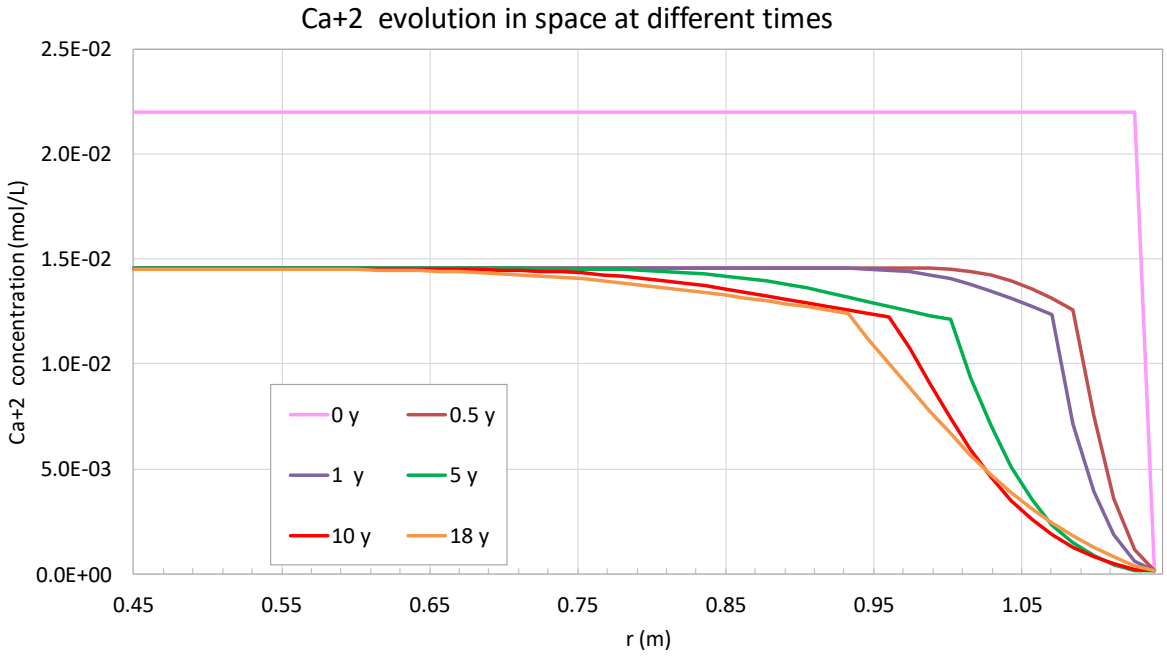

Figure 45.- Spatial distribution of the computed Ca^{2+} concentration at 0, 0.5, 1, 5, 10 and 18 years for the Case TC5.

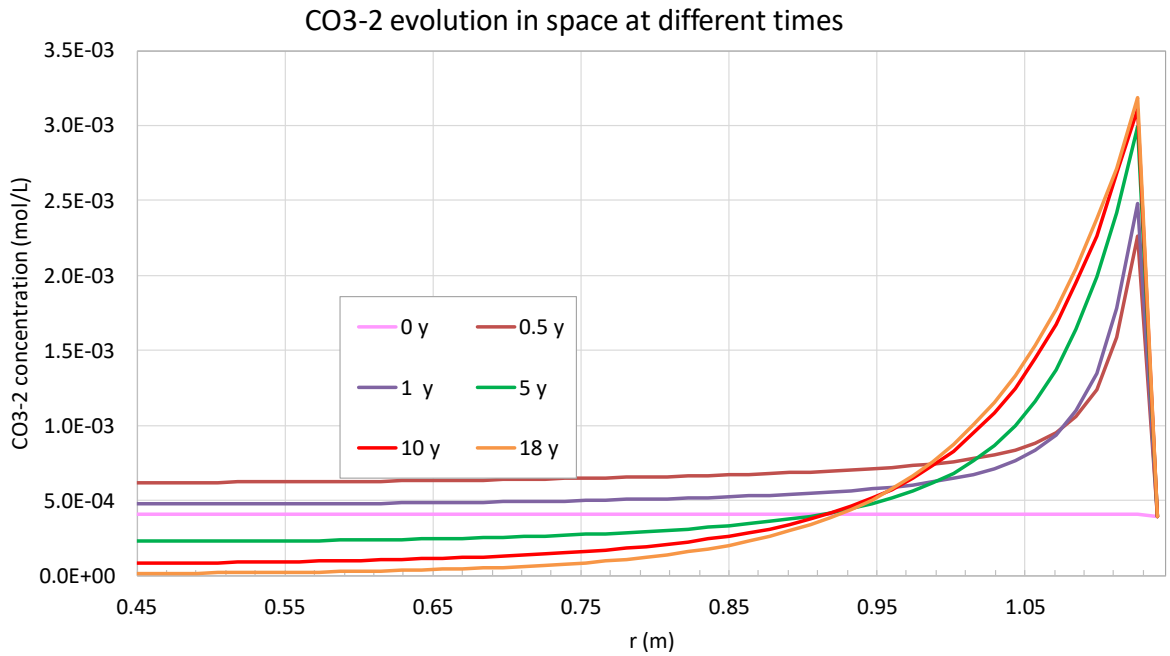

Figure 46.- Spatial distribution of the computed CO_3^{2-} concentration at 0, 0.5, 1, 5, 10 and 18 years for the Case TC5.

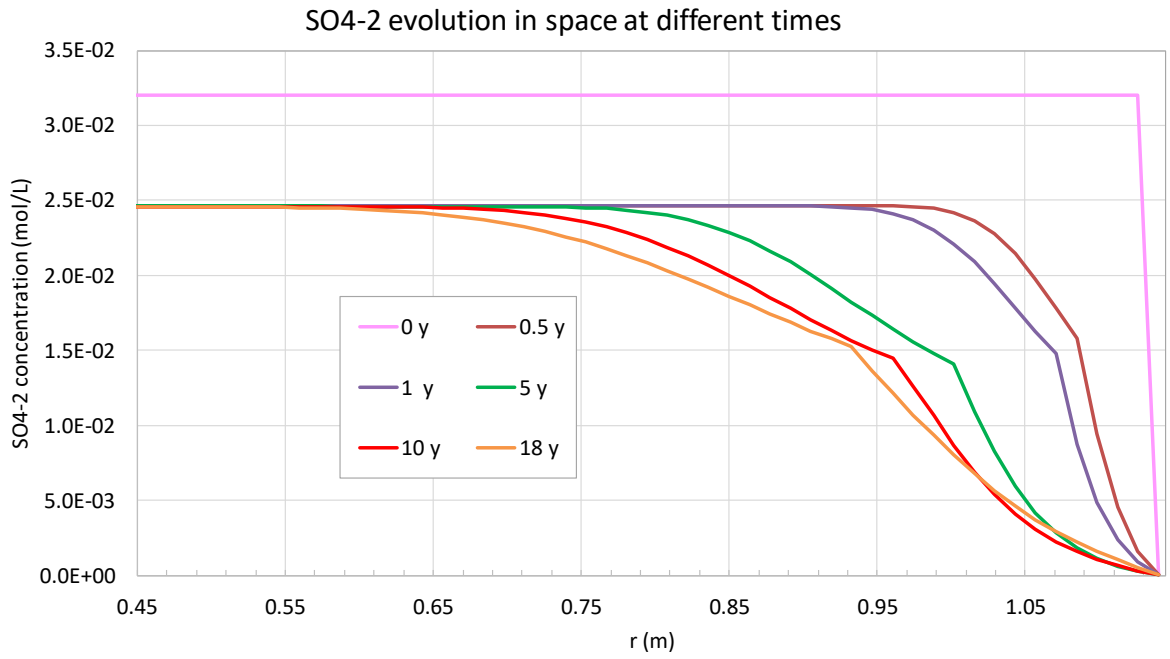

Figure 47.- Spatial distribution of the computed SO_4^{2-} concentration at 0, 0.5, 1, 5, 10 and 18 years for the Case TC5.

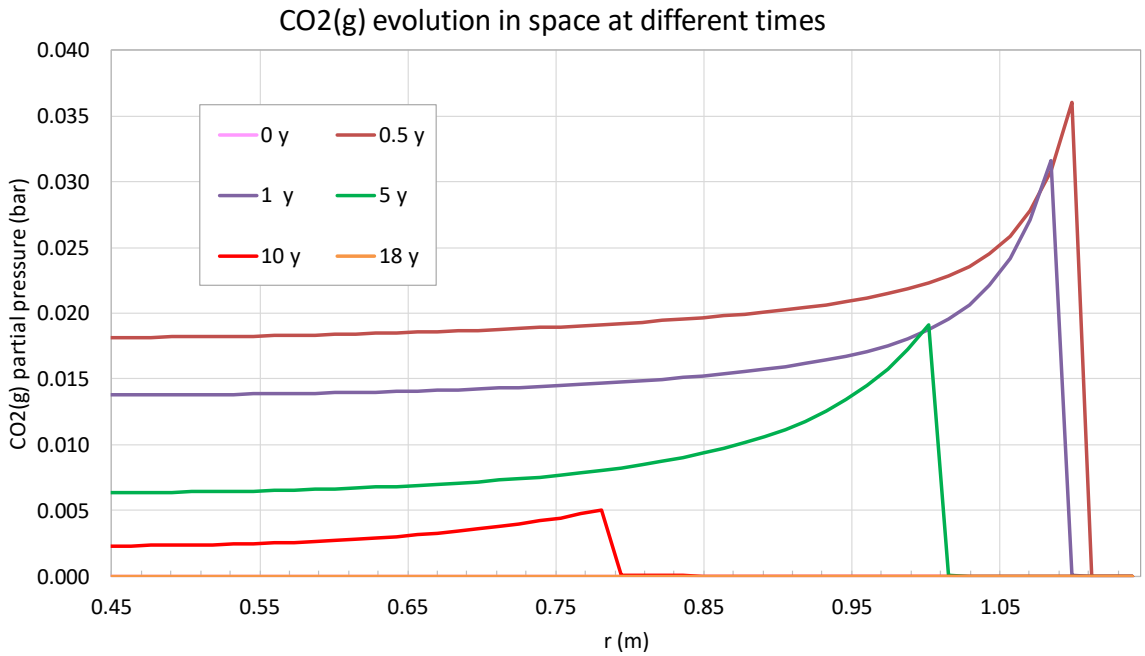

Figure 48.- Spatial distribution of the computed $CO_2(g)$ partial pressure at 0, 0.5, 1, 5, 10 and 18 years for the Case TC5.

6. Benchmark case 2: Long-term corrosion

6.1 Description of the long-term corrosion benchmark case

Samper et al. (2016) presented a non-isothermal multicomponent reactive transport model to study the long-term interactions of corrosion products and compacted bentonite in a high-level radioactive waste (HLW) repository in granite based on the Spanish reference concept (ENRESA, 2000). It consists on the disposal of spent fuel elements in cylindrical carbon steel canisters surrounded by blocks of compacted bentonite placed in horizontal disposal drifts, which are located at a depth of 500 m in a granite formation.

6.2 Simplifications and benchmark test cases

The conceptual model for the non-isothermal multicomponent reactive transport model to study the long-term interactions of corrosion products and compacted bentonite in a HLW repository in granite needs to be simplified due to the complexity of the real system. It has been agreed to consider a simplified system in the reference case and to increase the complexity of the modelled processes.

One simplification is that the granite host rock is considered as a boundary condition and not as a material of the model. Bentonite swelling process is not considered. Surface complexation by sorption is not taken into account in the model.

The proposed benchmark test cases (TC) are the following (Table 13):

1. Conservative transport.
2. Conservative transport. Aqueous complexation, canister corrosion and H2(g) generation.
3. Conservative transport. Aqueous complexation, canister corrosion, H2(g) generation, bentonite minerals and corrosion products.
4. Conservative transport. Aqueous complexation, canister corrosion, H2(g) generation, bentonite minerals and corrosion products and cation exchange.
5. Adding the porosity feedback effect (PFE).

Table 13 - Proposed benchmark test cases of the non-isothermal multiphase and reactive transport for radioactive waste disposal (benchmark case 2 of hydrogen generation)

Test case	Aqueous complexation	Minerals	Gas	Cation exchange
TC1	Conservative tracer	-	-	-
TC2	Yes	Fe(s)	$H_2(g)$	-
TC3	Yes	Fe(s), bentonite minerals and corrosion products	$H_2(g)$	-
TC4	Yes	Fe(s), bentonite minerals and corrosion products	$H_2(g)$	Na^+, K^+, Ca^{2+}, Mg^{2+}
TC5	Yes	Fe(s), bentonite minerals and corrosion products	$H_2(g)$	Na^+, K^+, Ca^{2+}, Mg^{2+}

6.3 Conceptual model

6.3.1 Hydrodynamic processes

Although the bentonite blocks are initially unsaturated, the reactive transport model of the HLW disposal cell in granite assumes that the bentonite is initially water-saturated because the bentonite barrier will become fully saturated in less than 50 years (Zheng and Samper, 2008).

The model accounts for molecular diffusion. The hydraulic conductivity of the bentonite is extremely low ($6 \cdot 10^{-14}$ m/s). Therefore, advection is negligible and solute diffusion is the main solute transport mechanism. All the water is assumed to be accessible to solutes.

Solute transport through the granite is simulated with a prescribed water flux parallel to the axis of the gallery at the bentonite/granite interface.

6.3.2 Thermal processes

All the runs in the reactive transport model of the HLW disposal cell in granite are non-isothermal. The selected time evolution of the temperature at the canister-bentonite and the bentonite-granite interfaces in a HLW disposal cell in granite after 100 years of storage was used in the model (*Figure 49*). These data was computed by E. Neeft with the thermal parameters of the Febex bentonite and the Spanish Reference Granite (Neeft, 2020, personal communication).

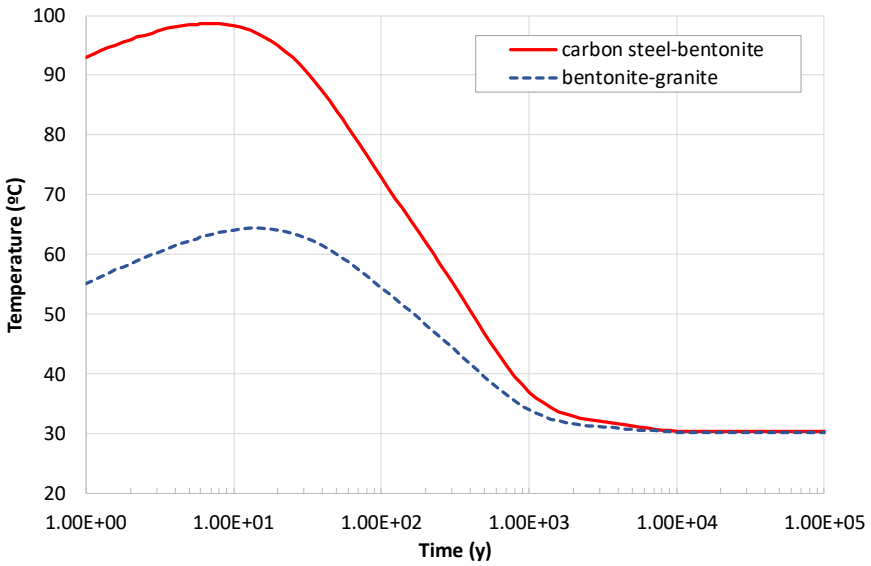

Figure 49.- Time evolution of the temperature in the canister/bentonite and bentonite/granite interfaces used in the model of the HLW disposal cell in granite.

6.3.3 Chemical processes

The conceptual geochemical model of the HLW disposal cell in granite includes the following processes: 1) Carbon-steel canister corrosion, 2) Aqueous complexation; 3) Acid/base; 4) Redox; 5) Mineral dissolution/precipitation; and 6) Cation exchange of Ca^{2+}, Mg^{2+}, Fe^{2+}, Na^{+} and K^{+}.

The geochemical system is defined in terms of 13 primary species (H_2O, H^{+}, $O_2(aq)$, Ca^{2+}, Mg^{2+}, Na^{+}, K^{+}, Fe^{2+}, Al^{3+}, Cl^{-}, SO_4^{2-}, HCO_3^{-}, H_4SiO_4,), 39 secondary aqueous species, 9 minerals and 5 cation exchange species. The secondary aqueous species were identified from speciation runs performed with EQ3/6 (Wolery, 1992). The Gaines-Thomas convention was used for cation exchange reactions (Appelo and Postma, 1993) only in the bentonite. Chemical reactions and the equilibrium constants at 25ºC for aqueous species and mineral dissolution/precipitation used in the model are listed in Table 14.

All the reactions are assumed at chemical equilibrium, except for the dissolution/precipitation of some minerals which are kinetically controlled such as the carbon-steel corrosion. The following kinetic rate law is used:

$$r_m = s_m k_m e^{\frac{-Ea}{RT}} \left(\prod_{i=1}^{N_T} a_i^{p_{mi}} \right) \left| \left(\Omega_m^{\theta} - 1 \right)^{\eta} \right| \quad (63)$$

where r_m is the dissolution/precipitation rate (mol/m²/s), k_m is the kinetic rate constant (mol/m²/s) at 25ºC, E_a is the activation energy, R is the gas constant (J/K·mol), T is the temperature (K), Ω_m is the saturation index which is equal to the ratio of the ion activity product to the equilibrium constant (dimensionless), Θ and η are empirical parameters, $\lfloor \cdot \rfloor$ is the absolute value operator, and $\prod_{i=1}^{N_T} a_i^{p_{mi}}$ is a catalytic term which accounts for the activities a_i of the aqueous species and p_{mi} is the exponent for the i-th aqueous species in the m-th mineral phase dissolution reaction. Variable s_m is taken equal to -1 for precipitation and 1 for dissolution to ensure that the dissolution/precipitation rate is always positive for dissolution and negative for precipitation for any values of the parameters Θ and η.

The dissolution/precipitation rate in mol/m²/s, r_m, is multiplied by the mineral specific surface area, σ, to get the dissolution/precipitation rate in mol/m³/s, R_m. The specific surface area σ is defined as the surface area of the mineral per unit fluid volume. The reactive transport model of the HLW disposal cell in granite assumes that σ is constant in time.

Table 14 - *Chemical reactions and equilibrium constants for aqueous complexes and minerals at 25ºC taken from the thermodynamic database ThermoChimie v11.a (Giffaut et al., 2014).*

Aqueous complexes	**Log K**
$CaCO_3(aq) + H^+ \Leftrightarrow Ca^{2+} + HCO_3^-$	7.1100
$CaHCO_3^+ \Leftrightarrow Ca^{2+} + HCO_3^-$	-1.100
$CaSO_4(aq) \Leftrightarrow Ca^{2+} + SO_4^{2-}$	-2.310
$CaOH^+ + H^+ \Leftrightarrow Ca^{2+} + H_2O$	12.78
$CO_2(aq) + H_2O \Leftrightarrow H^+ + HCO_3^-$	-6.350
$CO_3^{2-} + H^+ \Leftrightarrow HCO_3^-$	10.33
$KOH(aq) + H^+ \Leftrightarrow K^+ + H_2O$	14.460
$KSO_4^- \Leftrightarrow K^+ + SO_4^{2-}$	-0.8796
$MgCO_3(aq) \Leftrightarrow Mg^{2+} + CO_3^{2-}$	-2.980
$MgHCO_3^+ \Leftrightarrow Mg^{2+} + HCO_3^-$	-1.040
$MgSO_4(aq) \Leftrightarrow Mg^{2+} + SO_4^{2-}$	-2.230
$MgOH^+ + H^+ \Leftrightarrow Mg^{2+} + H_2O$	11.680
$NaHCO_3(aq) \Leftrightarrow Na^+ + HCO_3^-$	0.250
$NaSO_4^- \Leftrightarrow Na^+ + SO_4^{2-}$	-0.940
$NaCO_3^- \Leftrightarrow Na^+ + CO_3^{2-}$	-1.270
$NaOH(aq) + H^+ \Leftrightarrow Na^+ + H_2O$	14.750
$OH^- + H^+ \Leftrightarrow H_2O$	14.000
$HSO_4^- \Leftrightarrow H^+ + SO_4^{2-}$	1.9791
$HS^- + 2O_2(aq) \Leftrightarrow H^+ + SO_4^{2-}$	138.27
$Fe^{3+} + 0.5H_2O \Leftrightarrow H^+ + 0.25O_2 + Fe^{2+}$	-8.485
$FeHCO_3^+ \Leftrightarrow Fe^{2+} + HCO_3^-$	-1.440
$FeCO_3(aq) \Leftrightarrow Fe^{2+} + CO_3^{2-}$	4.640
$FeCl^+ \Leftrightarrow Fe^{2+} + Cl^-$	-0.140
$FeCl^{2+} + 0.5H_2O \Leftrightarrow Fe^{2+} + Cl^- + H^+ + 0.25O_2(aq)$	-9.885
$FeOH^+ + H^+ \Leftrightarrow Fe^{2+} + H_2O$	9.500
$FeOH^{2+} \Leftrightarrow Fe^{2+} + 0.5H_2O + 0.25O_2(aq)$	-6.295
$Fe(OH)_2(aq) + 2H^+ \Leftrightarrow Fe^{2+} + 2H_2O$	20.60
$Fe(OH)_3(aq) + 2H^+ \Leftrightarrow Fe^{2+} + 2.5H_2O + 0.25O_2(aq)$	4.075
$Fe(OH)_4^- + 3H^+ \Leftrightarrow Fe^{2+} + 3.5H_2O + 0.25O_2(aq)$	13.115
$Fe(OH)_2^+ + H^+ \Leftrightarrow Fe^{2+} + 1.5H_2O + 0.25O_2(aq)$	-2.815
$Fe(SO_4)_2^- + 0.5H_2O \Leftrightarrow Fe^{2+} + 2SO_4^{2-} + H^+ + 0.25O_2(aq)$	-13.885
$FeSO_4(aq) \Leftrightarrow Fe^{2+} + SO_4^{2-}$	-2.200
$FeHSO_4^{2+} + 0.5H_2O \Leftrightarrow Fe^{2+} + 2H^+ + SO_4^{2-} + 0.25O_2(aq)$	-12.955

$Fe_2(OH)_2^{4+} + 2H^+ \Leftrightarrow 2Fe^{2+} + H_2O + 0.5O_2(aq)$	-14.020
$H_2(aq) + 0.5O_2 \Leftrightarrow H_2O$	46.07
$Al(OH)_2^+ + 2H^+ \Leftrightarrow Al^{3+} + 2H_2O$	10.580
$Al(OH)_3(aq) + 3H^+ \Leftrightarrow Al^{3+} + 3H_2O$	16.420
$Al(OH)_4^- + 4H^+ \Leftrightarrow Al^{3+} + 4H_2O$	22.870
$Al(OH)^{2+} + H^+ \Leftrightarrow Al^{3+} + H_2O$	4.9500
Minerals	**LogK**
$Calcite + H^+ \Leftrightarrow Ca^{2+} + HCO_3^-$	1.850
$Magnetite + 6H^+ \Leftrightarrow 3Fe^{2+} + 0.5O_2(aq) + 3H_2O$	-6.560
$Siderite + H^+ \Leftrightarrow Fe^{2+} + HCO_3^-$	-0.470
$Goethite + 2H^+ \Leftrightarrow Fe^{2+} + 1.5H_2O + 0.25O_2(aq)$	-8.090
$Fe(s) + 2H^+ \Leftrightarrow Fe^{2+} + 2H_2O + 2OH^- + H_2(aq)$	58.85

6.3.3.1 Carbon steel corrosion

The available oxygen in the HLW disposal cell in granite will be consumed soon after its closure, and anaerobic conditions will prevail in the long term. The canister is treated as a porous material made of 100% metallic iron, Fe(s). Under anaerobic conditions, H_2O is the oxidizing agent of Fe(s) (Lu et al., 2011; Mon, 2017; Samper et al., 2016). The anaerobic Fe(s) corrosion reaction is given by:

$$Fe(s) + 2H_2O \rightleftarrows Fe^{2+} + 2OH^- + H_2(g) \quad (64)$$

By rewriting this reaction in terms of the primary species used in the numerical model, one obtains:

$$Fe(s) + 2H^+ + 0.5O_2(aq) \rightleftarrows Fe^{2+} + H_2O \quad (65)$$

The carbon-steel corrosion is kinetically controlled and assumed to corrode at a constant rate of 2 μm/year which amounts to 0.281 mol/m^2/year.

6.4 Numerical model

6.4.1 Grid and simulated time

A 1-D numerical model of the canister and the bentonite was used to simulate the long term interactions of the corrosion products and the bentonite (*Figure 50*). Water flow and solute transport through the granite was simulated with a constant water flux of 4.6 L/y parallel to the axis of the gallery at the bentonite-granite interface. The finite element mesh has 93 nodes and 92 elements. Numerical simulations were performed for a time horizon of 10.000-50.000 years. The spatial mesh discretization is non uniform.

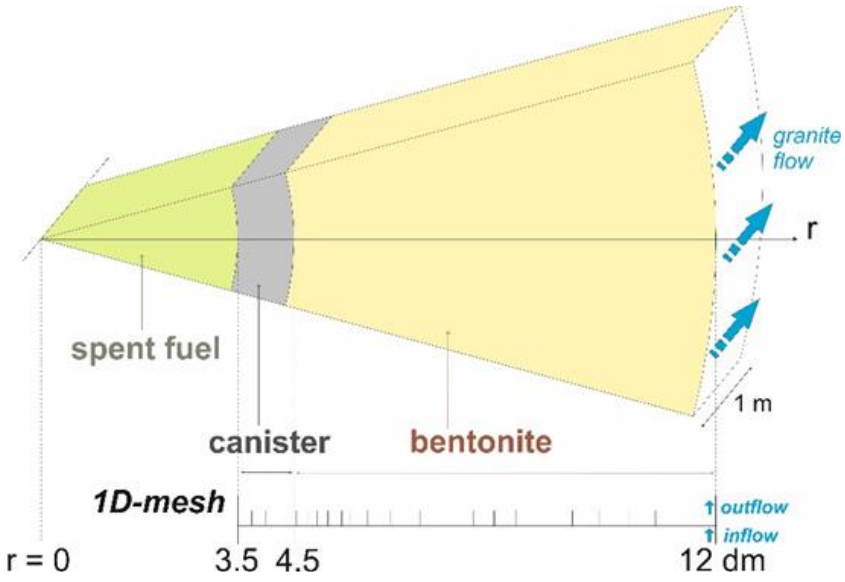

Figure 50.- Sketch of the engineered barrier system and 1D finite element grid of the 1D model.

6.4.2 Flow and transport parameters

The FEBEX bentonite is considered initially saturated with a thickness of 75 cm. The hydraulic conductivity of the bentonite is extremely low, with a value of $6 \cdot 10^{-14}$ m/s (Samper et al., 2016). Therefore, solute advection is negligible and diffusion is the main solute transport mechanism. All the water is assumed to be accessible to solutes.

The bentonite porosity, ϕ, is equal to 0.407. The effective diffusion coefficient, D_e, of the bentonite is equal to $4.07 \cdot 10^{-11}$ m^2/s (Samper et al., 2016). The solid density of the bentonite is 2700 kg/m^3. The specific heat capacity and the saturated thermal conductivity of the bentonite are equal to 846.4 J/kgºC and 1.15 W/mºC, respectively (Samper et al., 2016).

The canister is assumed to have the same transport parameters, De and ϕ, as the bentonite.

The specific heat capacities of the bentonite and the canister are equal to 846 and 480 J/kgºC, respectively. The saturated thermal conductivities of bentonite and steel canister are equal to 1.15, and 50 W/mºC, respectively (ENRESA, 2000).

The thermal and hydrodynamic parameters of the bentonite considered in the reactive transport model of a HLW disposal cell in granite are listed in *Table 15* (Samper et al., 2018; Samper et al., 2016).

Table 15 - Thermal and hydrodynamic parameters of the bentonite (Samper et al., 2018; Samper et al., 2016; Zheng and Samper, 2008; Zheng et al., 2011).

Parameter	*Bentonite*
Hydraulic conductivity (m/s)	$6 \cdot 10^{-14}$
Liquid viscosity (kg/m s)	$7 \cdot 10^{-5}(T-44)^{-1.562}$
Solid density (kg/m3)	*2700*
Specific heat of the solid (J/kg ºC)	*846.4*

Thermal conductivity of the solid (W/m ºC)	*1.23*

6.4.3 Chemical parameters

The chemical composition of the initial bentonite porewater (Samper et al., 2016) is listed in *Table 16*. The initial accessory mineral volume fraction of the calcite considered in the bentonite is 1%. Magnetite, siderite and goethite are not initially present in the system but are allowed to precipitate. The cation exchange capacity (CEC) of the bentonite is 102 meq/100 g (Fernández et al., 2004). Cation selectivity coefficients for exchanged Ca^{2+}, Mg^{2+}, K^{+} and Fe^{+} were derived from Samper et al. (Samper et al., 2008) and Tournassat (2003). *Table 17* shows the selectivity constants for cation exchange reactions in the FEBEX bentonite.

The initial chemical composition of the canister porewater is assumed to be the same as that of the bentonite porewater. The canister is treated as a porous material made of 100% metallic iron, Fe(s). The chemical composition of the granite boundary water (Samper et al., 2016) is listed in *Table 18*.

Table 16 - Chemical composition of the initial FEBEX bentonite porewater (Samper et al., 2016).

Species (mol/L)	**FEBEX bentonite porewater**
pH	6.46
Eh (V)	-0.078
Ca^{2+}	$3.32 \cdot 10^{-2}$
Mg^{2+}	$3.67 \cdot 10^{-2}$
Na^{+}	$1.88 \cdot 10^{-1}$
K^{+}	$1.55 \cdot 10^{-3}$
Fe^{2+}	$1.43 \cdot 10^{-4}$
Al^{3+}	$1.0 \cdot 10^{-8}$
Cl^{-}	$2.75 \cdot 10^{-1}$
HCO_3^{-}	$7.59 \cdot 10^{-3}$
SO_4^{2-}	$2.05 \cdot 10^{-2}$
SiO_2 (aq)	$9.67 \cdot 10^{-5}$

Table 17 - Selectivity constants for cation exchange reactions in the FEBEX bentonite (ENRESA, 2006).

Cation exchange	**$K_{Na\text{-}cation}$**
$Na^{+} + X\text{-}K \Leftrightarrow K^{+} + X\text{-}Na$	0.138
$Na^{+} + 0.5\ X_2\text{-}Ca \Leftrightarrow 0.5\ Ca^{2+} + X\text{-}Na$	0.2924
$Na^{+} + 0.5\ X_2\text{-}Mg \Leftrightarrow 0.5\ Mg^{2+} + X\text{-}Na$	0.2881
$Na^{+} + 0.5\ X_2\text{-}Fe \Leftrightarrow 0.5\ Fe^{2+} + X\text{-}Na$	0.5

Table 18 - Chemical composition of the granite boundary water (Samper et al., 2016).

Species (mol/L)	Granite boundary water
pH	7.825
Eh (V)	-0.188
Ca^{2+}	$1.522 \cdot 10^{-4}$
Mg^{2+}	$1.604 \cdot 10^{-4}$
Na^{+}	$4.350 \cdot 10^{-3}$
K^{+}	$5.371 \cdot 10^{-5}$
Fe^{2+}	$1.791 \cdot 10^{-8}$
Al^{3+}	$1.85 \cdot 10^{-8}$
Cl^{-}	$3.949 \cdot 10^{-4}$
HCO_3^{-}	$5.049 \cdot 10^{-3}$
SO_4^{2-}	$1.561 \cdot 10^{-5}$
SiO_2 (aq)	$3.761 \cdot 10^{-4}$

6.5 Calculated model results

An excel file of each benchmark test case will be distributed to compare the computed results including the time evolution at selected locations and the spatial distribution at selected times of:

- The computed liquid and gas saturation
- The computed total dissolved chemical species concentration and pH
- The computed concentration of precipitated and dissolved minerals
- The computed concentration of exchanged cations
- The computed gases concentration

7. References

Bildstein O., Claret F. and Lagneau V. (2021) Guest editorial to the special issue: subsurface environmental simulation benchmarks. *Computational Geosciences* **25**, 1281-1283.

Birkholzer J. T., Tsang C.-F., Bond A. E., Hudson J. A., Jing L. and Stephansson O. (2019) 25 years of DECOVALEX-Scientific advances and lessons learned from an international research collaboration in coupled subsurface processes. *International Journal of Rock Mechanics and Mining Sciences* **122**, 103995.

Fernández A. (2011) Determination of the Specific Heat Capacity of materials used as confinement barrier at El Cabril. Interim Report CIEMAT/DMA/2G208/3/11.

Fernández A. M., Baeyens B., Bradbury M. and Rivas P. (2004) Analysis of the porewater chemical composition of a Spanish compacted bentonite used in an engineered barrier. *Physics and Chemistry of the Earth, Parts A/B/C* **29**, 105-118.

Garrels R. M. (1965) Solutions, minerals, and equilibrium. *Freeman* **363**.

Giffaut E., Grivé M., Blanc P., Vieillard P., Colàs E., Gailhanou H., Gaboreau S., Marty N., Made B. and Duro L. (2014) Andra thermodynamic database for performance assessment: ThermoChimie. *Applied Geochemistry* **49**, 225-236.

Hausmannová L., Hanusová I. and Dohnálková M. (2018) Summary of the research of Czech bentonites for use in the deep geological repository–up to 2018.

Helgeson H. and Kirkham D. (1974) Theoretical prediction of the thermodynamic behaviour of aqueous temperatures: II. Debye-Húckel parameters for activity coeffcients and relative partial molal properties. *Am. J. Sci* **274**, 1199-1261.

Iglesias R. J. and Gutiérrez-Alvarez C. V., M.V. (2019) Progress report of a THM cell with MX-80 pellets, in: CIEMAT (Ed.), p. 22.

Imbert C. and Villar M. V. (2006) Hydro-mechanical response of a bentonite pellets/powder mixture upon infiltration. *Applied Clay Science* **32**, 197-209.

Kulik D. A., Miron G. D. and Lothenbach B. (2022) A structurally-consistent CASH+ sublattice solid solution model for fully hydrated C-S-H phases: Thermodynamic basis, methods, and Ca-Si-H2O core sub-model. *Cement and Concrete Research* **151**, 106585.

Laloy E. and Jacques D. (2019) Emulation of CPU-demanding reactive transport models: a comparison of Gaussian processes, polynomial chaos expansion, and deep neural networks. *Computational Geosciences* **23**, 1193-1215.

Leal A. M., Kulik D. A. and Saar M. O. (2017) Ultra-fast reactive transport simulations when chemical reactions meet machine learning: chemical equilibrium. *arXiv preprint arXiv:1708.04825*.

Lothenbach B., Kulik D. A., Matschei T., Balonis M., Baquerizo L., Dilnesa B., Miron G. D. and Myers R. J. (2019) Cemdata18: A chemical thermodynamic database for hydrated Portland cements and alkali-activated materials. *Cement and Concrete Research* **115**, 472-506.

Lu C., Samper J., Fritz B., Clement A. and Montenegro L. (2011) Interactions of corrosion products and bentonite: An extended multicomponent reactive transport model. *Physics and Chemistry of the Earth, Parts A/B/C* **36**, 1661-1668.

Marques Fernandes M., Baeyens B., Dähn R., Scheinost A. C. and Bradbury M. H. (2012) U(VI) sorption on montmorillonite in the absence and presence of carbonate: A macroscopic and microscopic study. *Geochimica et Cosmochimica Acta* **93**, 262-277.

Miron G. D., Kulik D. A., Yan Y., Tits J. and Lothenbach B. (2022) Extensions of CASH+ thermodynamic solid solution model for the uptake of alkali metals and alkaline earth metals in C-S-H. *Cement and Concrete Research* **152**, 106667.

Mon A. (2017) Coupled thermo-hydro-chemical-mechanical models for the bentonite barrier in a radioactive waste repository.

Mon A., Samper J., Montenegro L., Naves A. and Fernández J. (2017) Long-term non-isothermal reactive transport model of compacted bentonite, concrete and corrosion products in a HLW repository in clay. *Journal of contaminant hydrology* **197**, 1-16.

Navarro V. and Alonso E. (2000) Modeling swelling soils for disposal barriers. *Computers and Geotechnics* **27**, 19-43.

Pearson F., Tournassat C. and Gaucher E. C. (2011) Biogeochemical processes in a clay formation in situ experiment: Part E–Equilibrium controls on chemistry of pore water from the Opalinus Clay, Mont Terri Underground Research Laboratory, Switzerland. *Applied geochemistry* **26**, 990-1008.

Prasianakis N. I., Haller R., Mahrous M., Poonoosamy J., Pfingsten W. and Churakov S. V. (2020) Neural network based process coupling and parameter upscaling in reactive transport simulations. *Geochimica et Cosmochimica Acta* **291**, 126-143.

Samper J., Lu C. and Montenegro L. (2008) Coupled hydrogeochemical calculations of the interactions of corrosion products and bentonite. *Physics and Chemistry of the Earth* **33**, S306-S316.

Samper J., Xu T. and Yang C. (2009) A sequential partly iterative approach for multicomponent reactive transport with CORE2D. *Computational Geosciences* **13**, 301-316.

Samper J., Mon A. and Montenegro L. (2018) A revisited thermal, hydrodynamic, chemical and mechanical model of compacted bentonite for the entire duration of the FEBEX in situ test. *Applied Clay Science* **160**, 58-70.

Samper J., Naves A., Montenegro L. and Mon A. (2016) Reactive transport modelling of the long-term interactions of corrosion products and compacted bentonite in a HLW repository in granite: Uncertainties and relevance for performance assessment. *Applied Geochemistry* **67**, 42-51.

Soler J. M. (2001) The effect of coupled transport phenomena in the Opalinus Clay and implications for radionuclide transport. *Journal of Contaminant Hydrology* **53**, 63-84.

Steefel C. I., Yabusaki S. B. and Mayer K. U. (2015) Reactive transport benchmarks for subsurface environmental simulation. *Computational Geosciences* **19**, 439.

Tang A.-M., Cui Y.-J. and Le T.-T. (2008) A study on the thermal conductivity of compacted bentonites. *Applied Clay Science* **41**, 181-189.

Tournassat C. (2003) Interactions cations-argiles: le cas du Fe (II). Application au contexte de stockage profond des déchets radioactifs. Université Joseph-Fourier-Grenoble I.

Van Wijk W. and De Vries D. (1963) Thermal properties of soils. North Holland Publishing, Amsterdam, pp. 210-235.

Villar M. (2013) Long-term THM tests reports: Isothermal infiltration tests with materials from the HE-E. PEBS Deliverable 2.2-7.2. CIEMAT Technical Report CIEMAT/DMA/2G210/07/2013. Madrid.

Villar M., Martín P., Gómez-Espina R., Romero F. and Barcala J. (2012) THM cells for the HE-E test: setup and first results. *PEBS Report D* **2**.

Villar M. V. (2020) MX-80 Bentonite. Thermo-Hydro-Mechanical Characterisation Performed ad CIEMAT in the Context of the Prototype Project.

Zheng L. and Samper J. (2008) A coupled THMC model of FEBEX mock-up test. *Physics and Chemistry of the Earth, Parts A/B/C* **33**, S486-S498.

Zheng L., Samper J. and Montenegro L. (2011) A coupled THC model of the FEBEX in situ test with bentonite swelling and chemical and thermal osmosis. *Journal of contaminant hydrology* **126**, 45-60.